NASA/TM–2000–209894

A Comprehensive Model of the Near-Earth Magnetic Field: Phase 3

Terence J. Sabaka, Nils Olsen, and Robert A. Langel

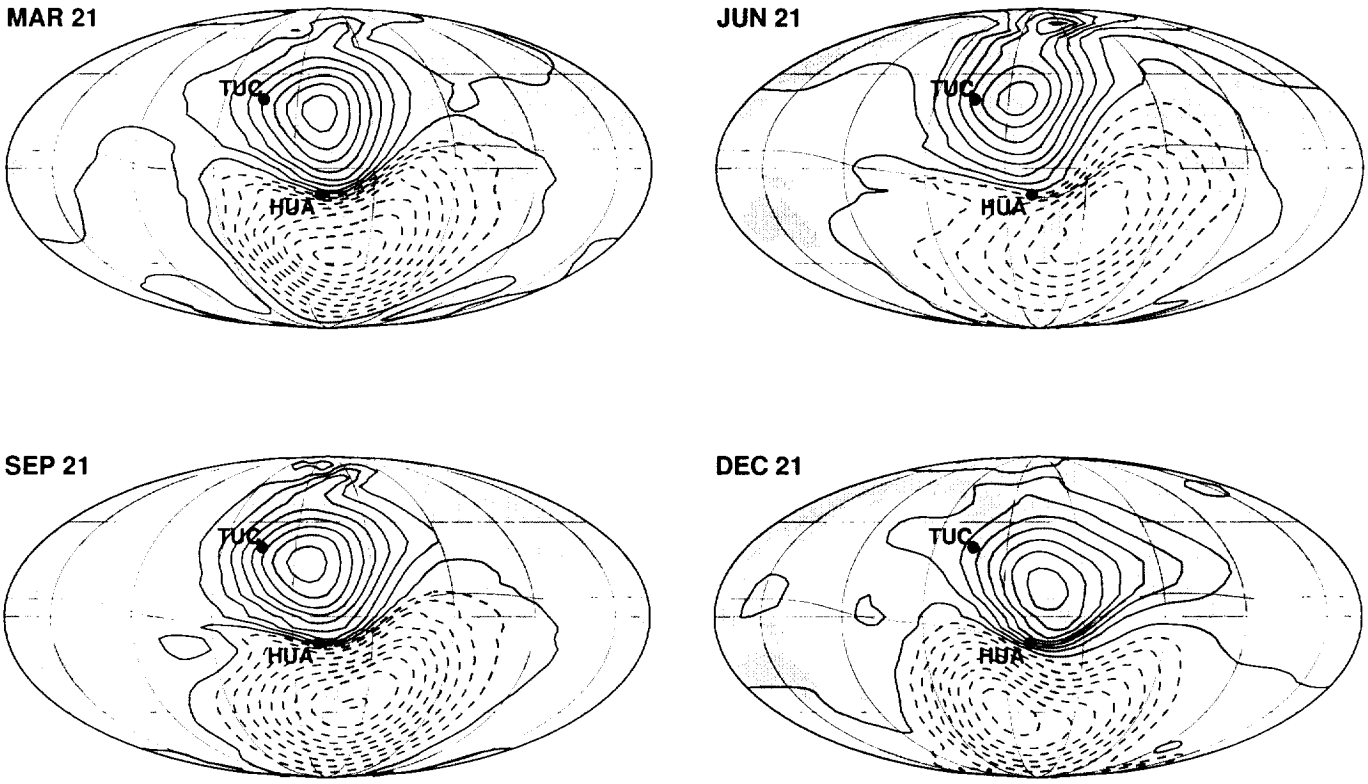

April 2000

The NASA STI Program Office ... in Profile

Since its founding, NASA has been dedicated to the advancement of aeronautics and space science. The NASA Scientific and Technical Information (STI) Program Office plays a key part in helping NASA maintain this important role.

The NASA STI Program Office is operated by Langley Research Center, the lead center for NASA's scientific and technical information. The NASA STI Program Office provides access to the NASA STI Database, the largest collection of aeronautical and space science STI in the world. The Program Office is also NASA's institutional mechanism for disseminating the results of its research and development activities. These results are published by NASA in the NASA STI Report Series, which includes the following report types:

- TECHNICAL PUBLICATION. Reports of completed research or a major significant phase of research that present the results of NASA programs and include extensive data or theoretical analysis. Includes compilations of significant scientific and technical data and information deemed to be of continuing reference value. NASA's counterpart of peer-reviewed formal professional papers but has less stringent limitations on manuscript length and extent of graphic presentations.
- TECHNICAL MEMORANDUM. Scientific and technical findings that are preliminary or of specialized interest, e.g., quick release reports, working papers, and bibliographies that contain minimal annotation. Does not contain extensive analysis.
- CONTRACTOR REPORT. Scientific and technical findings by NASA-sponsored contractors and grantees.
- CONFERENCE PUBLICATION. Collected papers from scientific and technical conferences, symposia, seminars, or other meetings sponsored or cosponsored by NASA.
- SPECIAL PUBLICATION. Scientific, technical, or historical information from NASA programs, projects, and mission, often concerned with subjects having substantial public interest.
- TECHNICAL TRANSLATION. English-language translations of foreign scientific and technical material pertinent to NASA's mission.

Specialized services that complement the STI Program Office's diverse offerings include creating custom thesauri, building customized databases, organizing and publishing research results . . . even providing videos.

For more information about the NASA STI Program Office, see the following:

- Access the NASA STI Program Home Page at http://www.sti.nasa.gov/STI-homepage.html
- E-mail your question via the Internet to help@sti.nasa.gov
- Fax your question to the NASA Access Help Desk at (301) 621-0134
- Telephone the NASA Access Help Desk at (301) 621-0390
- Write to:
  NASA Access Help Desk
  NASA Center for AeroSpace Information
  7121 Standard Drive
  Hanover, MD 21076–1320

NASA/TM–2000–209894

A Comprehensive Model of the Near-Earth Magnetic Field: Phase 3

Terence J. Sabaka
Raytheon ITSS, Lanham, Maryland

Nils Olsen
Danish Space Research Institute, Juliane Maries Vej 30, DK-2100 Copenhagen Ø, Denmark

Robert A. Langel
Formerly, NASA-GSFC, Geodynamics Branch, Greenbelt, Maryland

National Aeronautics and
Space Administration

Goddard Space Flight Center
Greenbelt, Maryland 20771

April 2000

Available from:

NASA Center for AeroSpace Information
7121 Standard Drive
Hanover, MD 21076–1320
Price Code: A17

National Technical Information Service
5285 Port Royal Road
Springfield, VA 22161
Price Code: A10

Abstract

The near-Earth magnetic field is due to sources in Earth's core, ionosphere, magnetosphere, lithosphere, and from coupling currents bewteen ionosphere and magnetosphere and between hemispheres. Traditionally, the main field (low degree internal field) and magnetospheric field have been modeled simultaneously, and fields from other sources modeled separately. Modelling separately can introduce spurious features. A new model, designated CMP3 (Comprehensive Model: Phase 3), has been derived from quiet-time Magsat and POGO satellite measurements and observatory hourly and annual means measurements as part of an effort to coestimate fields from all of these sources. The initial phase of this work was reported in *Sabaka and Baldwin* [1993], and the second phase in *Langel et al.* [1996]. In this third phase the model of the dominant sun-synchronus, local time morphology of the ionospheric field is now supplemented with non-local time modes. Since many ionospheric features follow lines of dip latitude in equatorial regions and of the auroral oval in polar latitudes, special quasi-dipole (QD) conforming harmonic functions have been introduced, including terms accounting for seasonal variation and variation with solar activity. The new model also accounts for low conductivity levels in the low and mid-latitude regions of the nightside ionosphere via special constraints on the QD functions. Both local and non-local time terms, with seasonal modulations, are included in a spherical harmonic representation of the field of magnetospheric origin. The dipole terms in this external field expansion include variation with respect to the D_{st} index in order to account for variations in the intensity of the ring-current. Because the time varying ionospheric and magnetospheric fields induce currents in the Earth, a transfer function between the primary and induced fields is introduced under the simplifying assumption of an *a priori* radially varying conductivity model. The fields produced by coupling currents (both field-aligned and meridional) flowing in the satellite sampling region have been explicitly modeled under the assumption that they are primarily radial in direction in the sampling region. This radial current density model, including seasonal variation, is accomplished via separate toroidal stream function representations of the associated fields at dawn and dusk for Magsat data. Finally, the internal spherical harmonic expansion is extended to degree 65 in order to account for fields from the Earth's lithosphere as measured at satellite altitude. The result of this effort is a model whose fits to the data are generally superior to previous models and whose parameter states for the various constituent sources are very reasonable.

Contents

List of Figures

List of Tables

List of Frequently used Symbols

$a = 6371.2$ km	Mean radius of Earth
$\underline{a}(\underline{x})$	Non-linear, continuously differentiable vector function of $\underline{x}$
A_n	Jacobian of $\underline{a}(\underline{x})$ evaluated at n-th iterate $\underline{x}_n$
A_{n_i}	Portion of A_n corresponding to i-th data group
b_j^k	B-spline of order k which is non-zero over knot interval $\tau_q < t \leq \tau_{q+k}$
$\underline{B} = (X, Y, Z)^T$	Magnetic field vector in local north (X), east (Y), down (Z) directions either on sphere or ellipsoid
$\underline{B} = (B_r, B_\theta, B_\phi)^T$	Magnetic field vector in local r, θ, ϕ directions
$\underline{B}_{bias,OAM}$	Static vector bias solution at a given observatory annual means station
$\underline{B}_{bias,OHM}$	Static vector bias solution at a given observatory hourly means station
$\Delta\underline{B}_{ltd}$	Deviation of external magnetic field vector from that of an external tilted dipole in magnetic local time
$\delta\underline{B} = \delta\underline{B}_t + \delta\underline{B}_p$	Toroidal ($\delta\underline{B}_t$) and poloidal ($\delta\underline{B}_p$) decomposition of magnetic field vector from ionospheric coupling currents
C	Linear transformation from $\underline{\epsilon}$ to $\underline{\epsilon}'$, i.e. applies conditions for continuity of radial magnetic field across ionospheric equivalent sheet current
$C_\nu, \tilde{C}_\nu$	Covariance matrix of data noise vector $\underline{\nu}$, its *a posteriori* unbiased estimate
$C_{\xi_i}, \tilde{C}_{\xi_i}$	Covariance matrix of error in i-th model constraint state $\underline{\xi}_i$, its *a posteriori* unbiased estimate
$C_x, \tilde{C}_x$	Covariance matrix of error in estimated model state $\underline{\tilde{x}}$, its unbiased estimate
$\delta = 1000$ km	Penetration depth of "very long-period" inducing fields, i.e. longer than one week or so
$\underline{d}$	Data vector, i.e. vector of measurements
D_{st}	Disturbance storm-time index in units of nT
D, d_{kn}^{lm}	Linear transformation from generic QD to generic SH expansion coefficients on a given shell, maps coefficient of QD degree k and order l to coefficient of SH degree n and order m, i.e. applies QD constraints on a given sphere
$D_e, d_{kn,e}^{lm}$	Linear transformation from $\underline{\tilde{\epsilon}}$ to $\underline{\epsilon}$, maps $\tilde{\epsilon}_{ksp}^{l}$ to ϵ_{nsp}^{m}, i.e. applies QD constraints to SH's in external ionospheric potential
$D_i, d_{kn,i}^{lm}$	Linear transformation from $\underline{\tilde{\epsilon}}'$ to $\underline{\epsilon}'$ and from $\underline{\tilde{\iota}}$ to $\underline{\iota}$, maps $\tilde{\epsilon}_{ksp}^{l\prime}$ to $\epsilon_{nsp}^{m\prime}$ and $\tilde{\iota}_{ksp}^{l}$ to ι_{nsp}^{m}, i.e. applies QD constraints to SH's in internal ionospheric potential
$D_j, d_{kn,j}^{lm}$	Linear transformation from $\underline{\tilde{\phi}}$ to $\underline{\phi}$, maps $\tilde{\phi}_{ks}^{l}$ to ϕ_{ns}^{m}, i.e. applies QD constraints to surface SH's in toroidal magnetic field stream function from coupling currents
η	Spherical colatitude minus geodetic colatitude

$\underline{\epsilon}$, ϵ_{nsp}^{m} Vector of complex, periodic SH expansion coefficients for external ionospheric and magnetospheric potentials, coefficient of periodic SH of degree n and order m with seasonal and diurnal wavenumbers s and p, except for $n = 1$ magnetospheric coefficients which have linear D_{st} dependence also

$\underline{\epsilon}'$, $\epsilon_{nsp}^{m\prime}$ Vector of complex, periodic SH expansion coefficients for internal ionospheric potential, coefficient of periodic SH of degree n and order m with seasonal and diurnal wavenumbers s and p

$\underline{\tilde{\epsilon}}$, $\tilde{\epsilon}_{ksp}^{l}$ Vector of complex, periodic QD expansion coefficients for external ionospheric potential, coefficient of periodic QD function of degree k and order l with seasonal and diurnal wavenumbers s and p

$\underline{\tilde{\epsilon}}'$, $\tilde{\epsilon}_{ksp}^{l\prime}$ Vector of complex, periodic QD expansion coefficients for internal ionospheric potential, coefficient of periodic QD function of degree k and order l with seasonal and diurnal wavenumbers s and p

$\underline{\tilde{\varepsilon}}$, $\tilde{\varepsilon}_{ksp}^{l}$ Vector of complex, time-varying QD expansion coefficients for external ionospheric potential as a function of solar radiation flux, coefficient of time-varying QD function of degree k and order l with seasonal and diurnal wavenumbers s and p

$e = 1980$ Epoch of temporal expansion of $\gamma_n^m(t)$

$\underline{\tilde{e}}$ Real vector composed of real and imaginary parts of $\underline{\tilde{\varepsilon}}$

$E[\cdot]$ Statistical expectation operator

$\underline{\phi}$, ϕ_{ns}^{m} Vector of complex, periodic surface SH expansion coefficients for toroidal magnetic field stream function from coupling currents, coefficient of periodic SH of degree n and order m with seasonal wavenumber s

$\underline{\tilde{\phi}}$, $\tilde{\phi}_{ks}^{l}$ Vector of complex, periodic surface QD expansion coefficients for toroidal magnetic field stream function from coupling currents, coefficient of periodic QD function of degree k and order l with seasonal wavenumber s

Φ Stream function of toroidal magnetic field from coupling currents

$\underline{f}_z$ Real linear functional or form which maps estimated model state $\underline{\tilde{x}}$ into some real scalar function $\tilde{z}$

$F_{10.7}$ Solar radiation flux at 10.7 cm wavelength in units of $10^{-22}\mathrm{W/m^2/Hz}$

F, f_{knsp}^{lm} Linear transformation from $\underline{\tilde{\epsilon}}$ to $\underline{\iota}$, maps $\tilde{\epsilon}_{ksp}^{l}$ to ι_{nsp}^{m}, i.e. applies QD constraints and induction transfer function (dependent upon s and p) to SH's in internal potential induced by ionosphere

$\underline{\gamma}$, γ_{nq}^{m} Vector of complex, time-varying SH expansion coefficients for internal potential from core and lithospheric sources, coefficient of SH degree n and order m corresponding to q-th B-spline in $\dot{\gamma}_n^m(t)$ temporal expansion

g_n^m Real part of γ_n^m

G, g_{kn}^{lm}	Linear transformation from $\underline{\tilde{\epsilon}}$ to $\underline{\epsilon}'$, maps $\tilde{\epsilon}_{ksp}^{l}$ to $\epsilon_{nsp}^{m\prime}$, i.e. applies QD constraints and radial field continuity conditions to SH's in internal ionospheric potential
h	Generic height or altitude in units of km (also, number of interior knots in B-spline domain of temporal expansion of $\dot{\gamma}_n^m(t)$)
$h_m = 450$ km	Mean Magsat altitude
h_n^m	Negative imaginary part of γ_n^m
$\underline{\iota}$, ι_{nsp}^m	Vector of complex, periodic SH expansion coefficients for internal potential induced by ionosphere, coefficient of periodic SH of degree n and order m with seasonal and diurnal wavenumbers s and p
$\underline{\tilde{\iota}}$, $\tilde{\iota}_{ksp}^{l}$	Vector of complex, periodic QD expansion coefficients for internal potential induced by ionosphere, coefficient of periodic QD function of degree k and order l with seasonal and diurnal wavenumbers s and p
$\underline{J} = \underline{J}_t + \underline{J}_p$	Toroidal ($\underline{J}_t$) and poloidal ($\underline{J}_p$) decomposition of current density, particularly the ionospheric coupling current density
J_r	Radial component of $\underline{J}_p$, the poloidal portion of the ionospheric coupling current density
$\underline{J}_{eq}$	Ionospheric E-region equivalent sheet current density
k	QD degree (also, order of B-spline)
$K(p-l)$	Determines latitudinal resolution of ionospheric and magnetospheric portions of model as a function of local versus non-local time, i.e. for given l and p, $k_{max} = \|l\| + K(p-l)$, where $K(0)$ refers to local time and $K(\neq 0)$ refers to non-local time (see k, l, and p)
K_p	Planetary index of geomagnetic activity
λ_i	Lagrange multiplier or damping parameter corresponding to, and having reciprocal units of, i-th constraint norm, $\mathcal{Q}_i(\underline{x})$
Λ_i	Real, positive-definite norm matrix corresponding to i-th constraint norm, $\mathcal{Q}_i(\underline{x})$, whose inverse is equivalent to C_{ξ_i}, to within an unknown scale factor
l	QD order
$\mathcal{L}(\underline{x})$	Least-squares cost or objective function to be minimized with respect to $\underline{x}$
$\mathcal{L}_{e_i}(\underline{x})$	Term in $\mathcal{L}(\underline{x})$ corresponding to weighted error variance with respect to i-th preferred model state, $\underline{x}_{a_i}$, i.e. penalizes deviations from $\underline{x}_{a_i}$
$\mathcal{L}_r(\underline{x})$	Term in $\mathcal{L}(\underline{x})$ corresponding to weighted residual variance, i.e. penalizes data misfit
$\mu_0 = 4\pi \times 10^{-7}$ H/m	Permeability of free space
μ_r	Mean of particular residual component
$\underline{\mu}$, μ_{ksp}^{l}	Vector of complex, periodic SH expansion coefficients for external magnetospheric potential with no D_{st} dependence, coefficient of periodic SH of degree k and order l with seasonal and diurnal wavenumbers s and p

$\underline{\mu}_{D_{st}}$, $\mu^l_{ksp,D_{st}}$	Vector of complex, time-varying SH expansion coefficients for external magnetospheric potential with linear D_{st} dependence, coefficient of time-varying SH of degree k and order l with seasonal and diurnal wavenumbers s and p (only $k = 1$ is used in this study)
m	SH order (also, number of knots defining generic spline domain)
M_i	Length of $\underline{x}_{a_i}$ or rank of Λ_i, i.e. number of conditions imposed upon model parameter space by i-th constraint norm, $\mathcal{Q}_i(\underline{x})$
∇_g, ∇_d	Gradient operator in geographic spherical polar coordinates, gradient operator in dipole spherical polar coordinates
$\underline{\nu}$	Data noise vector
n	SH degree (also, iteration number of GLSE)
N	Length of $\underline{d}$, i.e. number of measurements fit by model
N_i	Number of measurements in i-th data subset
N_{max}	Maximum SH degree of internal potential expansion from core and lithospheric sources
$\omega_s = 2\pi$ rads/yr	Fundamental seasonal angular frequency
$\omega_p = 2\pi/24$ rads/hr	Fundamental diurnal angular frequency
Ω_s	Spherical sector
Ψ	Scalar function of poloidal magnetic field from coupling currents, and stream function of ionospheric E-region equivalent sheet current density, $\underline{J}_{eq}$
p	Wavenumber of diurnal periodicity
$P_n^m(\theta)$	Schmidt normalized associated Legendre function of degree n and order m
q	Knot number such that $b_q^k(t)$ is non-zero over $\tau_q < t \leq \tau_{q+k}$
Q, q^{lm}_{knsp}, $q^{mm}_{nn}(f)$	Linear transformation from $\underline{\epsilon}$ to $\underline{\iota}$, maps ϵ^m_{nsp} to ι^l_{ksp}, i.e. applies induction transfer function (dependent upon s and p) to SH's in internal potential induced by ionosphere and magnetosphere (in this study a radially varying conductivity profile is used such that a diagonal matrix results, mapping ϵ^m_{nsp} to ι^m_{nsp})
$\mathcal{Q}_i(\underline{x})$	Quadratic norm corresponding to i-th constraint on $\underline{x}$
$\mathcal{Q}_{\lvert\underline{J}_{eq}\rvert}$	Quadratic norm which measures mean-square magnitude of $\underline{J}_{eq}$ over a spherical sector of 8 hr width, centered on 1:00 am dipole magnetic local time, and over time
$\mathcal{Q}_{\lvert\nabla^2_s \underline{J}_{eq,p>0}\rvert}$	Quadratic norm which measures weighted mean-square magnitude of surface Laplacian of $\underline{J}_{eq}$ for $p > 0$ over sphere and over time
$\mathcal{Q}_{\lvert\Delta\underline{B}_{ltd}\rvert}$	Quadratic norm which measures mean-square magnitude of deviations of external field from that of an external tilted dipole in magnetic local time over sphere at mean Magsat altitude and over time
$\mathcal{Q}_{\lvert J_r\rvert}$	Quadratic norm which measures mean-square magnitude of J_r, radial component of ionospheric coupling currents in Magsat sampling shell, over sphere at mean Magsat altitude and over time (applied separately at dawn and dusk)

$\rho_{z,j}$	Norm of real $\underline{r}_{z,j}$
$\rho_{\|z\|}$	Norm of complex $\underline{r}_{z,j}$ associated with complex $\tilde{z}_j$, i.e. generalization of $\rho_{z,j}$
$\underline{r} = (r, \theta, \phi)^T$	Position vector in spherical coordinates with respect to Earth's geographic axis
$\underline{r} = (r, \theta_d, \phi_d)^T$	Position vector in spherical coordinates with respect to dipole moment of GSFC(12/83) main field model [*Langel and Estes*, 1985b]
$\underline{r} = (r, \theta_q, \phi_q)^T$	Position vector in QD coordinates defined by IGRF 1980 model [*IAGA Division I Working Group 1*, 1981]
$\underline{r}_{z,j}$	Real linear functional or form which maps true model state $\underline{x}$ into expected value of contribution of j-th data subset to some real scalar function $\tilde{z}$
R	Resolution matrix of estimated model state $\underline{\tilde{x}}$ due to data (also, annual sunspot number)
R_{d_i}	Resolution matrix of estimated model state $\underline{\tilde{x}}$ due to i-th data subset
R_{a_i}	Resolution matrix of estimated model state $\underline{\tilde{x}}$ due to i-th constraint
R_n	Mean-squared internal field magnitude per SH degree n over a sphere
R_x	Correlation matrix of estimated model state $\underline{\tilde{x}}$
R_{es}	Rotation matrix from local geographic spherical to local geographic ellipsoidal basis
R_{gd}	Rotation matrix from local dipole spherical to local geographic spherical basis
σ_r	Standard deviation about mean of particular residual component
σ_ν	Assigned *a priori* standard deviation of particular data noise component
$\hat{\sigma}^2$	Unknown data misfit, i.e. unknown scale factor of C_ν
s	Wavenumber of seasonal periodicity
s^2	Unbiased estimate of $\hat{\sigma}^2$, i.e. scale factor of $\tilde{C}_\nu$
$s(t)$	Generic spline function of t
$s^2_{d_i}$	Unbiased estimate of $\hat{\sigma}^2_{d_i}$, unknown scale factor of diagonal block of C_ν associated with i-th data subset, i.e. scale factor of diagonal block of $\tilde{C}_\nu$ associated with i-th data subset
$s^2_{a_i}$	Unbiased estimate of $\hat{\sigma}^2_{a_i}$, unknown scale factor of C_{ξ_i}, i.e. scale factor of $\tilde{C}_{\xi_i}$
$\underline{S}_e$, $S^m_{nsp,e}$	Vector of complex, periodic SH functions for external ionospheric and magnetospheric potentials, periodic SH function of degree n and order m with seasonal and diurnal wavenumbers s and p
$\underline{S}_i$, $S^m_{nsp,i}$	Vector of complex, periodic SH functions for internal ionospheric potential and internal potentials induced by ionosphere and magnetosphere, periodic SH function of degree n and order m with seasonal and diurnal wavenumbers s and p
$\underline{S}_j$, $S^m_{ns,j}$	Vector of complex, periodic surface SH functions for stream function of toroidal magnetic field from ionospheric coupling currents, periodic surface SH function of degree n and order m with seasonal wavenumber s
θ_g	Geodetic colatitude
τ_q	The q-th member of ordered knot set defining B-spline domain used in $\dot{\gamma}^m_n(t)$ temporal expansion

t	Time of year counted from January 1, 00 Universal Time (UT) in units of yr
t_m	Magnetic time of day at dipole prime meridian in units of hr, i.e. magnetic UT (MUT)
t_{mlt}	Magnetic time of day at observer in units of hr, i.e. magnetic local time (MLT)
t_{qlt}	QD magnetic time of day at observer in units of rads, i.e. QD magnetic local time (QLT)
$tr[\cdot]$	Matrix trace operator
$T = 1$ yr	Averaging time for various $\mathcal{Q}_i(\underline{x})$ norms
$\underline{T}_e$, $T^l_{ksp,e}$	Vector of complex, periodic QD functions for external ionospheric and magnetospheric potentials, periodic QD function of degree k and order l with seasonal and diurnal wavenumbers s and p
$\underline{T}_i$, $T^l_{ksp,i}$	Vector of complex, periodic QD functions for internal ionospheric potential and internal potentials induced by ionosphere and magnetosphere, periodic QD function of degree k and order l with seasonal and diurnal wavenumbers s and p
$\underline{T}_j$, $T^l_{ks,j}$	Vector of complex, periodic surface QD functions for stream function of toroidal magnetic field from ionospheric coupling currents, periodic surface QD function of degree k and order l with seasonal wavenumber s
$\underline{u}$	Real vector composed of real and imaginary parts of $\underline{\mu}$
$V = V_{cl}$, V^m_n	Internal scalar potential function from core and lithospheric sources, potential term corresponding to SH degree n and order m
$V = V_{ion}$, V^m_{nsp}	External scalar potential function from ionospheric sources, potential term corresponding to SH degree n and order m with seasonal and diurnal wavenumbers s and p
$V = V_{mag}$, V^m_{nsp}	External scalar potential function from magnetospheric sources, potential term corresponding to SH degree n and order m with seasonal and diurnal wavenumbers s and p
$V' = V'_{ion}$, V'^m_{nsp}	Internal scalar potential function from ionospheric sources, potential term corresponding to SH degree n and order m with seasonal and diurnal wavenumbers s and p
$\underline{\tilde{w}}$	Real vector composed of real and imaginary parts of $\underline{\tilde{\phi}}$
W	Real, positive-definite data weight matrix whose inverse is equivalent to C_ν, to within an unknown scale factor
$\underline{x}_{a_i}$	Preferred *a priori* model state vector from i-th constraint
$\underline{x}_n$	Model state estimate after n iterations of GLSE
$\underline{\tilde{x}}$	Final estimate of true model state from GLSE
$\delta\underline{x}_n$	Correction of model state estimate at n-th iteration of GLSE
$Y^m_n(\theta, \phi)$	Schmidt normalized surface SH of degree n and order m
$\underline{\xi}_i$	Error in i-th model constraint state, $\underline{x}_{a_i}$
$\tilde{z}$	Real scalar function of $\underline{\tilde{x}}$
$E[\tilde{z}_j]$	Expected value of contribution of j-th data subset to $\tilde{z}$

List of Frequently used Acronyms

AEJ	Auroral electrojet
BFLPR	Best fit linear piecewise regression
CMP3	Comprehensive Model: Phase 3
CNXS	Version of CMP3 with no $\mathcal{Q}_{\lvert\Delta \underline{B}_{ltd}\rvert}$ smoothing
EEJ	Equatorial electrojet
FAC	Field aligned current
GLSE	Gauss least-squares estimator
GSFC	Goddard Space Flight Center
GSFC(12/93)	Comprehensive model from first phase study [*Sabaka and Baldwin*, 1993]
GSFC(8/95-SqM)	Comprehensive model from second phase study [*Langel et al.*, 1996]
GSFC/CU(12/96)	Unpublished predecessor to CMP3, developed jointly with University of Copenhagen
LS	Least-squares
MLT	Magnetic local time (see t_{mlt})
MUT	Magnetic universal time (see t_m)
OAM	Observatory annual mean
OHM	Observatory hourly mean
POGO	Polar Orbiting Geophysical Observatories
QD	Quasi-dipole
QLT	Quasi-dipole magnetic local time (see t_{qlt})
RLPAA	Designation given in this paper to the lithospheric ΔZ map of *Ravat et al.* [1995]
SH	Spherical harmonic
Sq	Solar-quiet
UT	Universal time (see t)

1 Introduction

The terrestrial magnetic field is comprised of contributions from many sources. Resolution of these constituent fields is of primary importance in understanding the physical processes responsible for their existence. This paper is concerned with the modeling of the field from measurements at Earth's surface and extending to about 2000 km in altitude above that surface, a region that will be referred to as "near-Earth". Before embarking on this inverse problem, however, a brief background into the nature of these source phenomena is in order.

1.1 Near-Earth magnetic field contributions

By far the most dominant of near-Earth fields is of core origin, accounting for over 97% of the field observed at Earth's surface [*Langel and Hinze*, 1998] and ranging in intensity from about 30,000 nT at the equator to about 50,000 nT at the poles. According to geodynamo theory, inductive interactions between the fluid motion of the liquid outer core and the geomagnetic field not only modify the source current so as to induce secular variation of the field, but sustain it against long-term decay caused by magnetic diffusion and Ohmic dissipation of the source current [*Voorhies*, 1995].

The solar quiet (Sq) magnetic field variation is a manifestation of an ionospheric current system. Heating at the dayside and cooling at the nightside of the atmosphere generates tidal winds which drive ionospheric plasma against the geomagnetic field inducing electric fields and currents in the dynamo region between 80-200 km in height. The current system remains relatively fixed to the Earth-sun line and produces regular daily variations which are directly seen in the magnetograms of geomagnetic "quiet" days, therefore the name Sq. On "disturbed" days there is an additional variation which includes superimposed magnetic storm signatures. Because the geomagnetic field is strictly horizontal at the dip equator, there is an enhancement of the effective Hall conductivity, called the Cowling conductivity, which results in an enhanced eastward current, called the equatorial electrojet (EEJ), flowing along the dayside dip equator. In addition, auroral electrojets (AEJ) flow in the auroral belt and vary in amplitude with different levels of magnetic activity. The Sq fields are on the order of 10-50 nT, depending upon component, latitude, season, solar activity, and time of day; the magnetic signature of the EEJ can be about 5-10 times that of Sq; and that of the AEJ can vary widely from a few 10's nT during quiet periods to several thousand nT during major magnetic storms.

The field originating in Earth's magnetosphere is due primarily to the ring-current and to currents on the magnetopause and in the magnetotail. Currents flowing on the outer boundary of the magnetospheric cavity, known as the magnetopause, cancel the Earth's field outside and distend the field within the cavity. This produces an elongate tail in the anti-solar direction within which sheet currents are established in the equatorial plane. Interaction of these currents with the radiation belts near the Earth produces a ring-current in the dipole equatorial plane which partially encircles the Earth, but achieves closure via field-aligned currents into and out of the ionosphere. These resulting fields have magnitudes on the order of 20-30 nT near the Earth during magnetically quiet periods, but can increase to several hundreds of nT during disturbed times.

If displacement currents are neglected, then the current densities associated with these external fields are solenoidal and therefore must flow along closed circuits. Given the complex nature of the conductivity structure in the near-Earth region, circuit closure is sometimes achieved through currents which couple the various source regions. At high latitudes, the auroral ionosphere and magnetosphere are coupled by currents which flow along Earth's magnetic field lines (see *Potemra* [1982]). The fields from these field-aligned currents (FAC) have magnitudes that vary with the magnetic distrubance level. However, they are always present, on the order of 30-100 nT during quiet periods and up to several thousand nT during substorms. Fields from these currents have been detected in surface data in the Y (east) component of the magnetic field at low latitudes, with difficulty, but are mostly mapped using magnetometers aboard near-Earth orbiting satellites. There are also currents which couple the Sq currents systems in the two hemispheres that flow, at least in part, along magnetic field lines. Detection of these has been reported by *Olsen* [1997a] using data from the Magsat satellite. The associated magnetic fields are generally 10 nT or less. Finally, there exists a meridional current system which is connected to the EEJ with upward directed currents at the dip equator and field-aligned downward directed currents at low latitudes. Fields from this current system have been detected by magnetic

measurements taken on a rocket [*Musmann and Seiler*, 1978] and from those taken by Magsat [*Maeda et al.*, 1982]. In the latter case, the EEJ coupling currents resulted in fields of about 15-40 nT in the Magsat data at dusk local time.

The lithosphere is a rheological classification for that outer layer of the Earth which is rigid. It contains regions whose temperature is below the Curie point of magnetite and other magnetic minerals. As a result, it can have magnetization that is either induced by the present day ambient field or frozen into the rocks at their last time of cooling below the Curie temperature, i.e. remanent magnetization. Fields from the lithosphere are of amplitude up to several thousand nT at the surface and at aircraft altitude and up to about 30 nT at the satellite altitudes considered in this paper.

1.2 Earlier modeling efforts

Historically, fields from the various sources have been modeled separately, or at least not all together. Under the assumption that measurements are aquired in current-free regions, models of the core, magnetospheric, ionospheric, and lithospheric fields have taken the form of gradients of potential functions, usually in spherical coordinates. The main field (the "low" degree spherical harmonic contributions from the core and lithosphere) and magnetospheric field have typically been modeled together as internal and external potentials, respectively. This approach has been used by *Langel and Estes* [1985a, 1985b] to analyze the Magsat satellite data. They include an external field with associated induced contribution of spherical harmonic Y_1^0 whose time variations are proportional to the D_{st} index. *Sabaka et al.* [1997] followed a similar method in modeling secular variation of the long-term magnetospheric field using measurements from satellites, observatory annual-means, repeat stations, and surveys from land, sea, and air of the years 1900-1995, but with annual averages of the *aa* index [*Mayaud*, 1972, 1980; *Rangarajan*, 1989] as a proxy for the D_{st} index, and also with B-spline functions.

Spherical harmonic models of ionospheric fields have generally been produced separately from the other field contributions using data from magnetic observatories and variometer stations [see, e.g., *Matsushita and Maeda*, 1965; *Malin*, 1973; *Winch*, 1981; *Campbell*, 1989; *Olsen*, 1997b]. *Langel and Estes* [1985a] reported detection of Sq fields in the data from the POGO satellites. Attempts to model the EEJ affects in satellite data directly have been carried out by *Langel et al.* [1993], who first isolate the dip-latitude dependent fields via filtering and then fit with either zonal harmonics in dipole coordinates or other related empirical functions.

Global models of the lithospheric field are realizable only with satellite data, and have taken the form of various potential field representations. The usual approach has been to isolate the lithospheric field first by removing estimates of the main, ionospheric, and magnetospheric fields from the data and then correlating what is believed to be the remaining signal (see *Langel and Hinze* [1998] for details on recommended procedures). Though the exact methods may deviate from this, some examples of studies of this type can be found in *Arkani-Hamed and Strangway* [1985a, 1985b, 1986]; *Arkani-Hamed et al.* [1994]; *Ravat et al.* [1995]. A natural alternative is to include higher degree/order terms in the internal field potential expansion to capture the lithospheric contributions. *Cain et al.* [1984] followed this procedure in deriving a degree/order 29 internal field model from Magsat data corrected for both magnetospheric and ionospheric effects, and later, *Schmitz et al.* [1989] and *Cain et al.* [1989a, 1990] derive even higher degree ($\geq$ 50) expansions using improved ionospheric data corrections.

Currents at satellite altitude are responsible for the non-potential part of the magnetic field observed by satellites. Currents which couple the ionosphere with the magnetosphere flow in the ionospheric F-region at satellite altitude and therefore produce toroidal magnetic fields. *Takeda and Maeda* [1983] modeled the fields due to meridional currents as an F-region dynamo, but perhaps the best global model of the fields from these coupling currents comes from the work of *Olsen* [1997a], who represents them as a toroidal stream function expansion within the Magsat sampling shell under the assumption of radial currents only.

1.3 Comprehensive approach

Each of the studies cited in the previous section enjoy varying degrees of success in their ability to describe the target source field. They all, however, suffer at some level from the effects of frequency overlap between the spectra of the various source fields, both in the spatial and temporal domains. That is, frequency range cannot be used to absolutely distinguish between the spectra, and so bandpass and bandstop filters alone are doomed to either keep some of the unwanted signal or eliminate some of the signal of interest. Note that this is different from aliasing which is imposed by sampling intervals and results in signals with frequencies above the Nyquist being overlapped onto those at and below it [*Kanasewich*, 1981].

Evidently, additional information is needed to resolve the source contributions to near-Earth fields in a realistic manner. One possibility is to consider the radial positions of the various source regions relative to the available data. Core and lithospheric fields would be internal to both surface and satellite data while the magnetospheric field would be external. The ionospheric field would be external to surface data, but internal to satellite data. Thus, surface data could separate ionospheric and magnetospheric from core and lithospheric fields, and satellite data could separate magnetospheric from core, lithospheric, and ionospheric fields. This suggests that a joint analysis of both surface and satellite data could theoretically resolve parameterizations of all sources, but only if the parameter set is treated consistently between data types, which implies that they be coestimated. This simultaneous inversion for parameters describing all sources will be termed the "comprehensive approach", and models of this kind could provide the reference fields needed in more refined studies where source contamination is an issue.

This paper reports on the third in a series of efforts to derive progressively more sophisticated models using the comprehensive approach. The first phase, reported by *Sabaka and Baldwin* [1993], culminated in a model known as GSFC(12/93), while the second phase, reported by *Langel et al.* [1996], culminated in the GSFC(8/95-SqM) model. These models are based upon magnetically quiet data from the POGO and Magsat spacecraft and observatory annual and hourly means. Because of their limited scope, the Magsat vector data poleward of $\pm 50^\circ$ geomagnetic latitude is not used in order to avoid the auroral field-aligned currents (FAC's), while the Magsat dusk data is corrected for the effects of the EEJ and associated meridional currents. Details of the model parameterizations are given in Section 6.1, but qualitatively, both include representations of the main field, its secular variation, and the local time (sun synchronus) modes of the magnetospheric and ionospheric fields; both include ring-current variations through the proxy D_{st} index; and both include explicit parameterizations for fields induced by the time varying external fields. The GSFC(8/95-SqM) also includes seasonal variations in the magnetospheric and ionospheric fields.

The scope of the model presented in this paper is much wider and its attention to detail much higher than its predecessors. Being the culmination of the third phase of work along these lines, this model will be designated as "CMP3" (for "Comprehensive Model: Phase 3"). In the remainder of the paper, a description of the data, parameterization, and method of estimation leading to the CMP3 model will be given followed by a discussion of the model properties in terms of inverse theory and physical plausibility. In conclusion, model availability will be discussed and future directions will be outlined.

2 Data

The accuracy of models derived from inverse problems is intimately related to the quality of the data being analyzed. Undoubtably the best data to date for purposes of this study comes from the Magsat and POGO satellite missions and from the permanent magnetic observatories, which will now be discussed.

2.1 Observatories

The CMP3 model incorporates both annual and hourly means from permanent magnetic observatories. The former offers control of the main field secular variation over the Magsat and POGO mission duration envelopes, which is

discussed more in Section 3.1. Hence, the annual means are chosen within the interval 1960 to 1985 and are computed at the average time of the data over the particular year. These data are furnished by the National Geophysical Data Center (NGDC) in Boulder, CO, and are described in detail by *Langel and Baldwin* [1991].

The hourly means data are chosen from the magnetically quietest day of each month, as defined by K_p level, during the operational periods of the POGO (September 1965 to August 1971) and Magsat (November 1979 to May 1980) missions, though data through 1982 are also included. These data are furnished by NGDC, with augmented data from Winch, Faynberg and Singer, Olsen and others. Because the shortest time scale considered in the ionospheric and magnetospheric portions of the CMP3 model is 6 hr (see Sections 3.2 and 3.3), only hourly means data from every other hour are used. Before the hourly means data set was actually analyzed in the CMP3 model, it underwent an outlier rejection phase by visual inspection with respect to a model derived in the preliminary stages of this study. This process is discussed in more detail in Section 4.4.

Station breaks in time, introduced by *Langel et al.* [1982], are assigned by a visual inspection of the time series separately for the annual and hourly means. These breaks will usually coincide with a physical change in the nature of the measurements, such as a change in location, equipment, or local man-made fields. Thus, each station segment may be thought to have its own base line, which is estimated in the form of a vector bias as described in Section 3.1.

A synopsis of the hourly and annual means data sets is given in Appendix A via Tables 7-10 and 11-15, respectively. These tables provide information on station breaks (denoted by the root name with a roman numeral suffix), locations, time spans, and measurement counts per observatory. The CMP3 vector bias values and associated errors are also included and are discussed in detail in Section 6.2. The total measurement counts are listed in the *Number* column of Table 2, where the hourly means have been divided into those with dipole colatitude, θ_d, poleward or equatorward of $\pm 50°$. The spatial and temporal distributions of these data sets are shown in Fig. 1. The top panel shows that both hourly and annual means data are being analyzed at most station locations (triangles). The bottom panel shows that the annual means are close to being uniformly distributed across the time span of the model. Note here that the histograms are only recording the number of stations, including their breaks, that provide measurements within a one year bin, and not the total number of measurements, in which case the hourly counts would dwarf those of the annual.

2.2 Magsat

The Magsat data sets used in the CMP3 model are mainly those dawn and uncorrected dusk data sets used in deriving the GSFC DAWN(6/83) and DUSK(6/83) models of *Langel and Estes* [1985a], respectively. Though these data sets are described in detail by *Langel and Baldwin* [1991], a brief synopsis of the processing is given here: The Magsat data were initially screened with the three-hourly K_p index by choosing only data with corresponding $K_p < 1^-$ and previous $K_p \leq 2^o$. Vector data poleward of $\pm 50°$ dipole latitude were excluded to minimize the effects of field-aligned and ionospheric currents in the auroral regions. Scalar intensity data were retained at all latitudes. A data selection algorithm was then applied separately for both the dawn and dusk data within a ± 20 nT D_{st} level for the time intervals of November and December, 1979; January and February, 1980; and March and April, 1980. The objective of the algorithm was to obtain a uniform data distribution in both time and space. Finally, after the elimination of outliers with respect to the GSFC(9/80) model, passes from slightly more disturbed times were added to sparse regions in order to improve geographic coverage. These data sets will be referred to simply as the "Magsat dawn" and "Magsat dusk" data sets.

The CMP3 model represents a significant advancement in how fields of external origin, such as those from ionospheric coupling and EEJ currents, are parameterized. It is then desirable to include high (poleward of $\pm 50°$) geomagnetic latitude vector data in the analysis, particularly the X and Y components which are sensitive to high latitude field-aligned currents. Accordingly, X and Y vector components were added at sampling points poleward of $\pm 50°$ corresponding to those already providing scalar measurements in the CMP3 Magsat dawn and dusk data sets. These new data sets will be referred to as the "Magsat polar dawn" and "Magsat polar dusk" data sets.

Before the Magsat dawn, polar dawn, dusk, and polar dusk data sets were actually analyzed in the CMP3 model, they underwent an additional episode of refinement via the rejection of outliers with respect to a model derived in the

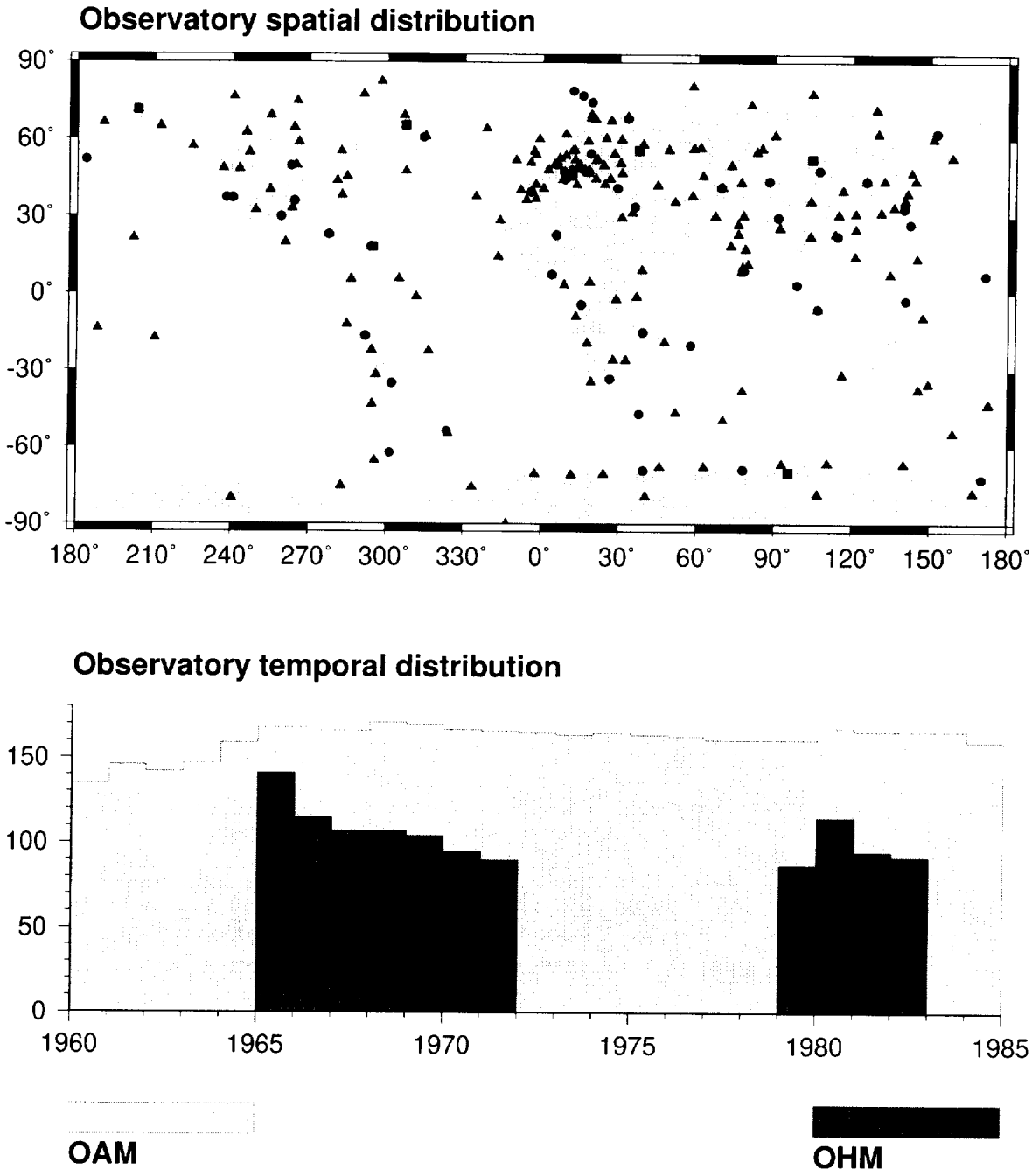

Figure 1: Observatory hourly mean (OHM) and annual mean (OAM) spatial and temporal distributions. The top panel shows observatory locations where only OHM (squares), only OAM (circles), or both (triangles) data types are used in the CMP3 model (Cylindrical Equidistant projection). The bottom panel shows a histogram of the number of OHM and OAM stations contributing data to that particular one year bin across the time span of the CMP3 model.

preliminary stages of this study. This process is discussed in more detail in Section 4.4, and the resulting measurement counts for these data sets are listed in the *Number* column of Table 2.

2.3 POGO

The bulk of the parent POGO (Polar Orbiting Geophysical Observatories, comprised of the OGO-2, OGO-4, and OGO-6 satellites, see *Langel* [1974]) data sets from which those used in the CMP3 model were extracted were also used to derive the POGO(2/72) field model [*Langel et al.*, 1980], with additional OGO-6 data from 1969 to 1971 for magnetically quiet to moderately quiet times. These parent data sets, described in detail by *Langel and Baldwin* [1991], were found to have an uneven distribution in local time and to be somewhat larger than necessary for this study. Therefore, these data sets were decimated in order to achieve a more uniform geographic and magnetic local time (MLT) distribution, and a more managable size. Furthermore, the same outlier rejection phase was applied to POGO data as to Magsat data, details of which are found in Section 4.4. The resulting data sets will be referred to collectively as the "POGO decimated" data set. The MLT distribution of this data set is shown in the bottom panel of Fig. 2 as a histogram of the number of measurement positions falling within one-hour MLT bins. Of the total 22685 positions, the most (1509) fall between 1:00 and 2:00 am and the least (390), unfortunately, fall between 12:00 and 1:00 pm.

Historically, the mechanism used for the POGO decimated data set did not admit entire satellite tracks. Much of the external field current systems is transient and, while this distribution probably gives a broad sampling of those variations, it may not give coherent data tracks across these patterns. Because of this, it is felt that some advantage might be gained by incorporating some individual passes of data. Accordingly, a selection of data from typical passes from quiet periods has been made. These data were also put through the outlier rejection phase, which resulted in 6754 measurements from 170 passes. This data set is referred to as the "POGO pass" data set. The angular positions of the pass loci are shown in the top panel of Fig. 2, and a histogram of the number of passes that cross the geographic equator within one-hour MLT bins is shown in the middle panel. The spatial and temporal distributions appear to be sufficient to sample most of the Sq and EEJ features of the ionospheric current systems.

3 Parameterization of field sources

As alluded to earlier, the ultimate worth of the CMP3 model lies in its ability to properly describe as much of the intended signal as possible in the data. These data, however, are limited in their spatial and temporal sampling of the field and are contaminated at some level by systematic and random error processes. An efficient model parameterization will take these limitations into account in order to achieve optimal results. The parameterizations used in this study are now described by source.

3.1 Core and lithospheric fields

The current systems responsible for both the core and lithospheric magnetic fields lie entirely below the regions sampled by permanent observatories and satellites. Therefore, these fields may be expressed as gradients of internal potential functions of the form:

$$V = \Re \left\{ a \sum_{n=1}^{N_{max}} \sum_{m=0}^{n} \left(\frac{a}{r}\right)^{n+1} \gamma_n^m Y_n^m(\theta, \phi) \right\} \tag{1}$$

with:

$$Y_n^m = P_n^m(\theta) \exp im\phi \tag{2}$$

where a is the mean radius of the Earth (6371.2 km), (r,θ,ϕ) are the usual geographic spherical polar coordinates, and Y_n^m and P_n^m are the Schmidt normalized surface spherical harmonic and associated Legendre function of degree n and

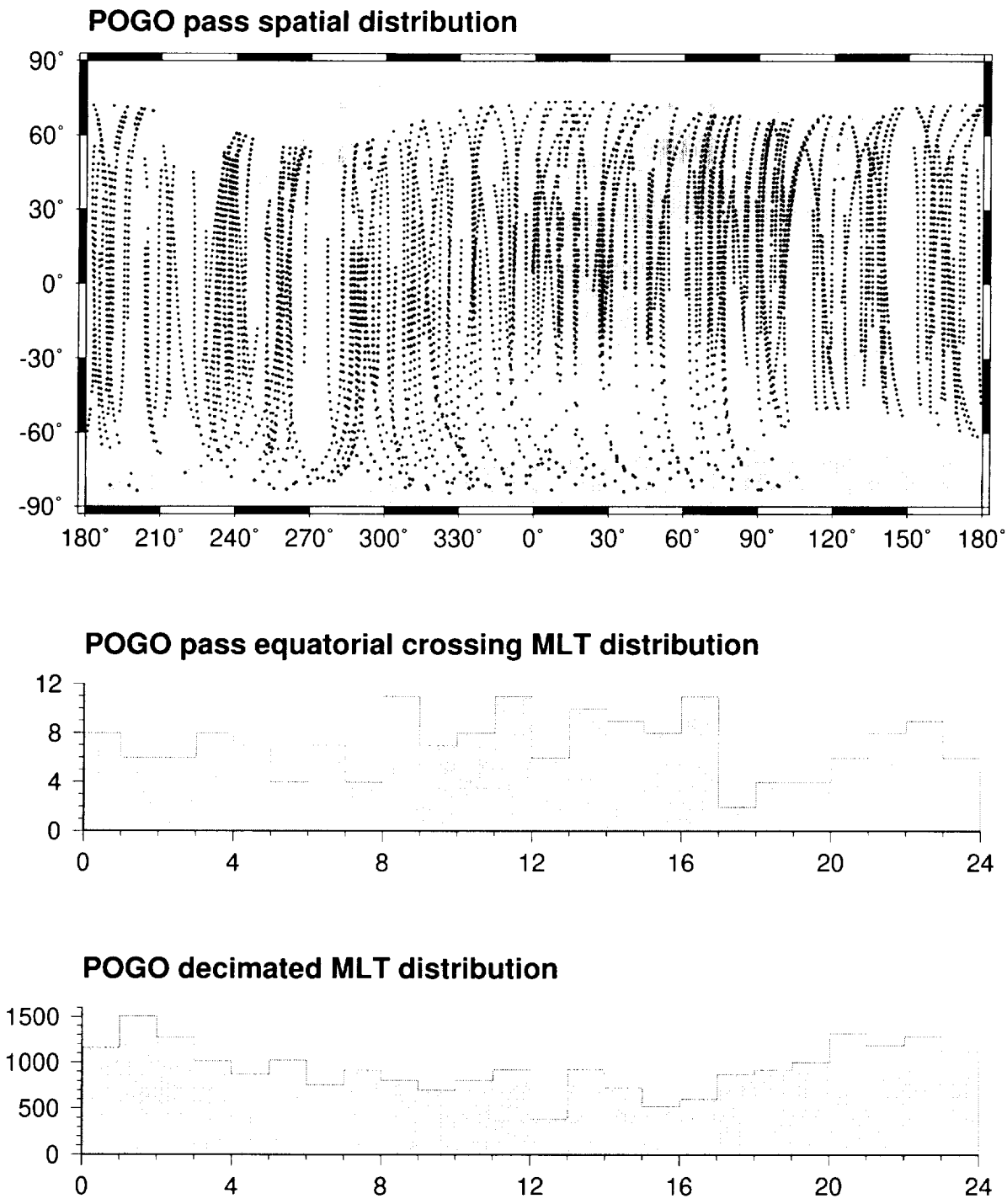

Figure 2: POGO satellite spatial and temporal distributions. The top panel shows the angular positions of the pass loci for the POGO pass data set (Cylindrical Equidistant projection). The middle panel shows a histogram of the number of passes from the POGO pass data set that cross the geographic equator within a particular one hour magnetic local time (MLT) bin. The bottom panel shows a histogram of the number of measurement positions in the POGO decimated data set that fall within a particular one hour MLT bin.

order m, respectively [e.g. *Langel*, 1987]. The $\Re\{\cdot\}$ operation takes the real part of the expression only. Hence, the γ_n^m are unique complex expansion coefficients, also known as Gauss coefficients. They are related to the usual real Gauss coefficients g_n^m and h_n^m according to $\gamma_n^m = g_n^m - ih_n^m$. Typically, terms in Eq. 1 have been retained only up to a degee truncation level, N_{max}, that is justified by the data, or in the case of satellites, up to that degree at which it is believed that the lithospheric field begins to dominate the series, otherwise known as the main field portion of the spectrum, taken by *Langel and Estes* [1982] to be 13. Spherical harmonic models of lithospheric fields have been derived from data with estimates of the main, magnetospheric, and ionospheric fields removed. Such models indicate that noise becomes dominant somewhere between $N_{max} = 60$ to 70 [*Ravat et al.*, 1995]. That noise, however, reflects also an inaccurate estimation of the other fields. One of the intentions of the present study is to examine whether a combined model can be more effective in accurately representing the lithospheric field. To this end, the degee truncation level for this model is set at $N_{max} = 65$.

The main field is mostly dominated by contributions which originate in the core region of Earth. Advection of magnetic field lines by the highly conductive fluid in the outer core sustains the field against Ohmic decay. The consequence of this dynamo action is that the main field varies with time scales on the order of centuries. Variations with time scales shorter than a year or two are effectively screened by finite mantle conductivity, and as a result, are not detectable at Earth's surface. *Sabaka et al.* [1997] modeled the longer time scale variations of the main field by parameterizing its first temporal derivative, commonly known as secular variation, with cubic B-splines.

Briefly, if $\{\tau_i, i = 1, \ldots, m\}$ are a set of strictly increasing real numbers, and if $s(t)$ is a polynomial of degree $k-1$ in each of the intervals $\tau_{i-1} < t \leq \tau_i, i = 2, \ldots, m$, and if $s(t)$ and its first $k-2$ derivatives are continuous, then $s(t)$ is a spline of order k with knot set $\{\tau_i\}$. A k-th order B-spline, $b_q^k(t)$, is a special case in which $s(t)$ is non-zero over only k adjacent knot intervals, $\tau_q < t \leq \tau_{q+k}$, of the knot set $\{\tau_i, i = 1, \ldots, h+2k\}$. The h knots $\{\tau_i, i = k+1, \ldots, h+k\}$ are called interior knots. Furthermore, $b_q^k(t)$ is positive-valued over $\tau_q < t \leq \tau_{q+k}$, has a single maximum, and joins the t-axis with its first $k-2$ derivatives equal to zero at $t = \tau_q$ and $t = \tau_{q+k}$ [*Schumaker*, 1981]. The B-spline functions provide a suitable temporal basis for the secular variation of the Gauss coefficients, which are now time dependent:

$$\frac{d\gamma_n^m(t)}{dt} = \sum_{q=1}^{h+k} \gamma_{nq}^m b_q^k(t) \tag{3}$$

leading to:

$$\gamma_n^m(t) = \gamma_n^m(e) + \sum_{q=1}^{h+k} \gamma_{nq}^m \int_e^t b_q^k(\tau) d\tau \tag{4}$$

$$= \gamma_{n0}^m + \sum_{q=1}^{h+k} \gamma_{nq}^m \left[\frac{\tau_{q+k} - \tau_q}{k} \left\{ \sum_{j=q}^{h+k} \left(b_j^{k+1}(t) - b_j^{k+1}(e) \right) \right\} \right] \tag{5}$$

where e is the epoch or expansion point for the series, and the γ_{nq}^m are the unique complex coefficients of the series. This approach is adopted here with $k = 4$, for cubic B-splines, and $e = 1980$, for the Magsat epoch, for all $\gamma_n^m(t)$. Because both POGO and Magsat satellite data will be included in the analysis, the time span of the model is chosen to be 1960-1985, allowing for an extension at either end of the missions. Given that the spline knot set must be defined over the entire time envelope, and choosing an equi-spaced knot distribution at 2.5 yr intervals for all $\gamma_n^m(t)$, this results in a value of $h = 9$ and a total of $h + k = 13$ cubic B-splines per $\gamma_n^m(t)$. Including the offset, γ_{n0}^m, this gives a total of 14 parameters describing the temporal behavior of each $\gamma_n^m(t)$.

Assuming that the temporal variation of terms with $n > 13$ is negligible for the present model, the final working expression for the core and lithospheric potential is given by:

$$V = \Re \left\{ a \sum_{n=1}^{13} \sum_{m=0}^{n} \sum_{q=0}^{13} \left(\frac{a}{r} \right)^{n+1} \gamma_{nq}^m Y_{nq}^m + a \sum_{n=14}^{65} \sum_{m=0}^{n} \left(\frac{a}{r} \right)^{n+1} \gamma_n^m Y_n^m \right\} \tag{6}$$

with:

$$Y_{nq}^m = \begin{cases} Y_n^m & \text{for } q = 0; \\ Y_n^m \int_{1980}^t b_q^k(\tau) d\tau & \text{for } q > 0. \end{cases} \tag{7}$$

The number of real coefficients in the main and lithospheric field model expansions are 2730 and 4160, respectively, which gives a total of 6890 real coefficients in this portion of the CMP3 model.

In order to resolve the secular variation of the main field, it is imperative that the data provide good spatial and temporal coverage over the time span of interest. Though permanent magnetic observatories may lack in the former, they are very well suited to the latter by continuously measuring the field at one location. In this study, observatory hourly means are analyzed which are cotemporaneous with the POGO and Magsat mission envelopes. Though they provide crucial information about external and induced fields, their time distribution limits their ability to resolve secular variation. Therefore, observatory annual means, whose collective distribution spans the entire 1960-1985 time envelope, are also included in the analysis.

Consider now that permanent magnetic observatories are located on the outer surface of the lithosphere, and being in such close proximity makes them extremely sensitive to the short wavelength field of the lithosphere. Even at $N_{max} = 65$ there is undoubtedly deviation of the predicted from the actual field due in part to power in the lithospheric field at higher degrees. If deviations due to random error are handled properly, then the remaining systematic deviations are point-sampled by the observatories and can be represented by a local vector bias, $\underline{B}_{bias}$, as introduced by *Langel et al.* [1982]. There are 506 individual observatory time series in the combined annual and hourly means data sets for which a full vector bias is estimated. Due to data quality issues, only the horizontal bias components of the hourly means are estimated at Amberley II and San Fernando. Conversely, only the vertical hourly means are used at Amatsia, and hence, only this component of the bias is estimated here. This accounts for another 1523 real coefficients in the model.

3.2 Ionospheric field

The morphology of geomagnetic variations produced by the ionospheric dynamo is relatively fixed in magnetic local time. However, within this basic morphology there is considerable variation depending upon other phenomena such as season, solar cycle, interactions with Earth's main field, etc. It is assumed that the primary currents flow horizontally in the ionospheric E-region at an altitude of $h = 110$ km. Therefore, the equivalent currents are equal in effect to the real currents. Because these fields vary with time, there are corresponding induced currents in the Earth, with attendant fields. Since the measurements used are not acquired in the regions where the source currents flow, the fields can be represented by gradients of potential functions. The basis functions representing the ionospheric and associated induced potentials are best understood as being built from a set of "elemental" potential functions reflecting a single spatial harmonic modulated by single seasonal and diurnal periods. For the region between the Earth's surface, $r = a$, and the location of the ionospheric equivalent current sheet, $r = a + h$, these have the following form:

$$V^m_{nsp} = \Re\left\{ a \left[\iota^m_{nsp} \left(\frac{a}{r}\right)^{n+1} + \epsilon^m_{nsp} \left(\frac{r}{a}\right)^n \right] P^m_n(\theta_d) \exp i(m\phi_d + \omega_s s t + \omega_p p t_m) \right\} \tag{8}$$

where θ_d and ϕ_d are dipole colatitude and longitude, respectively. The fundamental seasonal angular frequency is $\omega_s = 2\pi$ rads/yr with associated wavenumber s and time of year t counted from January 1, 00 UT. The fundamental diurnal angular frequency is $\omega_p = 2\pi/24$ rads/hr with associated wavenumber p and magnetic universal time (MUT) t_m. Hence, the ϵ^m_{nsp} and ι^m_{nsp} are unique complex expansion coefficients of the external ionospheric and the internal induced potentials, respectively, having a single spatial harmonic as prescribed by n and m, which oscillates on two time scales as prescribed by s and p, and propagates in one direction as prescribed by the relative signs of s, p, and m.

A brief digression is in order such that the nature of magnetic local and universal time may be explained in the context of this study. The magnetic local time, t_{mlt}, of an observer is defined as:

$$t_{mlt} = (180^\circ + \phi_{d,o} - \phi_{d,s})/15 \tag{9}$$

where if the dipole longitude of the observer, $\phi_{d,o}$, and the sub-solar point, $\phi_{d,s}$, are in degrees, then t_{mlt} is in hours. Dipole longitude in measured in the dipole equatorial plane in a positive sense from a line extending from Earth's center into the half-plane defined by the dipole and geographic axes and containing the south geographic pole. The tilted dipole from the GSFC(12/83) model [*Langel and Estes*, 1985b], whose north magnetic dipole position is

$(\theta = 11.2°, \phi = 289.3°)$, is used to assign dipole longitudes to data in this study. The position of the sub-solar point is calculated from routines provided in *Russell* [1971]. The magnetic universal time is defined as the MLT of the dipole prime meridian, the meridian from whence dipole longitude is rendered. Hence, it is given by:

$$t_m = (180° - \phi_{d,s})/15 \tag{10}$$

where $\phi_{d,o}$ is now zero. To clarify, Eq. 9 is given incorrectly in *Langel* [1987] and *Langel and Hinze* [1998].

At this point one could define an ensemble of V^m_{nsp} as the working form of the ionospheric and associated induced potentials. However, incorporating a few conditions gained from some basic physical insights can drastically reduce the number of free parameters in this part of the model. To facilitate the discussion, consider an ensemble of V^m_{nsp} across n and m for fixed s and p:

$$V_{sp} = \sum_{n,m} V^m_{nsp} \tag{11}$$

or in matrix notation:

$$V_{sp} = \Re\left\{\underline{\epsilon}^H \underline{S}_e + \underline{\iota}^H \underline{S}_i\right\} \tag{12}$$

where $\underline{\epsilon}$ and $\underline{\iota}$ are the vectors of $(\epsilon^m_{nsp})^*$ and $(\iota^m_{nsp})^*$, respectively. The super-scripted asterisk and H denote complex conjugation and Hermatian conjugation, respectively. The $\underline{S}_e$ and $\underline{S}_i$ are vectors with elements given, respectively, by:

$$S^m_{nsp,e} = a\left(\frac{r}{a}\right)^n P^m_n(\theta_d) \exp i(m\phi_d + \omega_s s t + \omega_p p t_m) \tag{13}$$

$$S^m_{nsp,i} = a\left(\frac{a}{r}\right)^{n+1} P^m_n(\theta_d) \exp i(m\phi_d + \omega_s s t + \omega_p p t_m) \tag{14}$$

The first insight that can be made is that $\underline{\iota}$ is in general not independent of $\underline{\epsilon}$. The nature of this dependence is related to the conductivity structure of the crust and upper mantle, which leads to the following linear relationship:

$$\iota^l_{ksp} = \sum_{n,m} q^{lm}_{knsp} \epsilon^m_{nsp} \tag{15}$$

or in matrix notation:

$$\underline{\iota} = Q\underline{\epsilon} \tag{16}$$

where Q is a complex matrix representation of the transfer function between the driving ionospheric signal and the driven induced signal [*Schmucker*, 1985; *Olsen*, 1999]. There is a one-to-one correspondence between induced and inducing frequencies, i.e. Q maps between $\underline{\epsilon}$ and $\underline{\iota}$ of like frequencies. For a general three-dimensional mantle conductivity, the Q matrix, as written in Eq. 16, is dense. However, for purposes of this model a one-dimensional conductivity distribution, i.e. depending only on radius, of *Olsen* [1998] has been adopted. It is a four-layer conductivity model derived from Sq and Dst data at selected European observatories. The consequences on Q are that it is now diagonal and its elements do not depend upon longitudinal wavenumber m, but only upon n and the frequency f. This means that one external coefficient induces only one internal coefficient, i.e. $\iota^m_n = q^{mm}_{nn}(f)\epsilon^m_n$. Furthermore, for matrix element $q^{mm}_{nn}(f)$, the theoretical range of magnitude is $0 \leq |q^{mm}_{nn}(f)| \leq \frac{n}{n+1}$ while causality relationships imply $\Re\{q^{mm}_{nn}(f)\} \geq 0$ and $\Im\{q^{mm}_{nn}(f)\} \geq 0$.

The temporal variation of the working ionospheric and associated induced potentials consists of various combinations of modulated seasonal and diurnal frequencies. The fields induced from higher frequencies will generally dominate those from lower. Therefore, for simplicity, a single frequency (the highest of the diurnal-seasonal modulation) may be assigned to the matrix elements operating on ϵ^m_{nsp}, which leads to the following assignment rules:

$$q^{mm}_{nn}(f) = \begin{cases} 0 & \text{for } p = 0 \text{ and } s = 0; \\ q^{mm}_{nn}(0) & \text{for } p = 0 \text{ and } s > 0; \\ q^{mm}_{nn}(p) & \text{for } p > 0\,. \end{cases} \tag{17}$$

Note that $f = 0$ is formally used to designate "very long-period" rather than an absence of oscillation, in which case $q^{mm}_{nn}(f \to 0) = 0$. This is indeed true for the purely seasonal versus diurnal oscillations included in the model. For deriving the "very long-period" response $q^{mm}_{nn}(f \to 0)$, the mantle is assumed to be an insulator in the region

$a - \delta \leq r \leq a$ and superconducting in $r < a - \delta$. At the surface of a superconductor, the radial component of the magnetic field has to vanish. It follows from Eqs. 8 and 15 that:

$$q_{nn}^{nm}(f \to 0) = \left(\frac{n}{n+1}\right)\left(\frac{a-\delta}{a}\right) \tag{18}$$

For this study, a value of $\delta = 1000$ km is used, corresponding to induction with periods longer than one week or so.

A second insight is that many ionospheric phenomena are naturally organized with respect to the geometry of Earth's magnetic field due to its influence on the motion of charged particles. As a consequence, ionospheric conductivity is highly anisotropic, resulting in values that are so high parallel to the field that the magnetic field lines are nearly equipotential lines. Therefore, it is often convenient to work in a coordinate system that is aligned with the magnetic field, such as the "Quasi-Dipole" (QD) coordinates (θ_q, ϕ_q) proposed by *Richmond* [1995]. If one could exploit the symmetries of such a coordinate system by building them into the basis functions, then clearly a great savings would be realized in the number of free parameters that would need to be estimated. For example, modeling the EEJ with spherical harmonics expanded in dipole coordinates requires both high degree and order terms because of the undulation of the EEJ in longitude, i.e. it does not follow lines of constant θ_d. However, the EEJ is always located at $\theta_q = 90^\circ$, and therefore one may be able to fit this feature with far fewer of the proposed functions.

Before embarking on this course, however, certain properties of the QD coordinates must be articulated. First, the Laplacian operator does not separate in QD coordinates, rendering closed-form solutions out of the question. Secondly, though the QD colatitude, θ_q, and longitude, ϕ_q, do chart the sphere, their coordinate lines change with radius, r. With this in mind, consider a set of basis functions which possess the QD symmetry in two dimensions rather than three, perhaps on a constant-coordinate surface. If a sphere is chosen, then it is natural to think of the QD angular coordinates as the formal arguments to the usual surface harmonics. Though these functions are neither orthogonal nor complete on the sphere, they do possess the desired QD symmetry and should suffice for the resolution requirements of the model. Furthermore, these functions may be expanded in terms of the surface harmonics in dipole coordinates:

$$P_k^l(\theta_q)\exp il\phi_q \quad \sum_{n=1}^{N_{max}} \sum_{m=-\min(n,M_{max})}^{\min(n,M_{max})} (d_{kn}^{lm})^* P_n^m(\theta_d)\exp im\phi_d \tag{19}$$

where $\theta_q = \theta_q(r, \theta_d, \phi_d)$, $\phi_q = \phi_q(r, \theta_d, \phi_d)$, and $d_{kn}^{l\ \ -m} = (d_{kn}^{lm})^*$. The regression coefficients, d_{kn}^{lm}, are determined by a standard spherical transform, where N_{max} and M_{max} are chosen such that sufficient convergence is achieved. It is also very easy to introduce temporal oscillations to these functions of the kind seen in Eqs. 13 and 14 by simply multiplying by the appropriate complex exponential, e.g. $\exp i(\omega_s st + \omega_p pt_m)$.

As stated earlier, an attempt to define a radial dependence for the functions in Eq. 19 such that they satisfy Laplace's equation in QD coordinates is fruitless. If one settles for radial dependencies found in Eqs. 13 and 14, then the new functions will satisfy Laplace's equation in dipole coordinates for external and internal sources, respectively, and will exhibit the desired QD symmetry on a given sphere. It remains then to decide which sphere. Since $r = a + h$, with $h = 110$ km, is the approximate height of the ionospheric E-region current system where most of the features of interest are located, then this should be a satisfactory choice. Hence, in view of Eqs. 13, 14, and 19, one can construct the desired basis functions for potentials in the region $a \leq r \leq a + h$:

$$T_{kspc}^{l} = \sum_{n,m} (d_{kn}^{lm})^* \left(\frac{a}{a+h}\right)^{n+1} S_{nspc}^{m} \tag{20}$$

$$T_{ksps}^{l} = \sum_{n,m} (d_{kn}^{lm})^* \left(\frac{a+h}{a}\right)^{n+2} S_{nsps}^{m} \tag{21}$$

where summation over n and m is understood from Eq. 19. Clearly then:

$$T_{kspc}^{l}|_{r=a+h} \quad T_{kspc}^{l}|_{r=a+h} = (a+h)P_k^l(\theta_q)\exp i(l\phi_q + \omega_s st + \omega_p pt_m) \tag{22}$$

A global plot of $\Re\left\{T_{45,0,0,c}^{3}\right\}|_{r=a+h}$ is shown in Fig. 3 which illustrates the QD geometry on the sphere where the ionospheric currents are assumed to flow. The reference model used to define the QD coordinate system in this figure and for this study is the IGRF 1980 model [*IAGA Division I Working Group 1*, 1981].

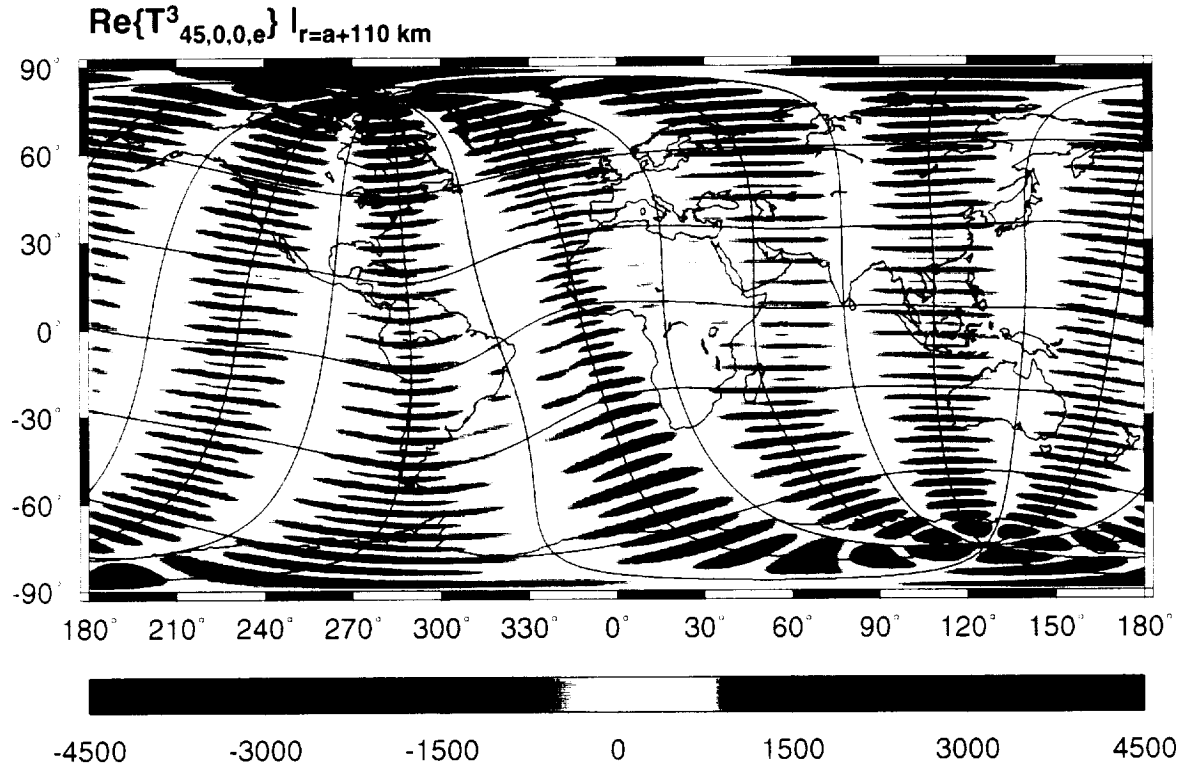

Figure 3: The function $\Re\left\{T^3_{45,0,0,e}\right\}$ evaluated on the sphere $r = 6481.2$ km (Cylindrical Equidistant projection). The reference model used to define the QD coordinate system is the IGRF 1980 model [*IAGA Division I Working Group I*, 1981]. The θ_q and ϕ_q coordinate lines are also shown in 30° increments.

It follows that a new set of "elemental" potential functions, analogous to those of Eq. 8, may be defined from Eqs. 20 and 21:

$$V^l_{ksp} = \Re\left\{\tilde{\iota}^l_{ksp} T^l_{ksp,i} + \tilde{\epsilon}^l_{ksp} T^l_{ksp,e}\right\} \tag{23}$$

Again, consider an ensemble of V^l_{ksp} across k and l for fixed s and p:

$$V_{sp} = \sum_{k,l} V^l_{ksp} \tag{24}$$

or in matrix notation:

$$\begin{aligned} V_{sp} &= \Re\left\{\underline{\tilde{\epsilon}}^H \underline{T}_e + \underline{\tilde{\iota}}^H \underline{T}_i\right\} && (25)\\ &= \Re\left\{\underline{\tilde{\epsilon}}^H D^H U_e \underline{S}_e + \underline{\tilde{\iota}}^H D^H U_i \underline{S}_i\right\} && (26)\\ &= \Re\left\{\underline{\tilde{\epsilon}}^H D^H_e \underline{S}_e + \underline{\tilde{\iota}}^H D^H_i \underline{S}_i\right\} && (27) \end{aligned}$$

where $\underline{\tilde{\epsilon}}$ and $\underline{\tilde{\iota}}$ are the vectors of $(\tilde{\epsilon}^l_{ksp})^*$ and $(\tilde{\iota}^l_{ksp})^*$, respectively, $\underline{T}_e$ and $\underline{T}_i$ are the vectors of $T^l_{ksp,e}$ and $T^l_{ksp,i}$, respectively, D is the matrix of d^{lm}_{kn} regression coefficients in Eq. 19, and U_e and U_i are real matrix representations of the upward-continuation operators for external and internal fields in Eqs. 20 and 21, respectively. It is now clear that imposing the QD symmetry at $r = a + h$ imposes a linear constraint on the original expansion coefficients:

$$\begin{aligned} \underline{\epsilon} &= D_e \underline{\tilde{\epsilon}} && (28)\\ \underline{\iota} &= D_i \underline{\tilde{\iota}} && (29) \end{aligned}$$

So far, only magnetic field measurements made within the shell between Earth's surface and the ionospheric sheet current, $a \le r \le a + h$, have been considered. However, a large number of measurements are made by the Magsat and POGO satellites in the region $a + h < r$, and so the ionospheric and associated induced potentials must be defined here also. With the induced potential remaining essentially intact, the major difference comes from the fact that the ionosphere is now internal to the measurement region. Hence, Eq. 12 becomes:

$$V'_{sp} = \Re\left\{\left(\underline{\epsilon}'^H + \underline{\iota}^H\right) \underline{S}_i\right\} \tag{30}$$

where the prime denotes quantities that now apply to the region $a + h < r$. Obviously the same QD symmetry is desired at $r = a + h$ as before, which leads to the following constraints:

$$\begin{aligned} \underline{\epsilon}' &= D_i \underline{\tilde{\epsilon}}' && (31)\\ \underline{\iota} &= D_i \underline{\tilde{\iota}} && (32) \end{aligned}$$

The ionospheric potentials above and below the sheet source are by no means independent because the radial components of the resulting fields are continuous across the sheet. This is a result of applying Gauss's theorem to the field in a volume of infinitesimal thickness, centered on $r = a + h$. The formal boundary condition is given by:

$$\frac{\partial V}{\partial r}\Big|_{r=a+h^-} = \frac{\partial V}{\partial r}\Big|_{r=a+h^+} \tag{33}$$

where h^- and h^+ refer to positions just below and above the sheet current, assumed to have zero thickness. All this implies a linear relationship between the expansion coefficients of the two potentials, given by:

$$\epsilon^{m\prime}_{nsp} = -\left(\frac{n}{n+1}\right)\left(\frac{a+h}{a}\right)^{2n+1} \epsilon^m_{nsp} \tag{34}$$

or in matrix notation:

$$\underline{\epsilon}' = C\underline{\epsilon} \tag{35}$$

where C is a real diagonal matrix.

At this point, several linear relationships have been established between the various sets of expansion coefficients. These must now be woven together in a consistent fashion. Because they are exact, these relationships can be built

directly into the model parameter space, thus decreasing the number of free parameters in an *a priori* deterministic way. First, consider the region $a \leq r \leq a+h$, where the induction condition (Eq. 16) and the QD constraints (Eqs. 28 and 29) apply. The goal is to solve for $\underline{\epsilon}$ and $\underline{\iota}$ in terms of $\underline{\tilde{\epsilon}}$, the reduced parameter set. The former is already provided by Eq. 28. The latter is more complicated. Substituting Eq. 28 into Eq. 16 and recalling that Eq. 29 restricts $\underline{\iota}$ to lie in the column space of D_i leads to the following expression:

$$\underline{\iota} = D_i D_i^+ Q D_e \underline{\tilde{\epsilon}} \tag{36}$$

where:

$$D_i^+ = \left(D_i^H D_i\right)^{-1} D_i^H \tag{37}$$

under the assumptions that D_i has more rows than columns and that its rank is equal to its column number. The D_i^+ matrix is the "pseudo-inverse" of D_i and the $D_i D_i^+$ matrix is a projection matrix onto the column space of D_i.

A subtle caveat exists, however, in Eq. 36 in that although the QD constraint is always satisfied, the induction condition is only simultaneously satisfied when the column space of QD_e is a proper subset of the column space of D_i. To resolve this problem, one is forced to complete the column space of D_i by admitting as many $T^l_{ksp,i}$ functions as $S^m_{nsp,i}$, i.e. making D_i a square matrix. Assuming the $T^l_{ksp,i}$ are linearly independent, this makes the projection operator an identity operator, which gives:

$$\underline{\iota} = Q D_e \underline{\tilde{\epsilon}} \tag{38}$$

$$= F \underline{\tilde{\epsilon}} \tag{39}$$

Substituting into Eq. 12 gives the constrained potential for this region:

$$V_{sp} = \Re\left\{\underline{\tilde{\epsilon}}^H \left(D_e^H \underline{S}_e + F^H \underline{S}_i\right)\right\} \tag{40}$$

It should be noted that although Eq. 29 still formally holds under a square D_i matrix of full rank, it no longer implies a constraint (a decrease in the number of free parameters), but merely a change of basis. Also, a square D_i matrix does not imply a square D_e matrix, their column dimensions are totally independent.

Now, consider the region $a + h < r$, where the induction condition (Eq. 16), the QD constraints (Eqs. 28, 29, and 31), and the radial continuity condition (Eq. 35) apply. Again, the goal is to solve for $\underline{\epsilon}'$ and $\underline{\iota}$ in terms of $\underline{\tilde{\epsilon}}$. This time the latter is provided by Eq. 39. Solving the former is completely analogous to solving for $\underline{\iota}$ in terms of $\underline{\tilde{\epsilon}}$ above, along with the same caveat. Here, the radial continuity condition would replace the induction condition and Eq. 31 would replace 29. Therefore:

$$\underline{\epsilon}' = C D_e \underline{\tilde{\epsilon}} \tag{41}$$

$$= G \underline{\tilde{\epsilon}} \tag{42}$$

Substituting into Eq. 30 gives the constrained potential for this region:

$$V'_{sp} = \Re\left\{\underline{\tilde{\epsilon}}^H \left(G^H + F^H\right) \underline{S}_i\right\} \tag{43}$$

The next item to be addressed is the dependence of ionospheric contributions on solar activity. In a paper on the variability of geomagnetic daily variations with solar activity, *Olsen* [1993] estimates the proportionality M between the coefficients of a spherical harmonic analysis of the variations and sunspot number, R. Solar flux, however, is probably a better parameter for describing the short term variability of solar activity of the kind encountered in this study. Together, these motivate a functional dependence of the ionospheric expansion coefficients on the solar radiation flux index, $F_{10.7}$, that is linear. Specifically, a new set of expansion coefficients is defined such that:

$$\tilde{\epsilon}^l_{ksp} = \tilde{\varepsilon}^l_{ksp} \cdot \left(1 + N \cdot F_{10.7}\right) \tag{44}$$

The proportionality N is not solved for, but rather an independently estimated *a priori* value is used, which is assumed to be equal for all coefficients. This means that increasing solar flux inflates the whole ionospheric current system (and induced contributions) without changing its shape. To estimate N, the technique of *Olsen* [1993] was used, but with solar flux $F_{10.7}$ instead of sunspot number R. Correlation between 20 annual means of $\left|\epsilon^1_2\right|$, the amplitude of the

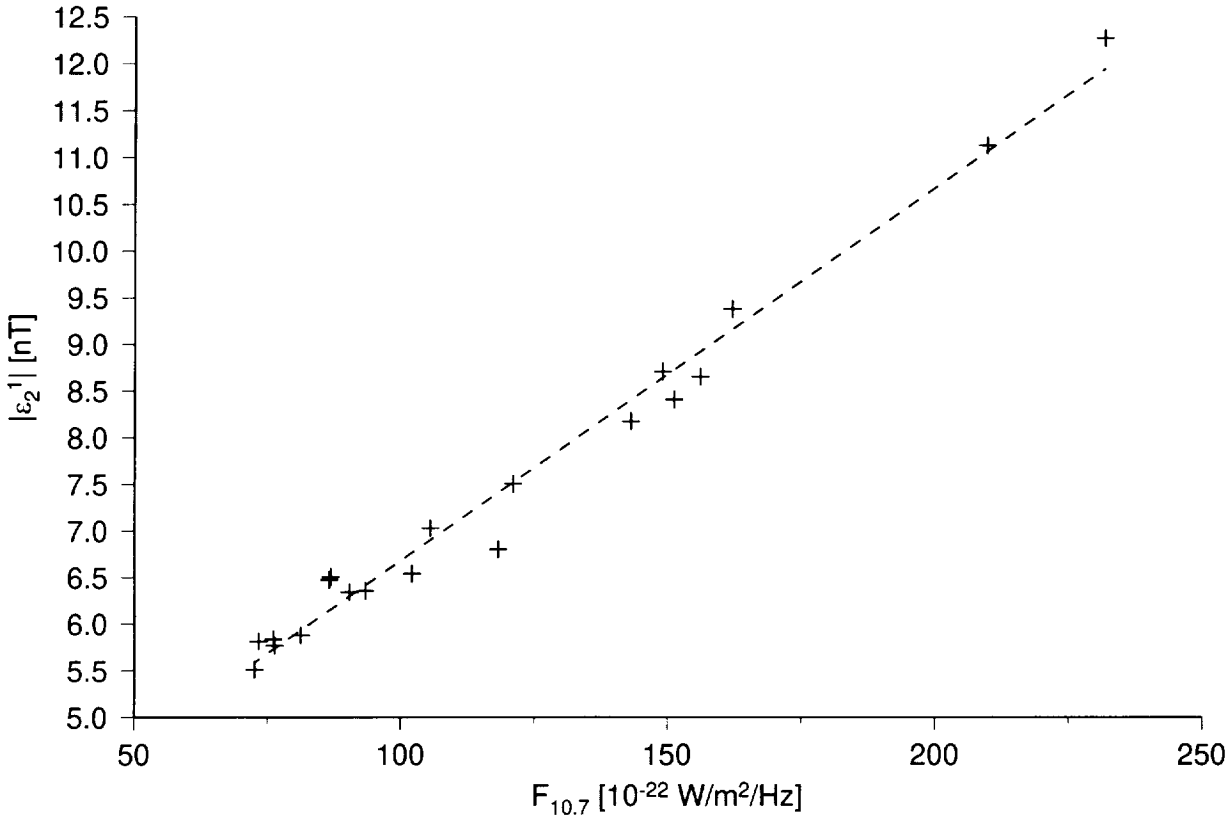

Figure 4: Plot of $F_{10.7}$ versus amplitude of the diurnal main term $\left|\epsilon_2^1\right|$ and linear regression from *Olsen* [1993]. The ratio of slope to $\left|\epsilon_2^1\right|$-intercept of the regression is $N = 14.85 \cdot 10^{-3} \left[10^{-22}\mathrm{W/m^2/Hz}\right]^{-1}$.

diurnal main term, and solar flux $F_{10.7}$ yields a value of $N = 14.85 \cdot 10^{-3} \left[10^{-22}\mathrm{W/m^2/Hz}\right]^{-1}$ with correlation coefficient of $r = 0.991$ (see Fig. 4). If $\alpha = (1 + N \cdot F_{10.7})$, then Eq. 44 may be written in matrix notation as:

$$\underline{\tilde{\epsilon}} = \alpha \underline{\tilde{\varepsilon}} \tag{45}$$

Substituting into Eqs. 40 and 43 gives the final potential forms for the ionospheric and associated induced potentials:

$$V_{sp} = \Re\left\{\underline{\tilde{\varepsilon}}^H \left(D_e^H \underline{S}_e + F^H \underline{S}_i\right)\right\} \tag{46}$$

$$V'_{sp} = \Re\left\{\underline{\tilde{\varepsilon}}^H \left(G^H + F^H\right) \underline{S}_i\right\} \tag{47}$$

where the scalar α has been subsumed by the matrices.

The final issue of concern entails the actual selection of basis functions from the pool of admissible functions already established, i.e. defining the expansion limits for s, p, k, l, n, and m, and any relationships that these imply. This is tantamount to choosing an ensemble of V_{sp} and V'_{sp} across s and p, and then determining the corresponding dimensions of vectors and arrays found in Eqs. 46 and 47. In particular, attention will focus on the selection of the $T^l_{ksp,e}$ functions of Eq. 46, i.e. the vector $\underline{T}_e = D_e^H \underline{S}_e$, since they allow for a clear physical interpretation. Note also that once D_e is determined, then so are F and G.

In order to gain a better understanding of the temporal nature of these functions, consider those of daily variation only on the ionospheric source sphere:

$$T^l_{k0p,e} \mid_{r=a+h} = (a+h) P^l_k(\theta_q) \exp i(l\phi_q + \omega_p p t_m) \tag{48}$$

As t_m increases, the waves propagate along lines of constant θ_q with the wavefronts defined by lines of constant ϕ_q. The local speed of a wave is inversely proportional to the density of lines of constant ϕ_q. The direction a wave travels is determined by the relative signs of l and p. If p is kept arbitrarily positive, then with respect to an Earth-fixed reference frame, modes with $l > 0$ move in the local $-\phi_q$ direction (generally westward), modes with $l = 0$ are standing modes (they oscillate simultaneously at all ϕ_q with frequency $\omega_p p$), and modes with $l < 0$ move in the local $+\phi_q$ direction (generally eastward). Of particular interest is motion with repect to QD magnetic local time longitude, defined as $t_{qlt} = \phi_q + \omega_p t_m$, which at low-mid latitudes moves approximately with the sun. In this reference frame Eq. 48 becomes:

$$T^l_{k0p,e} \mid_{r=a+h} = (a+h) P^l_k(\theta_q) \exp i(l t_{qlt} + \omega_p (p-l) t_m) \tag{49}$$

If p is kept arbitrarily positive and if $l > 0$, then modes with $l > p$ move generally slower than the sun, modes with $l = p$ represent local time modes, i.e. they generally move westward with the same speed as the sun, and modes with $l < p$ move generally faster than the sun. Note that with $p > 0$ and $l < 0$, all modes generally move slower than the sun.

Given the temporal distribution of the magnetic measurements to be analyzed, the first four diurnal harmonics can probably be resolved. This corresponds to a range of $p = 1, \ldots, 4$, which is to say, the 24 hr, 12 hr, 8 hr, and 6 hr periods. The $p = 0$ level will also be included for reasons to be discussed later. Recall that the morphology of the ionospheric field is relatively fixed in magnetic local time. Instead of using all QD longitudinal wavenumbers l (i.e. the whole band-width of $l = -k, \ldots, k$), it is suitable to focus on local time modes ($p = l$) plus slightly faster, respectively slower, travelling modes, limiting l to a tight band-width, L, centered on p (i.e. $l = p - L, \ldots, p + L$). In this study, $L = 1$. To get similar QD latitudinal resolution across diurnal periods, the maximum k should be a constant offset, K, from l (i.e. $k = \max(1, |l|), \ldots, |l| + K$). It is also desirable to have different resolution levels for local ($p = l$) versus non-local ($p \neq l$) time modes, in which case K becomes a function of $p - l$ (i.e. $K = K(p - l)$). In this study, they happen to be the same, with $K(0) = K(\neq 0) = 40$, chosen in hopes of resolving the EEJ. Note that this general selection scheme for p, k, and l has been used in previous studies to produce global field maps from Sq currents (e.g. *Malin and Gupta* [1977]).

Seasonal variation of the ionospheric field is a complicated phenomenon. It is of course, to first order, a function of the angle between the Earth-Sun line and Earth's rotation axis. However, it is also influenced by Earth's magnetic field, whose dipole portion alone wobbles about the rotation axis daily. This, together with commingling of other effects, such as solar radiation flux with its own associated periodicities, makes for a very complex picture indeed. It is

believed, however, that the annual and semi-annual periods will still dominate the seasonal spectrum, and so these are the modes that will be considered in this model. Furthermore, both the eastward and westward counterparts of these modes will be included. All this translates into a range of $s = -2, \ldots, 2$ for the model.

By specifying the s, p, k, and l ranges, the number and type of columns of the D_e, F, and G matrices have been effectively determined. What remains is to determine the number and type of rows of these matrices. Again, focusing on the D_e matrix, one can see from Eq. 19 that this is commensurate with choosing N_{max} and M_{max} such that the regressions converge, which is therefore a function of maximum k and $|l|$. These values are $\max(k) = 45$ and $\max(|l|) = 5$. For these values, and for purposes of this study, an expansion with $N_{max} = 60$ and $M_{max} = 12$ is considered sufficient, i.e. a total of 1368 real regression coefficients per $T^l_{ksp,e}$.

The culmination of the development presented in this section is a set of expressions for the ionospheric and associated induced potentials for the regions $a \leq r \leq a + h$ and $a + h < r$ that hopefully captures the essence of these phenomena in an efficient manner. For clarity, they are written in explicit summation notation as follows:

$$V = \Re\left\{\sum_{s=-2}^{2}\sum_{p=0}^{4}\sum_{l=p-1}^{p+1}\sum_{k=\max(1,|l|)}^{|l|+40}\bar{\varepsilon}^l_{ksp}\cdot \sum_{n=1}^{60}\sum_{m=-\min(n,12)}^{\min(n,12)}\left[(d^{lm}_{kn,e})^* S^m_{nsp,e} + (f^{lm}_{knsp})^* S^m_{nsp,i}\right]\right\} \tag{50}$$

$$V' = \Re\left\{\sum_{s=-2}^{2}\sum_{p=0}^{4}\sum_{l=p-1}^{p+1}\sum_{k=\max(1,|l|)}^{|l|+40}\bar{\varepsilon}^l_{ksp}\cdot \sum_{n=1}^{60}\sum_{m=-\min(n,12)}^{\min(n,12)}\left[(g^{lm}_{kn})^* + (f^{lm}_{knsp})^*\right] S^m_{nsp,i}\right\} \tag{51}$$

where $d^{lm}_{kn,e}$, g^{lm}_{kn}, and f^{lm}_{knsp} are elements of D_e, G, and F-type matrices, respectively. Note the s and p indexing on the F-type elements, which is consistent with Eqs. 38 and 17. The quadruple summation over s, p, l, and k implies 5520 real coefficients, each a free parameter in the ionospheric portion of the CMP3 model. This is about six times less than the number of parameters that would be needed if QD symmetry were not considered.

3.3 Magnetospheric field

The field of the magnetosphere is dominated by features which vary with ring-current intensity, season, and interplanetary magnetic fields (IMF), but also contains features which are relatively fixed in magnetic local time. These time-varying fields also induce currents and resultant secondary fields in the conductive portions of the crust and mantle. Because the major contributing sources of the magnetospheric field are the magnetotail, magnetopause, and ring-current complexes, which lie well outside the sampling region, the field may be represented by the gradient of a potential function. In fact, the form and development of this function will closely parallel that of the ionosphere and associated induced fields for the region $r \leq a + h$. Therefore, one may anticipate a final working form for the magnetospheric potential very similar to Eq. 50, and expedite its development by discussing only the deviations from the ionospheric case.

As just mentioned, a major source of the magnetospheric field is the ring-current, which girdles Earth's equatorial region at a radius of 4-7 Earth radii. The near-Earth spatial structure of the resultant field contribution is dominated by a simple external dipole, i.e. a degree one external field. The temporal variation of this field, however, is not so simple; exhibiting power across broad ranges of the frequency spectrum. The available measurements cannot resolve a high-precision parameterization of such variations. However, being that these variations are important, they should be accounted for in the model. This suggests building the desired variation into the temporal portion of the basis functions, much like the QD symmetry was built into the spatial portion of the basis functions for the ionosphere. *Langel and Estes* [1985a] found a suitable representor of this temporal behavior to be the D_{st} index, which is the horizontal

component, at the equator, of the symmetric portion of the field from the ring-current with respect to Earth's rotation axis. Given that D_{st} is a relative measure of disturbance, the following form is adopted for the source expansion coefficients, ϵ^m_{nsp}, in this portion of the model:

$$\epsilon^m_{1sp} = \mu^m_{1sp} + \mu^m_{1sp,D_{st}} \cdot D_{st}(t) \tag{52}$$

where the D_{st} index is in units of nT and is tabulated at hourly intervals as a function of universal time. Note that this relationship is adopted only for the dipole terms ($n = 1$), and that the temporal variability of $D_{st}(t)$ is modulated by both seasonal and diurnal oscillations (by virtue of the s and p indexing), the latter helping to describe local time asymmetries.

Induced fields may be treated just as they were in the ionospheric field development section. The major difference is the inclusion of basis functions which are now dependent upon the seasonally and diurnally modulated $D_{st}(t)$ index. Hence, for magnetospheric induction, Eq. 17 becomes:

$$q^{mm}_{nn}(f) = \begin{cases} 0 & \text{for } p = 0,\ s = 0, \text{ and no } D_{st}(t); \\ q^{mm}_{nn}(0) & \text{for } p = 0,\ s = 0, \text{ and } D_{st}(t)\ ; \\ q^{mm}_{nn}(0) & \text{for } p = 0 \text{ and } s > 0\ ; \\ q^{mm}_{nn}(p) & \text{for } p > 0\ . \end{cases} \tag{53}$$

Magnetospheric contributions that vary only with $D_{st}(t)$ are assumed to contain mostly signals with a period of a few days, at least during magnetic quiet days, hence, the use of a $q^{mm}_{nn}(0)$ based upon $\delta = 1000$ km.

At the source region for the magnetospheric current systems the Earth's magnetic field is more dipole-like compared to ionospheric current systems, and therefore, it is not necessary (though possible) to use QD coordinates for the characterization of magnetospheric sources. Thus, for this portion of the model:

$$D_e = I \tag{54}$$

$$F = Q \tag{55}$$

The final item of business is the selection of basis functions as prescribed by the ranges and relationships of s, p, k, and l. It follows from Eqs. 54 and 55, and the fact that Q is diagonal for a given s and p, that the n and m indices need not be explicitly specified. The relationship between p, k, and l is as for the ionosphere in that l resides in a narrow band-width about p, as specified by L, and maximum k is at a constant offset, K, from l to preserve latitudinal resolution levels across p. Again, the K is a function of local versus non-local time (i.e. $K = K(p - l)$).

The expansion limits are also somewhat similar to those of the ionosphere, with a seasonal variation of $s = -2, \ldots, 2$, a diurnal variation of $p = 0, \ldots, 5$, and $L = 1$. The major difference is found in the latitudinal resolution level, which is much less for the magnetosphere and different for local and non-local time modes: $K(0) = 5$ and $K(\neq 0) = 3$. It is expected that a significant number of expansion coefficients will be negligible at these truncation levels. In an investigation of geomagnetic daily variations as predicted by the Tsyganenko model of the magnetosphere (which are derived from data collected at several Earth radii), *Olsen* [1996] concluded that the only non-negligible coefficients are found within the expansion limits of $p = 0, \ldots, 2$, $L = 1$, and $K(0) = 3$ and $K(\neq 0) = 1$. However, since this is the first time ionospheric and magnetospheric parameterizations of this type have been coestimated, these liberal limits allow for the unexpected.

As a result of the previous development, an expression for the magnetospheric and associated induced potentials for observatory as well as satellite data is now given in explicit summation notation with D_{st} dependent terms broken out:

$$\begin{aligned} V = \Re \Bigg\{ & \sum_{s=-2}^{2} \sum_{p=0}^{5} \sum_{l=p-1}^{p+1} \sum_{k=\max(1,|l|)}^{|l|+K(p-l)} \mu^l_{ksp} \left[S^l_{ksp,e} + (q^{ll}_{kksp})^* S^l_{ksp,i} \right] + \\ & \sum_{s=-2}^{2} \sum_{p=0}^{5} \sum_{l=p-1}^{p+1} \sum_{k=\max(1,|l|)}^{1} \mu^l_{ksp,D_{st}} \cdot D_{st} \left[S^l_{ksp,e} + (q^{ll}_{kksp,D_{st}})^* S^l_{ksp,i} \right] \Bigg\} \end{aligned} \tag{56}$$

Note the s, p, and D_{st} indexing on the Q elements, which is consistent with Eq. 53. The summation over s, p, l, and k entails 800 real coefficients, which is the number of free parameters in the magnetospheric portion of the CMP3 model.

3.4 Fields from ionospheric coupling currents

When establishing the form of the basis functions used to represent ionospheric fields, it was assumed that the source currents flowed in a region that was entirely below the Magsat and POGO satellite sampling shells. In addition, a relationship was assumed between the external and internal fields from these currents based upon the concept of an equivalent sheet current flowing on a sphere at $r = a + 110$ km. If displacement currents are neglected, then the source currents are solenoidal, and these assumptions may be used for current loops or circuits which do not pierce the sampling shell, which is true for the E-region. However, in reality, these ionospheric currents are coupled to the magnetospheric and ionospheric E-region currents at the geomagnetic conjugate point through "coupling currents" which flow along the field lines of the Earth's magnetic field. This means, for instance, that the Magsat sampling region between $a + 350$ km and $a + 550$ km will be penetrated by F-region current whose associated magnetic field, $\delta\underline{B}$, will not be curl-free, and hence, will not be expressible as the gradient of a potential. It should also be noted that in general only vector, as opposed to scalar, samples can detect these fields, since $\delta\underline{B}$ is almost always perpendicular to the main field. Hence, only measurements from the Magsat satellite will be considered here.

Olsen [1997a], partially following *Backus* [1986], employs a theorem which provides for a decomposition of any solenoidal vector field into unique toroidal and poloidal parts on a sphere. Applying this to $\delta\underline{B}$ in dipole spherical coordinates gives its toroidal, $\delta\underline{B}_t$, and poloidal, $\delta\underline{B}_p$, parts in terms of derivatives of toroidal, Φ, and poloidal, Ψ, scalar functions:

$$\begin{aligned}
\delta\underline{B} &= \delta\underline{B}_t + \delta\underline{B}_p && (57)\\
&= \nabla \times \underline{r}\Phi + \nabla \times \nabla \times \underline{r}\Psi && (58)\\
&= \begin{pmatrix} 0 \\ \frac{1}{\sin\theta_d}\frac{\partial}{\partial\phi_d}\Phi \\ -\frac{\partial}{\partial\theta_d}\Phi \end{pmatrix} + \begin{pmatrix} -\nabla_s^2\,(r\Psi) \\ \frac{1}{r}\frac{\partial}{\partial\theta_d}\,(r\Psi)' \\ \frac{1}{r\sin\theta_d}\frac{\partial}{\partial\phi_d}\,(r\Psi)' \end{pmatrix} && (59)
\end{aligned}$$

with the prime denoting the $\frac{\partial}{\partial r}$ operator, and:

$$\nabla_s^2 = \frac{1}{r^2\sin\theta_d}\frac{\partial}{\partial\theta_d}\left(\sin\theta_d\frac{\partial}{\partial\theta_d}\right) + \frac{1}{r^2\sin^2\theta_d}\frac{\partial^2}{\partial\phi_d^2} \qquad (60)$$

as the horizontal part of the Laplacian operator. The associated current density, $\underline{J}$, is then given by:

$$\begin{aligned}
\mu_0\underline{J} &= \nabla \times \delta\underline{B} && (61)\\
&= \mu_0\left(\underline{J}_t + \underline{J}_p\right) && (62)\\
&= -\nabla \times \underline{r}\nabla^2\Psi + \nabla \times \nabla \times \underline{r}\Phi && (63)\\
&= \begin{pmatrix} 0 \\ -\frac{1}{\sin\theta_d}\frac{\partial}{\partial\phi_d}\nabla^2\Psi \\ \frac{\partial}{\partial\theta_d}\nabla^2\Psi \end{pmatrix} + \begin{pmatrix} -\nabla_s^2\,(r\Phi) \\ \frac{1}{r}\frac{\partial}{\partial\theta_d}\,(r\Phi)' \\ \frac{1}{r\sin\theta_d}\frac{\partial}{\partial\phi_d}\,(r\Phi)' \end{pmatrix} && (64)
\end{aligned}$$

Backus [1986] showed that for a shell whose thickness is small in comparison to its mean radius, $\delta\underline{B}_p$ goes to zero. This will be the case for the Magsat sampling shell, and so this approximation is adopted here:

$$\delta\underline{B} = \nabla \times \underline{r}\Phi \qquad (65)$$

with associated current:

$$\mu_0\underline{J} = \nabla \times \nabla \times \underline{r}\Phi \qquad (66)$$

In order for $\delta\underline{B}$ to be unique, the mean value of Φ over the sphere must be zero, i.e. $\int_\Omega \Phi \; d\Omega = 0$ with $d\Omega = \sin\theta_d d\theta_d d\phi_d$. Expanding Φ in surface spherical harmonics:

$$\Phi = \Re\left\{\sum_{n,m} \phi_n^m(r) P_n^m(\theta_d) \exp im\phi_d\right\} \tag{67}$$

requires expansion coefficients with $n = 0$ to vanish.

The radial dependence of the Φ expansion coefficients, $\phi_n^m(r)$, must still be specified. *Olsen* [1997a] considered a $\frac{1}{r}$ dependence on all coefficients, making $(r\Phi)' = 0$, and leading to a purely radial poloidal current density, J_r, in Eq. 64. When applying this to satellite data at a height above 350 km, as in this study, the assumption of radial currents is reasonable for the field-aligned currents in polar latitudes as well as for a very narrow band at the dip equator where the meridional current system flows in the radial direction. However, the assumption fails at middle latitudes. Nevertheless, this assumption is also adopted here, which leads to:

$$\Phi = \Re\left\{\sum_{n,m} \left(\frac{a}{r}\right) \phi_n^m P_n^m(\theta_d) \exp im\phi_d\right\} \tag{68}$$

or in matrix notation:

$$\Phi = \Re\left\{\underline{\phi}^H \underline{S}_j\right\} \tag{69}$$

where $\underline{\phi}$ is the vector of $(\phi_n^m)^*$ and $\underline{S}_j$ is the vector with elements given by:

$$S_{n,j}^m = \left(\frac{a}{r}\right) P_n^m(\theta_d) \exp im\phi_d \tag{70}$$

The toroidal scalar function Φ may also be thought of as the stream function for $\delta\underline{B}$, since its contours trace the $\delta\underline{B}$ field lines.

As in the case of the E-region discussed earlier, the F-region conductivity structure is also highly aligned with the magnetic field, which suggests the use of QD symmetric basis functions in order to reduce the number of free parameters needed. For example, the meridional coupling currents of the EEJ show a strong radial upwelling along $\theta_q = 90°$. From Eqs. 64, 68, and the associated Legendre differential equation, the radial component of $\underline{J}$ on the F-region source sphere ($r = a + h$ with $h = 450$ km) may be written as:

$$J_r = \Re\left\{\frac{1}{\mu_0(a+h)} \sum_{n,m} n(n+1) \left(\frac{a}{a+h}\right) \phi_n^m P_n^m(\theta_d) \exp im\phi_d\right\} \tag{71}$$

Following Eqs. 20 and 21, this suggests a stream function basis with the desired QD symmetry given by:

$$T_{k,j}^l = \sum_{n,m} (d_{kn}^{lm})^* \left(\frac{a+h}{a}\right) S_{n,j}^m \tag{72}$$

Clearly then:

$$T_{k,j}^l \mid_{r=a+h} = P_k^l(\theta_q) \exp il\phi_q \tag{73}$$

The d_{kn}^{lm} regression coefficients would be slightly different from those introduced earlier since these now reflect the QD symmetry at $r = a + 450$ km. Expressions analogous to Eq. 69 may now be written in the new basis:

$$\Phi = \Re\left\{\tilde{\underline{\phi}}^H \underline{T}_j\right\} \tag{74}$$

$$= \Re\left\{\tilde{\underline{\phi}}^H D^H \underline{S}_j \left(\frac{a+h}{a}\right)\right\} \tag{75}$$

$$= \Re\left\{\tilde{\underline{\phi}}^H D_j^H \underline{S}_j\right\} \tag{76}$$

where $\tilde{\underline{\phi}}$ is the vector of $(\tilde{\phi}_k^l)^*$, the reduced parameter set, $\underline{T}_j$ is the vector of $T_{k,j}^l$, and D is the matrix of d_{kn}^{lm} regression coefficients. As in the case of the E-region, imposing the QD symmetry at $r = a + h$ imposes a linear constraint on the original expansion coefficients:

$$\underline{\phi} = D_j \tilde{\underline{\phi}} \tag{77}$$

The temporal variation of the magnetic fields from ionospheric coupling currents will be much the same as for fields from the ionospheric E-region in that there will be strong local time modes which are modulated by both interactions with the main field and by significant seasonal effects. This suggests multiplying the Φ basis functions $T^l_{k,j}$ by complex exponentials of the form: $\exp i(\omega_s st + \omega_p pt_m)$, and then assembling them in a manner similiar to Eqs. 50 and 51. Although this is a valid approach in general, one must remember that it is only the Magsat data which are sensitive to these parameters, and that the scope of these data with respect to certain aspects of time coverage is severely limited. To begin with, the mission duration over which usable data was aquired was from November, 1979 to April, 1980, which is but six months. If one is interested in both annual and semi-annual seasonal periods, then it is unlikely that both a phase and amplitude can be resolved for the former. Assuming, however, that the maximum annual amplitudes occur at the solstices (or t values of roughly 0 and 6 mo), then the phase may be fixed, leaving only the amplitude to be resolved. If it is also assumed that maximum semi-annual amplitudes occur at the solstices and equinoxes (or t values of roughly 0, 3, 6, and 9 mo), then its phase may also be fixed. These conditions translate into a set of admissible functions of the form:

$$T^l_{ks,j} = T^l_{k,j} \cos(\omega_s st) \tag{78}$$

$$= \sum_{n,m} (d^{lm}_{kn,j})^* S^m_{n,j} \cos(\omega_s st) \tag{79}$$

$$= \sum_{n,m} (d^{lm}_{kn,j})^* S^m_{ns,j} \tag{80}$$

where $d^{lm}_{kn,j}$ are elements of the D_j matrix. Clearly, the annual and semi-annual functions of interest correspond to $s = 1$ and $s = 2$, respectively.

A further limitation of the Magsat data is that it sampled only two local times, dawn and dusk (or t_m values of roughly 6 and 18 hr). The Nyquist frequency for this sampling rate would be the diurnal ($p = 1$) frequency; all higher frequency harmonics ($p > 1$) would be aliased. Therefore, a continuous local time analysis is prohibited at the periods of interest. Consider, however, that over a period of several days to weeks a high density distribution of both Magsat dawn and dusk passes may be realized over all longitudes. This suggests that one model the behavior of particular local times as a function of geographic position, and of course season. This is formally equivalent to including a factor of $\exp i\omega_p pt_m$ in Eq. 78 with t_m fixed at the local time of interest. Since this is a complex constant throughout the analysis, it is simply subsumed by the associated expansion coefficient, leaving Eq. 78 essentially intact.

What remains is to select the basis functions $T^l_{ks,j}$ by specifying the limits of the s, k, l, n, and m indices. As previously discussed, there will be separate dawn and dusk contributions from the coupling currents considered in this model, each with a seasonal wavenumber range of $s = 1, 2$. The k and l ranges for these contributions are less complicated to specify than for the ionospheric potential field, since they reflect the spatial resolution level in an Earth-fixed mode versus a moving mode. Consequently, the latitudinal and longitudinal resolution levels are independent of one another. It is anticipated that most features of interest will lie in relatively thin, elongated QD latitude bands, which implies a high K_{max} and a low L_{max}. If the field from the EEJ coupling currents has a half-wavelength of about 5° at $\theta_q = 90°$, then $K_{max} = 40$ should suffice. For this study, $L_{max} = 4$. Finally, given these values of K_{max} and L_{max}, an expansion with $N_{max} = 60$ and $M_{max} = 12$ is considered sufficient, i.e. a total of 1368 real regression coefficients per $T^l_{ks,j}$.

The working form of the stream function for the toroidal field due to ionospheric F-region coupling currents in the Magsat sampling region may now be expressed in explicit summation notation as follows:

$$\Phi = \Re\left\{ \sum_{s=0}^{2} \sum_{k=1}^{40} \sum_{l=0}^{\min(k,4)} \tilde{\phi}^l_{ks} \sum_{n=1}^{60} \sum_{m=-\min(n,12)}^{\min(n,12)} (d^{lm}_{kn,j})^* S^m_{ns,j} \right\} \tag{81}$$

The triple summation over s, k, and l entails 1044 real coefficients, and since there is a distinct Φ for both dawn and dusk, then the total number of free parameters in this portion of the CMP3 model is 2088. This is about four times less than the number of parameters that would be needed if QD symmetry were not considered.

3.5 Observed fields

At present, expressions have been developed for the potential functions of the magnetic fields from the core and lithosphere, ionospheric E-region, and magnetosphere; for the toroidal field stream function associated with the ionospheric F-region coupling currents; and for observatory vector biases. In this section, the relationship of such quantities with what is actually observed by Magsat, POGO, and the observatories will be addressed. In the case of the latter, for instance, it is not enough to simply superimpose the negative gradients of all pertinent potential functions, add the bias, and call this the predicted magnetic field vector. There are subtle issues, like coordinate basis compatibility, that cannot be ignored.

The first step is to identify the various coordinate bases in which vector measurements are made and how they relate to those implied by the model. The Magsat vector data have been transformed to a local spherical basis, while the observatory vector data are reported in a local ellipsoidal basis (i.e. geodetic coordinates). However, the potential function for the core and lithospheric fields is cast in geographic spherical polar coordinates, while those of the ionospheric E-region and magnetosphere are cast in dipole spherical polar coordinates, as is the toroidal field stream function. Therefore, one needs to apply the appropriate rotations in order for the predicted field vector to be compatible with the measured.

The second step is to determine which parts of the model apply to which measurement sets. The Magsat vector data will sense the fields from the core and lithosphere, the ionospheric E-region (per Eq. 51), the magnetosphere, and the field associated with ionospheric F-region coupling currents. Both Magsat and POGO scalar data will sense all but the last contribution. The observatory hourly means data will also sense the fields from the core and lithosphere, the ionospheric E-region (per Eq. 50), and the magnetosphere. In addition, they will have their own set of vector biases estimated, which means that they only sense the time varying part (secular variation) of the core field. Likewise, the observatory annual means data will certainly sense the secular variation. However, because they represent field averages of up to a year, they will be treated as if their ionospheric E-region and magnetospheric contributions have been filtered out. This would probably be closer to the truth if the annual means were averaged over quiet times only. However, given that they are not, this treatment would be amenable to substantial improvement if it were not for the fact that their sole purpose is to determine the main field secular variation, which they do satisfactorily. Because the annual means have a different baseline than the hourly means, they too have their own set of vector biases estimated, and their influence on the hourly means is thus reduced.

The result of this discussion is a set of expressions for predicting the magnetic field as seen by Magsat, POGO, observatory hourly means (OHM), and observatory annual means (OAM):

$$\underline{B}_{Magsat} = -\nabla_g V_{cl} - R_{gd}\left[\nabla_d \left(V'_{ion} + V_{mag}\right) - \nabla \times \underline{r}\Phi\right] \tag{82}$$

$$|\underline{B}_{Magsat}| = \left|-\nabla_g V_{cl} - R_{gd}\nabla_d \left(V'_{ion} + V_{mag}\right)\right| \tag{83}$$

$$|\underline{B}_{POGO}| = \left|-\nabla_g V_{cl} - R_{gd}\nabla_d \left(V'_{ion} + V_{mag}\right)\right| \tag{84}$$

$$\underline{B}_{OHM} = -R_{es}\left[\nabla_g V_{cl} + R_{gd}\nabla_d \left(V_{ion} + V_{mag}\right)\right] + \underline{B}_{bias,OHM} \tag{85}$$

$$\underline{B}_{OAM} = -R_{es}\nabla_g V_{cl} + \underline{B}_{bias,OAM} \tag{86}$$

where V_{cl}, V_{ion}, V'_{ion}, and V_{mag} are the potential functions for the fields of the core and lithosphere, the ionospheric E-region for $a \leq r \leq a + h$ and $a + h < r$, and the magnetosphere, respectively. The ∇_g and ∇_d are the gradient operators in geographic and dipole spherical polar coordinates, respectively. The R_{gd} is a rotation matrix from the local dipole spherical to the local geographic spherical basis. It is a function of the colatitude and longitude of the observation point in both geographic and dipole coordinates, and of the geographic colatitude and longitude of the dipole moment of the main field (i.e. θ_m and ϕ_m). In this study, the dipole moment is provided by the GSFC(12/83) main field model of *Langel and Estes* [1985b], whose $\theta_m = 11.2°$ and $\phi_m = 289.3°$. The R_{es} is a rotation matrix from the local geographic spherical to the local geographic ellipsoidal basis given by *Langel* [1987]:

$$\begin{pmatrix} B_x \\ B_y \\ B_z \end{pmatrix} = \begin{pmatrix} -\cos\eta & 0 & -\sin\eta \\ 0 & 1 & 0 \\ \sin\eta & 0 & -\cos\eta \end{pmatrix} \begin{pmatrix} B_\theta \\ B_\phi \\ B_r \end{pmatrix} \tag{87}$$

where $\eta = \theta - \theta_g$ and θ_g is the geodetic colatitude determined using a reference ellipsoid for the Earth. For this study,

the IAU ellipsoid (International Astronomical Union, 1966) is used; it has an equatorial radius of 6378.160 km and flattening of $\frac{1}{298.25}$ [*Barton*, 1997].

4 Estimation of model parameters

Since the main thrust of this investigation involves the determination of the proposed field parameterizations from the satellite and observatory measurements, one must solve an inverse problem. Furthermore, this problem does not usually possess a unique solution, and the scalar data are non-linear functions of the model parameters. This suggests the use of an iterative least-squares (LS) estimator for determining the model.

4.1 Iterative Gauss least-squares estimator

The particular iterative LS estimator favored in this study is the Gauss method, due to its superior convergence properties over the steepest descent method and its simplicity over the full Newton method [*Sorenson*, 1980]. Consider a constrained model of the form:

$$\begin{cases} \underline{d} &= \underline{a}(\underline{x}) &+ \underline{\nu} \\ \underline{x}_{a_1} &= \underline{x} &+ \underline{\xi}_1 \\ &\vdots & \\ \underline{x}_{a_k} &= \underline{x} &+ \underline{\xi}_k \end{cases} \tag{88}$$

where $\underline{d}$ is the measurement vector, $\underline{a}(\underline{x})$ is a non-linear, continuously differentiable vector function of the model parameter vector $\underline{x}$, $\underline{\nu}$ is the noise vector of zero mean and covariance $C_\nu = \hat{\sigma}^2 W^{-1}$, $\underline{x}_{a_i}$ is the *a priori* preferred model parameter vector from the i-th constraint, $\underline{\xi}_i$ is the error vector of zero mean and covariance $C_{\xi_i} = (\hat{\sigma}^2/\lambda_i)\Lambda_i^{-1}$ for the i-th constraint, and $\hat{\sigma}^2$ is the dimensionless data misfit. The corresponding LS objective function is given by:

$$\mathcal{L}(\underline{x}) = \underline{\nu}^T W \underline{\nu} + \sum_{i=1}^{k} \lambda_i \underline{\xi}_i^T \Lambda_i \underline{\xi}_i \tag{89}$$

$$= \mathcal{L}_r(\underline{x}) + \sum_{i=1}^{k} \lambda_i Q_i(\underline{x}) \tag{90}$$

$$= \mathcal{L}_r(\underline{x}) + \sum_{i=1}^{k} \mathcal{L}_{e_i}(\underline{x}) \tag{91}$$

The first term, $\mathcal{L}_r(\underline{x})$, is the weighted residual variance, and the following terms, $\mathcal{L}_{e_i}(\underline{x})$, are the weighted error variances with respect to the preferred models. The λ_i are damping parameters whose units are reciprocal to those of the corresponding norms, $Q_i(\underline{x})$. It is assumed that both W^{-1} and the Λ_i^{-1} are known, the former being based upon data noise and model inadequacies and the latter typically based upon some physically meaningful quantity to be minimized.

Expanding $\mathcal{L}(\underline{x})$ in a second-order Taylor series about the n-th iterate point $\underline{x}_n$ and minimizing, under the assumption that $\underline{x}_n$ lies in a small-curvature, small-residual regime, yields the iterative Gauss LS estimator [*Tarantola and Valette*, 1982]:

$$\begin{cases} \underline{x}_{n+1} &= \underline{x}_n + \delta\underline{x}_n \\ \delta\underline{x}_n &= \left[A_n^T W A_n + \sum_{i=1}^{k} \lambda_i \Lambda_i\right]^{-1} \left[A_n^T W \left(\underline{d} - \underline{a}(\underline{x}_n)\right) + \sum_{i=1}^{k} \lambda_i \Lambda_i \left(\underline{x}_{a_i} - \underline{x}_n\right)\right] \end{cases} \tag{92}$$

where:

$$A_n = \frac{\partial \underline{a}(\underline{x})}{\partial \underline{x}} \Big|_{\underline{x}=\underline{x}_n} \tag{93}$$

4.2 Error covariance and misfit of model

Consider now the covariance of the errors in the final iterate, $\underline{x}_{n+1}$, with the LS estimate of $\underline{x}$, denoted $\tilde{\underline{x}}$. If $\underline{x}_n$ is sufficiently "close" to $\underline{x}$ such that the second-order terms in a Taylor expansion of $\underline{a}(\underline{x})$ about $\underline{x}_n$ may be neglected, and if $\underline{\nu}$ and the $\underline{\xi}_i$ are independent, then the error covariance matrix of the model, C_x, is given by:

$$C_x = \hat{\sigma}^2 \left(A_n^T W A_n + \sum_{i=1}^{k} \lambda_i \Lambda_i \right)^{-1} \tag{94}$$

The data misfit, $\hat{\sigma}^2$, is an unknown scalar factor of the observation error covariance matrix of the augmented system in Eq. 88. An estimate, s^2, of $\hat{\sigma}^2$ may be realized by considering the expected value of the *a posteriori* $\mathcal{L}_r(\underline{x})$ function:

$$E\left[\mathcal{L}_r(\tilde{\underline{x}})\right] = \hat{\sigma}^2 \left(N - tr\left[R\right]\right) \tag{95}$$

with:

$$R = \left(A_n^T W A_n + \sum_{i=1}^{k} \lambda_i \Lambda_i \right)^{-1} \left(A_n^T W A_n \right) \tag{96}$$

where $E\left[\cdot\right]$ and $tr\left[\cdot\right]$ are the expectation and trace operators, respectively, N is the number of observations, and R is the resolution matrix, which acts as a filter through which the true model state is seen, and whose trace gives the number of model parameters resolved by the data [*Langel*, 1987]. Hence, an unbiased estimate of $\hat{\sigma}^2$ is given by [*Toutenburg*, 1982]:

$$s^2 = \frac{\mathcal{L}_r(\tilde{\underline{x}})}{N - tr\left[R\right]} \tag{97}$$

Thus, s^2 is a measure of how well the model fits the weighted data per degree of freedom (DOF), and should be approximately unity if the weighting is correct [*Bloxham et al.*, 1989]. Of course, multiplying W^{-1} and the Λ_i^{-1} by s^2 will not change $\tilde{\underline{x}}$ in Eq. 92, but will make subsequent estimates of the data misfit equal to unity. With s^2 substituted into Eq. 94, one obtains an unbiased estimate of C_x, denoted $\tilde{C}_x$, which is sometimes called the "calibrated" error covariance since the observations are now fit as well as $\tilde{C}_\nu = s^2 W^{-1}$ indicates they can be.

Two additional classes of misfits also suggest themselves: first, data subset misfits, $s_{d_i}^2$, which measure how well the model fits the i-th subset of weighted data per DOF in that subset; and secondly, prior misfits, $s_{a_i}^2$, which measure the departure of the model from the i-th *a priori* preferred model per DOF in that norm. They are defined in a manner similar to s^2:

$$s_{d_i}^2 = \frac{\mathcal{L}_{r_i}(\tilde{\underline{x}})}{N_i - tr\left[R_{d_i}\right]} \tag{98}$$

$$s_{a_i}^2 = \frac{\mathcal{L}_{e_i}(\tilde{\underline{x}})}{M_i - tr\left[R_{a_i}\right]} \tag{99}$$

with:

$$R_{d_i} = \left(A_n^T W A_n + \sum_{i=1}^{k} \lambda_i \Lambda_i \right)^{-1} \left(A_{n_i}^T W A_{n_i} \right) \tag{100}$$

$$R_{a_i} = \left(A_n^T W A_n + \sum_{i=1}^{k} \lambda_i \Lambda_i \right)^{-1} \left(\lambda_i \Lambda_i \right) \tag{101}$$

where N_i is the number of observations in the i-th data subset, M_i is the length of $\underline{x}_{a_i}$, and A_{n_i} is the submatrix of A_n associated with the i-th data subset. It is assumed that the subset noise vectors, $\underline{\nu}_i$, are mutually independent, i.e. the C_ν matrix is block-diagonal along the subset boundaries. Hence, associated with each block is a scale factor $s_{d_i}^2$. Though the values of each $s_{d_i}^2$ are not expected to be unity when adjusting s^2 only, a "fine-scale calibration" method could adjust them, and consequently s^2, to unity. This would provide a way in which independent data could

be optimally combined in estimation procedures. Furthermore, if the information introduced by the i-th constraint equation is truly stochastic in nature, then s^2 should be modified to reflect this:

$$s^2 = \frac{\mathcal{L}_r(\underline{\tilde{x}}) + \mathcal{L}_{e_i}(\underline{\tilde{x}})}{N + M_i - tr\,[R + R_{a_i}]} \tag{102}$$

In view of the "fine-scale calibration" paradigm, $s^2_{a_i}$ would also be adjusted to unity, and thus, the method allows for the damping parameter λ_i to be objectively determined.

4.3 Regularization and *a priori* information

The Gauss estimator provides a framework, via the $\mathcal{L}_{e_i}(\underline{x})$ terms in Eq. 91, by which additional metrics or norms may be introduced into the cost function. These norms are of basically two natures: first, they allow for a unique solution by choosing the smoothest from the admissible set with respect to the given measure, i.e. they regularize the solution; and secondly, they allow for soft, typically data independent, physical bounds to be placed upon the model parameter space, i.e. they introduce additional theory into the model. Though their forms are similar, they reflect very different philosophies, and there is occasion to employ both in this study.

The first norm to be discussed is motivated by the theory that the nightside ionospheric E-region conductivity is greatly diminished due to the lack of solar EUV ionizing radiation, at least at the mid and low latitudes. This means that the equivalent current density, $\underline{J}_{eq}$, is minimal in these areas. To quantify this, apply Eqs. 33 and 50 and the Ampère circuital law to ionospheric $\underline{B}$ in an infinitesimal plane that is perpendicular to and centered on the sheet where currents flow ($r = a + h$) such that [*Langel et al.*, 1993]:

$$\underline{J}_{eq} = \frac{1}{\mu_0}\Delta\underline{B}_h \tag{103}$$

$$= -\hat{\underline{r}} \times \nabla\Psi \tag{104}$$

where $\Delta\underline{B}_h$ is the jump discontinuity in the horizontal component of $\underline{B}$, and the current function, Ψ [*Chapman and Bartels*, 1940], is given by:

$$\Psi = \Re\left\{ -\frac{1}{\mu_0} \sum_{s=-2}^{2} \sum_{p=0}^{4} \sum_{l=p-1}^{p+1} \sum_{k=\max(1,|l|)}^{|l|+40} \tilde{\varepsilon}^l_{ksp} \cdot \sum_{n=1}^{60} \sum_{m=-\min(n,12)}^{\min(n,12)} (d^{lm}_{kn,e})^* \left(\frac{2n+1}{n+1}\right) S^m_{nsp,e}\,|_{r=a+h} \right\} \tag{105}$$

It can also be seen from Eq. 104 that Ψ is the stream function of $\underline{J}_{eq}$.

The theory takes the form of a quadratic norm, $\mathcal{Q}_{|\underline{J}_{eq}|}$, which measures the mean-square magnitude of $\underline{J}_{eq}$ on a spherical sector or patch, Ω_s, fixed in dipole magnetic local time longitude, defined as $t_{mlt} = \phi_d + \omega_p t_m$, over time. It has been chosen to span a patch of low conductivity of about 8 hours width centered on local 1:00 am as opposed to local midnight (i.e. $t_{mlt} = 21 \cdot \frac{\pi}{12}, \ldots, 5 \cdot \frac{\pi}{12}$), which leads to:

$$\mathcal{Q}_{|\underline{J}_{eq}|} = \int_0^T \int_{\Omega_s} \left|\underline{J}_{eq}(\theta_d, t_{mlt}, t_m)\right|^2 d\Omega_s d\tau_m \Big/ \int_0^T \int_{\Omega_s} d\Omega_s d\tau_m \tag{106}$$

$$= \frac{3}{4\pi T} \int_0^T \int_{21\cdot\frac{\pi}{12}}^{5\cdot\frac{\pi}{12}} \int_0^{\pi} \left|\underline{J}_{eq}(\theta_d, t_{mlt}, t_m)\right|^2 \sin\theta_d d\theta_d d\tau_{mlt} d\tau_m \tag{107}$$

or in matrix notation:

$$\mathcal{Q}_{|\underline{J}_{eq}|} = \underline{\tilde{e}}^T \Lambda_{|\underline{J}_{eq}|} \underline{\tilde{e}} \tag{108}$$

with:

$$\underline{\tilde{e}} = \begin{pmatrix} \Re\{\underline{\tilde{\varepsilon}}\} \\ \Im\{\underline{\tilde{\varepsilon}}\} \end{pmatrix} \tag{109}$$

where $\Lambda_{|\underline{J}_{eq}|}$ is a real, positive-definite, symmetric matrix representation of the norm. Note that this matrix is not diagonal because the t_{mlt} integration is only over $\frac{2\pi}{3}$ radians and because the D_e matrix is involved. Furthermore, the t_m integration is facilitated by three assumptions: first, the time variation of the $F_{10.7}$ index is neglected, rendering $\underline{J}_{eq}$ periodic over one year such that $T = 1$ yr; secondly, universal time t in Eq. 13 is treated as magnetic universal time t_m, which is then used for time integration; and thirdly, $\omega_p = 365\omega_s$ in Eq. 13. Although the second assumption is best at low and mid latitudes, and the third is best during non-leap years, it is expected that these will make little difference in the analysis, especially since $\mathcal{Q}_{|\underline{J}_{eq}|}$ is a soft bound.

The $\mathcal{Q}_{|\underline{J}_{eq}|}$ norm works in conjunction with the $p = 0$ terms of Eq. 50 to establish a nightside baseline such that $\underline{J}_{eq}$ is minimized at those hours. This baseline is a global function, able to adjust to geographic shifts, which is static on diurnal time scales, but varies with season. Because there is difficulty in separating this functional behavior from that of main field secular variation at satellite altitude, the strength of the norm is adjusted via the associated $\lambda_{|\underline{J}_{eq}|}$ such that all $p = 0$ terms are determined by the norm. It is also for this reason that the influence of the norm cannot be greatly reduced in the polar regions (e.g. via some dipole colatitude weighting function) where $\underline{J}_{eq}$ is thought to flow at all magnetic local times.

Recall that in order to resolve the EEJ along the dip equator, QD degrees of up to $k = 45$ are used. Since the $T^l_{ksp,e}$ functions are global, it is expected that spurious oscillations will be exhibited in the $\underline{J}_{eq}$ morphology. Although the preferred model state for the $\mathcal{Q}_{|\underline{J}_{eq}|}$ norm is $\underline{\tilde{e}} = \underline{0}$, making it technically a smoothing norm, its influence is limited in proximity to magnetic local times of 21 hr to 5 hr. Hence, an additional norm is sought to minimize this roughness on the dayside, which suggests minimizing the mean-square magnitude of some function of the second-order horizontal derivatives of $\underline{J}_{eq}$. A natural choice is the surface Laplacian of $\underline{J}_{eq}$. However, this norm should not interfere with the $p = 0$ baseline established for $\underline{J}_{eq}$ by the $\mathcal{Q}_{|\underline{J}_{eq}|}$ norm, and so it is restricted to current densities in the $p > 0$ regime, denoted as $\underline{J}_{eq,p>0}$. Consequently, the norm may be applied at all magnetic local times. Furthermore, it must not interfere with legitimate EEJ variations near the dip equator nor with flow in the auroral regions. This may be accomplished by introducing a non-negative weighting or influence function in dipole colatitude which is smaller in the equatorial and polar regions and larger at mid-latitudes. The function used in this study is $\sin^8 2\theta_d$. Although a more rigorous approach would use QD colatitude, it is much more complicated and is left for future work.

Formally, this norm, denoted as $\mathcal{Q}_{|\nabla^2_s \underline{J}_{eq,p>0}|}$, is a quadratic function of $\underline{\tilde{e}}_{p>0}$ which measures the weighted mean-square magnitude of the surface Laplacian of $\underline{J}_{eq,p>0}$ on a sphere, Ω, over time:

$$\mathcal{Q}_{|\nabla^2_s \underline{J}_{eq,p>0}|} = \int_0^T \int_\Omega \left|\nabla^2_s \underline{J}_{eq,p>0}(\theta_d, \phi_d, t_m)\right|^2 \sin^8 2\theta_d d\Omega d\tau_m \Bigg/ \int_0^T \int_\Omega \sin^8 2\theta_d d\Omega d\tau_m \tag{110}$$

$$= \int_0^T \int_0^{2\pi} \int_0^{\pi} \left|\nabla^2_s \underline{J}_{eq,p>0}(\theta_d, \phi_d, t_m)\right|^2 \sin^8 2\theta_d \sin\theta_d d\theta_d d\phi_d d\tau_m \Bigg/ \left(\frac{131072}{109395}\right)\pi T \tag{111}$$

or in matrix notation:

$$\mathcal{Q}_{|\nabla^2_s \underline{J}_{eq,p>0}|} = \underline{\tilde{e}}^T_{p>0} \Lambda_{|\nabla^2_s \underline{J}_{eq,p>0}|} \underline{\tilde{e}}_{p>0} \tag{112}$$

where $\Lambda_{|\nabla^2_s \underline{J}_{eq,p>0}|}$ is a real, positive-definite, symmetric matrix representation of the norm. Again, this matrix is not diagonal because the D_e matrix is involved. Also, the same three assumptions regarding the t_m integration in the $\mathcal{Q}_{|\underline{J}_{eq}|}$ norm are made here as well.

To understand the nature of the surface Laplacian, first consider the Laplacian of a solenoidal vector field $\underline{a}$, which is given by:

$$\nabla^2 \underline{a} = -\nabla \times \nabla \times \underline{a} \tag{113}$$

The link to the surface Laplacian comes from ignoring the radial components of $\underline{a}$ and the ∇ operator. In the case of

$\underline{J}_{eq,p>0}$, a surface vector whose stream function $\Psi_{p>0}$ has no radial dependence, the two operators are identical:

$$\nabla_s^2 \underline{J}_{eq,p>0} = \nabla^2 \underline{J}_{eq,p>0} \tag{114}$$

$$= -\nabla \times \nabla \times \underline{J}_{eq,p>0} \tag{115}$$

$$= -\nabla \times \nabla \times \nabla \times \hat{\underline{r}} \Psi_{p>0} \tag{116}$$

$$= \nabla \times \hat{\underline{r}} \nabla_s^2 \Psi_{p>0} \tag{117}$$

where:

$$\nabla_s^2 \Psi_{p>0} = \Re \left\{ \frac{1}{\mu_0} \sum_{s=-2}^{2} \sum_{p=1}^{4} \sum_{l=p-1}^{p+1} \sum_{k=\max(1,|l|)}^{|l|+40} \tilde{\varepsilon}_{ksp}^{l} \cdot \right.$$
$$\left. \sum_{n=1}^{60} \sum_{m=-\min(n,12)}^{\min(n,12)} (d_{kn,e}^{lm})^* n(2n+1) S_{nsp,e}^{m} \mid_{r=a+h} \right\} \tag{118}$$

Note that the surface Laplacian operator multiplies $S_{nsp,e}^{m} \mid_{r=a+h}$ by a factor of $-n(n+1)$, and so $\mathcal{Q}_{|\nabla_s^2 \underline{J}_{eq,p>0}|}$ damps the higher degree harmonics much more severely than $\mathcal{Q}_{|\underline{J}_{eq}|}$, as intended.

It is anticipated that the magnetospheric field expansion of Eq. 56 includes many more coefficients than can be reliably estimated from the data at hand, especially those describing deviations from a dipole in magnetic local time. Experience from earlier phases of modeling suggests that excessive cross-talk or correlations between the ionospheric and non-D_{st} dependent magnetospheric expansions will likely exist as a result of poor field separation due to limited satellite data coverage in local time. Therefore, a magnetospheric solution is sought which is smooth in some sense that will reduce this coupling. Specifically, define a third quadratic norm, $\mathcal{Q}_{|\Delta \underline{B}_{ltd}|}$, which measures the mean-square magnitude of the deviations from a dipole in magnetic local time ($k > 1$ or $l \neq p$) and independent of D_{st} on a sphere at Magsat altitude ($r = a + h_m$ with $h_m = 450$ km), Ω, over time:

$$\mathcal{Q}_{|\Delta \underline{B}_{ltd}|} = \int_0^T \int_\Omega |\Delta \underline{B}_{ltd}(\theta_d, \phi_d, t_m)|^2 \, d\Omega d\tau_m \Big/ \int_0^T \int_\Omega d\Omega d\tau_m \tag{119}$$

$$= \frac{1}{4\pi T} \int_0^T \int_\Omega |\Delta \underline{B}_{ltd}(\theta_d, \phi_d, t_m)|^2 \sin\theta_d d\theta_d d\phi_d d\tau_m \tag{120}$$

where $\Delta \underline{B}_{ltd}$ includes all μ_{ksp}^{l} terms in Eq. 56 for which $k > 1$ or $l \neq p$. This may be written in matrix notation as:

$$\mathcal{Q}_{|\Delta \underline{B}_{ltd}|} = \underline{u}^T \Lambda_{|\Delta \underline{B}_{ltd}|} \underline{u} \tag{121}$$

with:

$$\underline{u} = \begin{pmatrix} \Re\{\underline{\mu}\} \\ \Im\{\underline{\mu}\} \end{pmatrix} \tag{122}$$

where $\Lambda_{|\Delta \underline{B}_{ltd}|}$ is a real, positive-definite, diagonal matrix representation of the norm.

Also recall that the radial component of the meridional coupling currents of the EEJ are being accounted for in the Magsat observations via $\delta \underline{B}$ in Eq. 65, requiring QD degrees of up to $k = 40$. Hence, the $T_{ks,j}^{l}$ will be susceptible to instabilities similar to those of $T_{ksp,e}^{l}$, and consequently, the associated J_r for both dawn and dusk will need to be smoothed. Consider that the inclination of the Magsat orbit was such that no data were aquired within a cap of half-angle of about 7° centered on the geographic poles [*Langel and Estes*, 1985a]. This, combined with the fact that J_r is expressed in dipole coordinates, makes damping the polar regions a neccessity for both dawn and dusk. Furthermore, since J_r shows little structure at low and mid-latitudes during dawn, there is no need to introduce a θ_d influence function as in $\mathcal{Q}_{|\nabla_s^2 \underline{J}_{eq,p>0}|}$. Although the EEJ coupling currents are present at dusk along the dip equator, the inclusion of an influence function which is small only at low dipole latitudes is complicated, and so it is omitted in this study.

To this end, define a fourth type of quadratic norm, $\mathcal{Q}_{|J_r|}$, which measures the mean-square magnitude of J_r on a sphere at Magsat altitude ($r = a + h_m$ with $h_m = 450$ km), Ω, over time:

$$\mathcal{Q}_{|J_r|} = \int_0^T \int_\Omega J_r^2(\theta_d, \phi_d, t) d\Omega d\tau \Big/ \int_0^T \int_\Omega d\Omega d\tau \tag{123}$$

$$= \frac{1}{4\pi T} \int_0^T \int_\Omega J_r^2(\theta_d, \phi_d, t) \sin\theta_d d\theta_d d\phi_d d\tau \tag{124}$$

where:

$$J_r = \Re \left\{ \frac{1}{\mu_0 (a + h_m)} \sum_{s=0}^{2} \sum_{k=1}^{40} \sum_{l=0}^{\min(k,4)} \tilde{\phi}_{ks}^{l} \cdot \sum_{n=1}^{60} \sum_{m=-\min(n,12)}^{\min(n,12)} (d_{kn,j}^{lm})^* n(n+1) S_{ns,j}^{m} \mid_{r=a+h_m} \right\} \tag{125}$$

or in matrix notation:

$$\mathcal{Q}_{|J_r|} = \underline{\tilde{w}}^T \Lambda_{|J_r|} \underline{\tilde{w}} \tag{126}$$

with:

$$\underline{\tilde{w}} = \begin{pmatrix} \Re\{\underline{\tilde{\phi}}\} \\ \Im\{\underline{\tilde{\phi}}\} \end{pmatrix} \tag{127}$$

The $\Lambda_{|J_r|}$ matrix is real, positive-definite, and symmetric. It is also non-diagonal because of the implied D_j matrix multiplicaton in Eq. 125. Because J_r has a period of one year, $T = 1$ yr. Again, there are separate $\mathcal{Q}_{|J_r|}$ included for both dawn and dusk.

Finally, no regularization was applied to the lithospheric fields or to main field secular variation. Though arguments could be made for smoothing them outright, the intent is to see how they are affected by the coestimation of the other field sources. This makes CMP3 useful for core field and lithospheric studies that must avoid artificial smoothing. The efficient parameterization of the main field secular variation will be dealt with in future versions of the model where it will be a critical issue in extending the time domain to include satellite missions such as Oersted, Oersted-2/SAC-C, and Champ.

4.4 Weighting

In this section the issue of data weighting is discussed. In particular, the known portion, W^{-1}, of the data noise covariance matrix C_ν will be defined. To do so, several simplifying assumptions are made: first, the elements of $\underline{\nu}$ are considered to be uncorrelated, rendering W^{-1} diagonal; secondly, the error processes within a particular data subset are treated as stationary, that is, they are translationally invariant, rendering all W^{-1} diagonal elements corresponding to a particular vector component of a particular data subset equal; and thirdly, the scalar noise process is considered Gaussian, which is only true if the process is isotropic.

In this context, the data subsets, or $\underline{\nu}$ subvectors, should be chosen to reflect distinct stochastic populations with respect to both measurement error and model parameter inadequacies. The subsets considered in this study are listed as headers of the horizontal divisions of Table 2, and are indeed divided along lines of instrumentation differences (Magsat, POGO, and observatories) and differences in the physical properties of what is being measured (annual versus hourly means, dawn versus dusk, high versus low/mid dipole latitude). The POGO pass is distinguished from the POGO decimated data set primarily because of the selection procedure. Further assumptions are made concerning the variation of the error processes with respect to orientation: the observatory annual and low/mid dipole latitude ($|90° - \theta_d| < 50°$) hourly means processes are considered isotropic; the high dipole latitude ($|90° - \theta_d| \geq 50°$) observatory hourly means and Magsat dawn and dusk processes are considered isotropic in the XY-plane; and the Magsat dawn and dusk mid/low dipole latitude processes are considered isotropic in the XZ-plane.

What remains is to assign the actual variances of the different error processes defined in this study. This is accomplished by iteratively adjusting a starting set of variances such that the $s_{d_i}^2$ values of Eq. 98, corresponding to the various data subsets, approach unity. This of course requires that a model be fit to the data. Because this is a computationaly intensive venture, and because only order-of-magnitude accuracy is needed, a preliminary model, denoted A, developed during the initial stages of this study is used once for all. Only the main field portion ($n = 1, \ldots, 13$ terms in Eq. 6) of the core and lithospheric field parameterization in the CMP3 model is included in the A model, though vector biases are also included for observatory annual and hourly means. For the A model ionosphere, $D_e = I$, $F = Q$, and $G = C$, $s = -2, \ldots, 2$, $p = 1, \ldots, 4$, $L = 1$, $K(0) = 7$ and $K(\neq 0) = 3$, and there is no $F_{10.7}$ dependence. For the magnetosphere, $D_e = I$ and $F = Q$, $s = -2, \ldots, 2$, $p = 0, \ldots, 5$, $L = 0$, $K(0) = K(\neq 0) = 5 - |l|$, and there is a linear D_{st} dependence on the $k = 1$ terms. Finally, for the coupling currents, $s = 0$, $K_{max} = 30$, and $L_{max} = 6$ for both the dawn and dusk expansions. The A model also includes damping on the coupling current parameters for both dawn and dusk via quadratic norms of the form $\mathcal{Q}_{|J_r|}$ of Eq. 123. The *a priori* data noise variances used in the CMP3 model resulting from this procedure are listed in the σ_ν column of Table 2.

This procedure also provides an opportunity to reject gross outliers with respect to the A model. Specifically, residuals in the Magsat mid/low and high dipole latitude data sets greater that 25 nT and 100 nT, respectively, are rejected as are observatory hourly means residuals greater than 150 nT and POGO residuals greater than 25 nT. The resulting measurement counts for the various data sets are listed in the *Number* column of Table 2.

4.5 Application

The iterative Gauss LS estimator of Eq. 92 was used to estimate the parameters defined in the CMP3 model. A total of two iterations were taken, though the second resulted in negligible adjustments, from a starting point, $\underline{x}_0$, provided by a preliminary model known as B, a successor to A. This model differs from A only in that it includes the $F_{10.7}$ solar flux dependence of Eq. 44, and that it includes damping on the magnetospheric parameters via a quadratic norm, $\mathcal{Q}_{|\underline{B}_{mag}|}$, which measures the mean-square magnitude of the magnetospheric field, $\underline{B}_{mag}$, over Earth's surface, Ω, and over time:

$$\mathcal{Q}_{|\underline{B}_{mag}|} = \int_0^T \int_\Omega \left|\underline{B}_{mag}(\theta_d, \phi_d, t_m)\right|^2 d\Omega d\tau_m \Big/ \int_0^T \int_\Omega d\Omega d\tau_m \tag{128}$$

The B model, also referred to as the GSFC/CU(12/96) model, has been used by *Purucker et al.* [1997] to study north-south trending anomalies of lithospheric origin, particularly over Australia.

Looking at Eq. 92, the measurement vector, $\underline{d}$, is of length 524230 and is provided by observatories, Magsat, and POGO; the current model state, $\underline{x}_n$, whose starting value, $\underline{x}_0$, was just discussed, is of length 16821; the matrix of partial derivatives, A_n, is derived from Eqs. 82 to 86; the weight matrix, W, has been discussed in Section 4.4; and the five ($k = 5$) quadratic smoothing norms ($\underline{x}_{a_i} = \underline{0}$ for each of $\mathcal{Q}_{|\underline{J}_{eq}|}$, $\mathcal{Q}_{|\nabla_s^2 \underline{J}_{eq,p>0}|}$, $\mathcal{Q}_{|\Delta \underline{B}_{ltd}|}$, and $\mathcal{Q}_{|J_r|}$ dawn and dusk) have been discussed in Section 4.3.

The last ingredient required is the selection of damping parameter values, λ_i, associated with each norm. Because the matrix representations of the norms, Λ_i, used in this study are all positive-definite, each $\mathcal{Q}_i$ is a monotonically decreasing function of its associated λ_i [*Bloxham et al.*, 1989]. This has lead some researchers to construct linear-linear or log-linear trade-off curves of $\mathcal{Q}_i$ as a function of $\mathcal{L}_r$ and choose λ_i corresponding to the model that lies at the inflection point (knee) of the curve [*Sabaka et al.*, 1997], or construct log-log curves and select the model lying at the point of negative unit slope [*Voorhies*, 1995]. In most of these cases, however, there is usually only one norm applied, requiring the exploration of a trade-off curve instead of a multi-parameter surface. Because five norms are employed in this study and because the number of parameters is large, a full trade-off study is impractical and so the more qualitative method of visual inspection is used. This is thought to suffice for two reasons: first, the $\mathcal{Q}_i$ measure physically meaningful quantities about which qualitative *a priori* knowledge abounds and which can be visually checked; and secondly, the λ_i have logarithmic influence on the norms (as manifested by the trade-off curves) and so only an order of magnitude accuracy is needed. The additional criterion of low correlation between ionospheric

Table 1: Damping parameter values used in the CMP3 model.

Norm	Damping parameter (λ)	
$\mathcal{Q}_{\lvert \underline{J}_{eq} \rvert}$	1.3×10^{3}	$(\mathrm{A/km})^{-2}$
$\mathcal{Q}_{\lvert \nabla_s^2 \underline{J}_{eq,P>0} \rvert}$	1.5×10^{-2}	$(\mathrm{A/km^3})^{-2}$
$\mathcal{Q}_{\lvert \Delta \underline{B}_{ttd} \rvert}$	6.3×10^{4}	$(\mathrm{nT})^{-2}$
$\mathcal{Q}_{\lvert J_r \rvert}$ dawn	1.3×10^{1}	$(\mathrm{nA/m^2})^{-2}$
$\mathcal{Q}_{\lvert J_r \rvert}$ dusk	1.3×10^{1}	$(\mathrm{nA/m^2})^{-2}$

and magnetospheric coefficients was instrumental in selecting the $\mathcal{Q}_{|\Delta \underline{B}_{ttd}|}$ damping parameter value. The selected values for the λ_i are listed in Table 1.

5 Results

The CMP3 model may be examined at two levels: the first may be called the purely inverse theoretical level, which addresses the self-consistency of the model, i.e. fitting efficiency, parameter separability, resolution, etc.; and the second may be called the physical plausibility level, which assesses the validity of the mathematical representations of real physical phenomena. The first of these levels will now be dealt with.

5.1 Residuals and data fits

The most natural way of evaluating the worth of a model is to see how well it fits data from whence it was derived (interpolatory) and data of which it has no direct knowledge (extrapolatory). To this end, Table 2 lists the unweighted residual statistics, i.e. the mean, μ_r, and standard deviation, σ_r, of the CMP3 model for each field measure for each of the data subsets of interest. Also listed is the *a priori* standard deviation of the associated noise, σ_ν. One can immediately see that the μ_r for the observatory annual and hourly means are zero, which is a result of coestimating vector biases at those stations. With the exception of Magsat polar dusk X and Magsat dawn Z, the remaining μ_r have magnitudes well below 1 nT, indicating that the mean field signal of those data subsets is being described fairly well by the model. It is also clear that the trend in σ_r roughly matches that of σ_ν. This is to be expected since the latter give information on the relative importance of each data subset which the estimator then fits accordingly, as measured by the former. In light of the assigned σ_ν values, the mid/low dipole latitude subsets of Magsat and the observatory hourly means are fit substantially better than their high latitude counterparts; within the mid/low dipole latitude Magsat dawn and dusk subsets scalar B is fit best (uneffected by attitude errors) whilst Y is fit slightly worse (possibly the result of dynamic variability in the meridional current system); the POGO B are fit significantly worse than Magsat B even though their numbers and σ_ν are comparable; and the observatory annual means are fit much worse than all other subsets (for reasons not yet fully understood).

To gain a better understanding of the residual behavior, residual histograms are plotted in Fig. 5 for the mid/low dipole latitude Magsat dawn and dusk and observatory hourly means subsets, as well as the high latitude hourly means subset, along with Gaussian curves having the same μ_r and σ_r. The vector residuals of both of the Magsat data subsets conform well with the superimposed Gaussian, even the B distributions appear to fall within the normal regime, though the comparison is only appropriate in the isotropic case. Conversely, the residual distributions for the hourly means are clearly too long-tailed to be Gaussian. Histograms for the annual means and the high latitude Magsat subsets also exhibit these long-tail features. Though it is a tautology to infer the distribution of errors on the basis of residuals from a model, as pointed out by *Bloxham et al.* [1989], it is clear that these latter data subsets are in need of further scrutiny, especially when considering that these outliers can have significant influence in a least-squares estimation. If the errors in POGO B are believed to be Gaussian, then its histograms also show somewhat thickened tails, suggesting an additional cycle of outlier rejection. Undetected outliers may be the reason for the anomalously high σ_r values in both the POGO and the annual means data.

Table 2: CMP3 unweighted residual statistics (μ_r, σ_r, and σ_ν in units of nT).

Component	Number	μ_r	σ_r	σ_ν
Observatory annual-means				
X	4047	0.0	29.7	34.0
Y	4047	0.0	44.3	34.0
Z	4047	0.0	37.4	34.0
Observatory hourly-means				
$\|90° - \theta_d\| < 50°$				
X	56963	0.0	10.1	11.0
Y	57016	0.0	12.8	11.0
Z	55978	0.0	9.1	11.0
$\|90° - \theta_d\| \geq 50°$				
X	65451	0.0	17.0	18.0
Y	65487	0.0	15.5	18.0
Z	65230	0.0	19.9	21.0
Magsat dusk				
X	9381	-0.04	4.6	5.4
Y	9321	-0.03	5.8	6.8
Z	9382	0.2	4.4	5.4
B	11404	0.5	3.7	5.5
Magsat polar dusk				
X	7985	-1.8	15.8	18.5
Y	7988	0.3	16.5	18.5
Magsat dawn				
X	10570	0.2	4.4	5.0
Y	10537	-0.002	4.6	5.4
Z	10588	-1.9	3.8	5.0
B	12441	-0.1	3.6	5.3
Magsat polar dawn				
X	8483	-0.6	17.4	19.0
Y	8445	0.1	18.2	19.0
POGO decimated				
B	22685	-0.2	5.1	4.8
POGO pass				
B	6754	-0.05	6.7	5.8

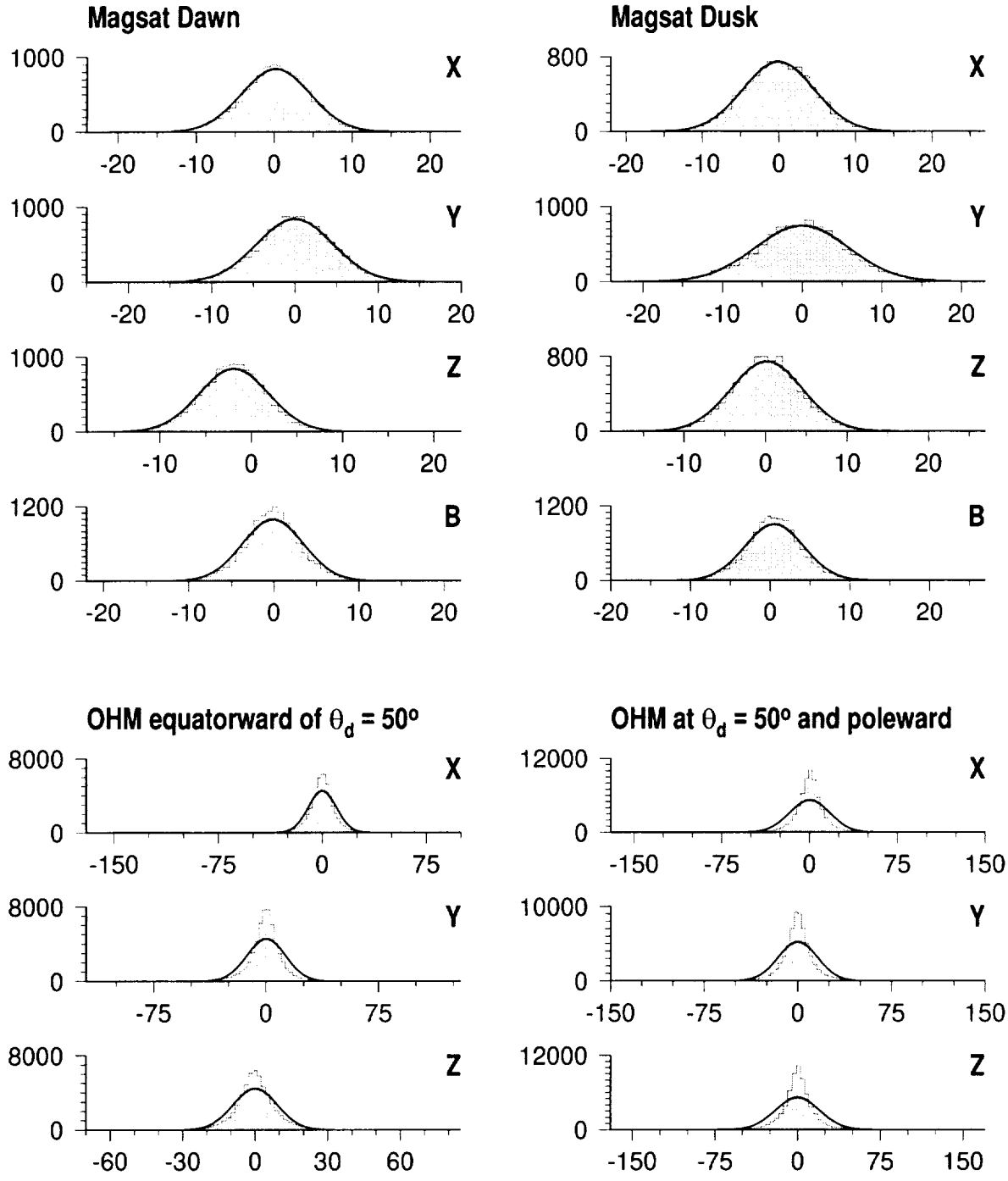

Figure 5: Residual histograms for the Magsat dawn and dusk and observatory hourly means (OHM) data versus the CMP3 predictions. The abscissa are all in units of nT, with bin widths of $\frac{1}{5}\sigma$, and the ordinates are counts. Gaussian curves with appropriate μ_r and σ_r from Table 2 have been normalized to the area of the associated histogram and then superimposed.

Thus far, the quality of fit of the CMP3 model has been analyzed only through statistical measures. The focus now shifts to a more datum oriented perspective as provided by selected observatory time series and satellite pass plots. The Tucson annual and hourly means data used in the model are shown in Fig. 6 at two different time scales, along with the values predicted by CMP3. The top panel shows all available data for the 1960 to 1985 time span along with the predicted hourly means and main field values. At this scale, the baselines of the annual and hourly means appear to be very similar and the Y and Z predicted main fields fit both nicely. However, the X main field exhibits peculiar excursions between the hourly means clusters which define the POGO and Magsat mission envelopes. This may be evidence for some type of annual means outlier in the vicinity of Tucson that attempts to deflect the main field in the absence of influential hourly means data. The bottom panel shows the hourly means data for the quietest day of each month for 1967 along with the predicted values. The fits here are truly satisfying, especially when considering the adjustment for the jump discontinuity, due to a change in external field strength (ring-current level), between the quietest days of May and June in X and Z.

Similar plots are provided in Fig. 7 for the Huancayo observatory, which is located under the EEJ. The top panel shows similar behavior as in the case of Tucson, except Z is now exhibiting the excursions. Again, annual means outliers are suspected. The bottom panel is now for the year 1966 and shows what is considered excellent fits to all three components. Note the adjustment in X for the jump discontinuity between the quietest days of June and July caused by different levels of ring-current activity.

Moving to the satellite pass plots, Fig. 8 shows the fit to B for a particular pass of POGO data that was included in the model analysis. This pass crosses the geographic equator at $59°W$ at noon magnetic local time and its trace is indicated in the top panel. The bottom panel shows a progression of residuals: The symbols in the top member show observations minus the main field part of the model; the solid line represents what the model predicts for the magnetospheric part. The difference is shown as symbols in the next member; the solid line now represents the ionospheric part of the model. Note that there is a clear EEJ signature in the data, which the model is able to reproduce. Again the difference is taken, and hence the symbols in the bottom member are observations minus main, magnetospheric, and ionospheric parts of the model; the solid line represents the lithospheric part of the model. Since the total residual is the only thing of interest in this section, it may be realized by comparing the squares and the black line in the bottom member. Though the fit is satisfactory for most of the pass (roughly 10 nT or less), it begins to diverge north of about $40°$ geographic latitude. This is probably due to the influence of polar current systems, whose dynamic behaviour is not included in the model.

The fit to the Z component for Magsat dusk pass 263, which was not included in the model, is shown in a similar format in Fig. 9. Again, looking at the bottom member of the bottom panel reveals a fit which is satisfactory for practically all of the pass (roughly 15 nT or less), although there may be some questions about the reality of some of the features, which will be discussed in a later section. The corresponding X and Y component residual progressions are shown in Fig. 10. The bottom members of the bottom panels indicate fits that do not deviate by more than about 15 nT for all of X and most of Y. The obvious exception is found in the polar region south of about $-60°$ geographic latitude. The importance of modeling the toroidal magnetic field at satellite altitude is illustrated in the member entitled "coupling currents" for the Y component residuals. This toroidal field is caused by radial currents impinging the sampling shell of the satellite, and there is clear evidence here for a signature in the Y component at low latitudes: the meridional current system connected with the EEJ. This model (probably the first to include the global, non-potential contribution at satellite altitude) is able to fit this feature.

An examination of the residual statistics and selected data fits from the CMP3 model suggest that it is doing a satisfactory job of interpolating the data used to derive it, although this data set may still contain some outliers. Extrapolation, at least to mid/low latitude Magsat dusk data, also seems valid. A more in depth discussion of the observatory time series and satellite pass plots, and their physical implications, will be undertaken in Section 6.

5.2 Correlations

Whenever models are estimated from imperfect distributions of imperfect data, parameter separability can become an issue. The CMP3 model is no exception: the observatories have a limited spatial distribution, Magsat samples only

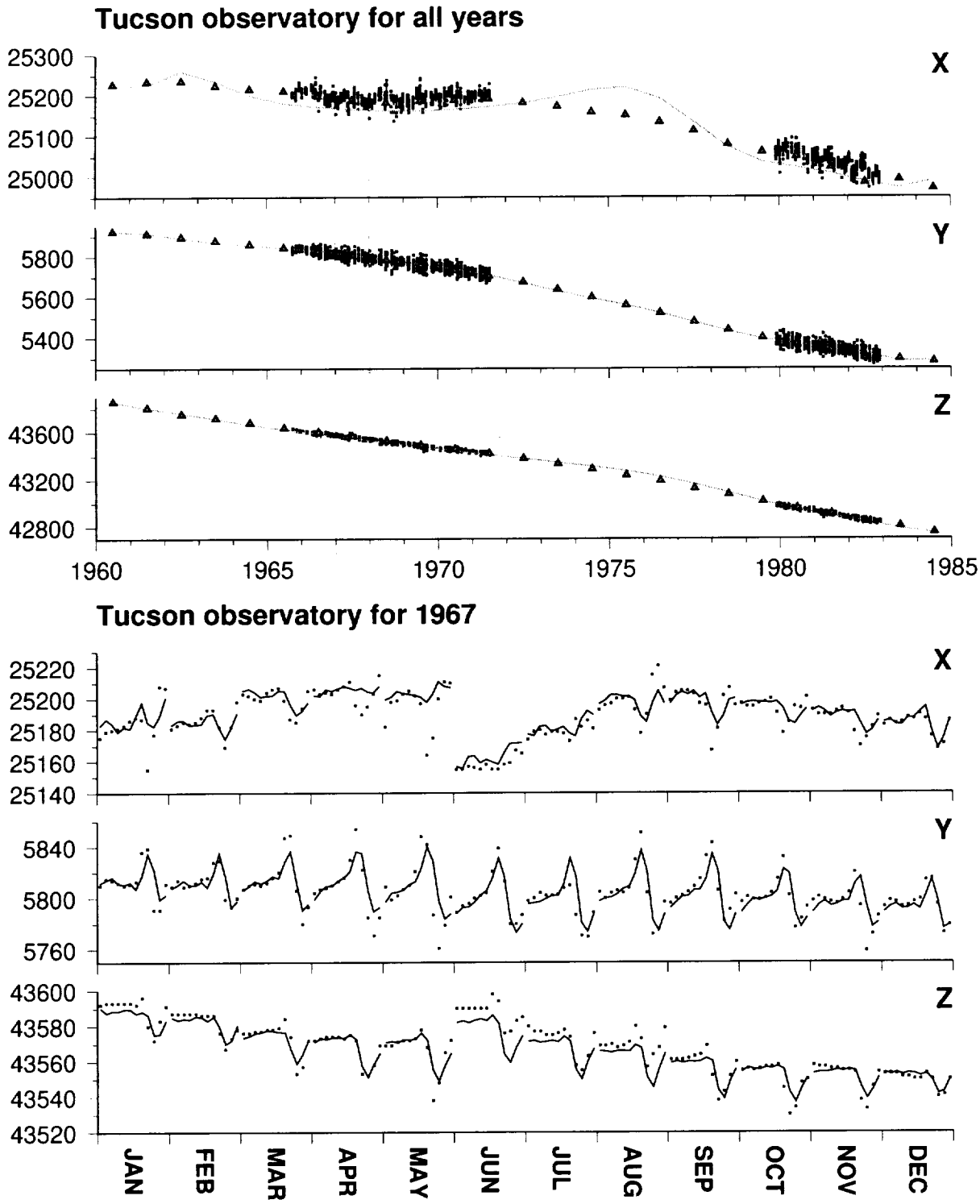

Figure 6: Fits of the CMP3 model to the components of the Tucson observatory annual and hourly means vector data. The top panel shows all measured annual (triangles) and hourly (squares) means data and the predicted main field (grey line), all in nT, over the time span of the model, in years. The bottom panel shows all hourly means (squares) and the model predictions (black line), all in nT, for the year 1967 (indicated by the box outline in the top panel). The abscissa in the bottom panel is discontinuous, being comprised of the quietest day of each month over the year, and begins at 0 UT for each day.

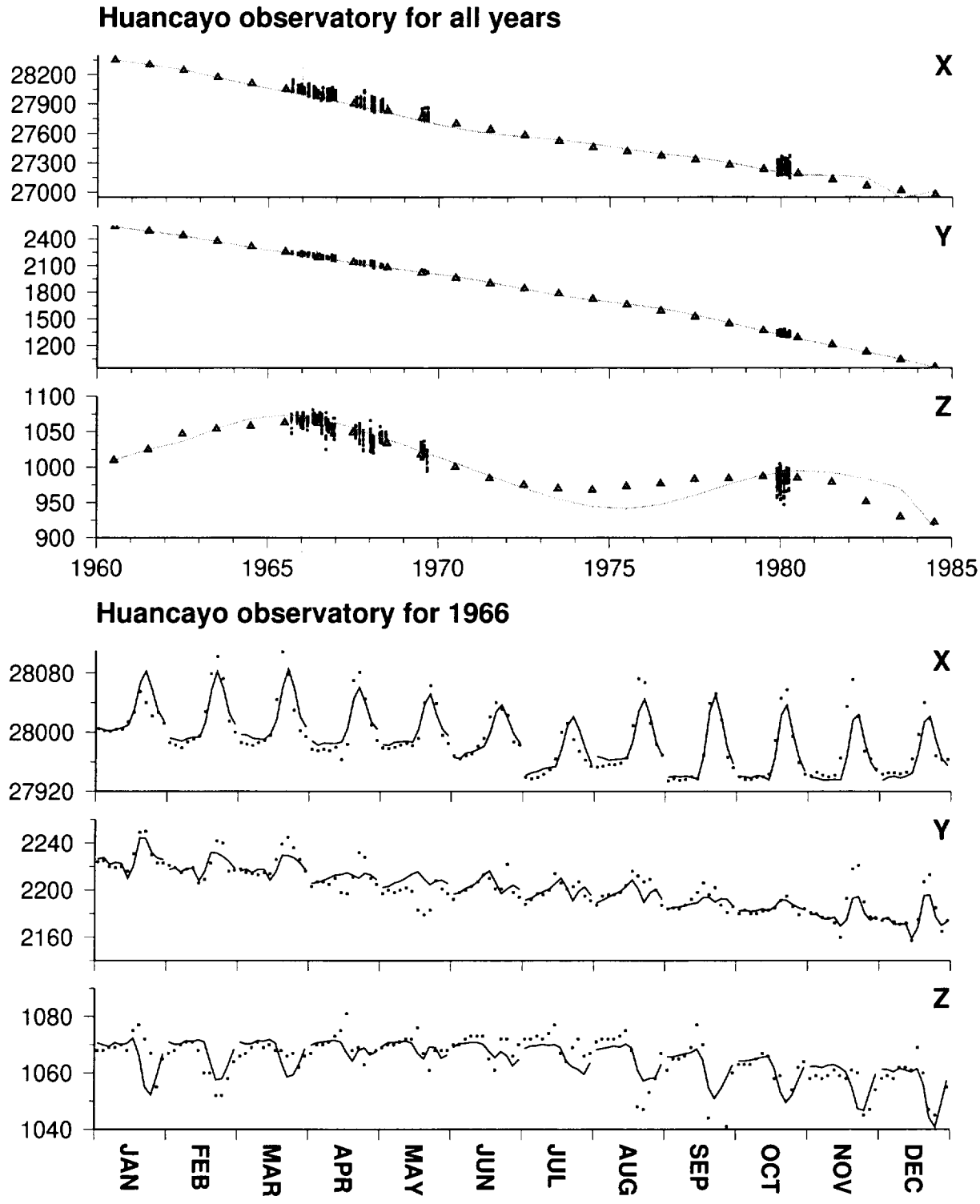

Figure 7: Fits of the CMP3 model to the components of the Huancayo observatory annual and hourly means vector data. The top panel shows all measured annual (triangles) and hourly (squares) means data and the predicted main field (grey line), all in nT, over the time span of the model, in years. The bottom panel shows all hourly means (squares) and the model predictions (black line), all in nT, for the year 1966 (indicated by the box outline in the top panel). The abscissa in the bottom panel is discontinuous, being comprised of the quietest day of each month over the year, and begins at 0 UT for each day.

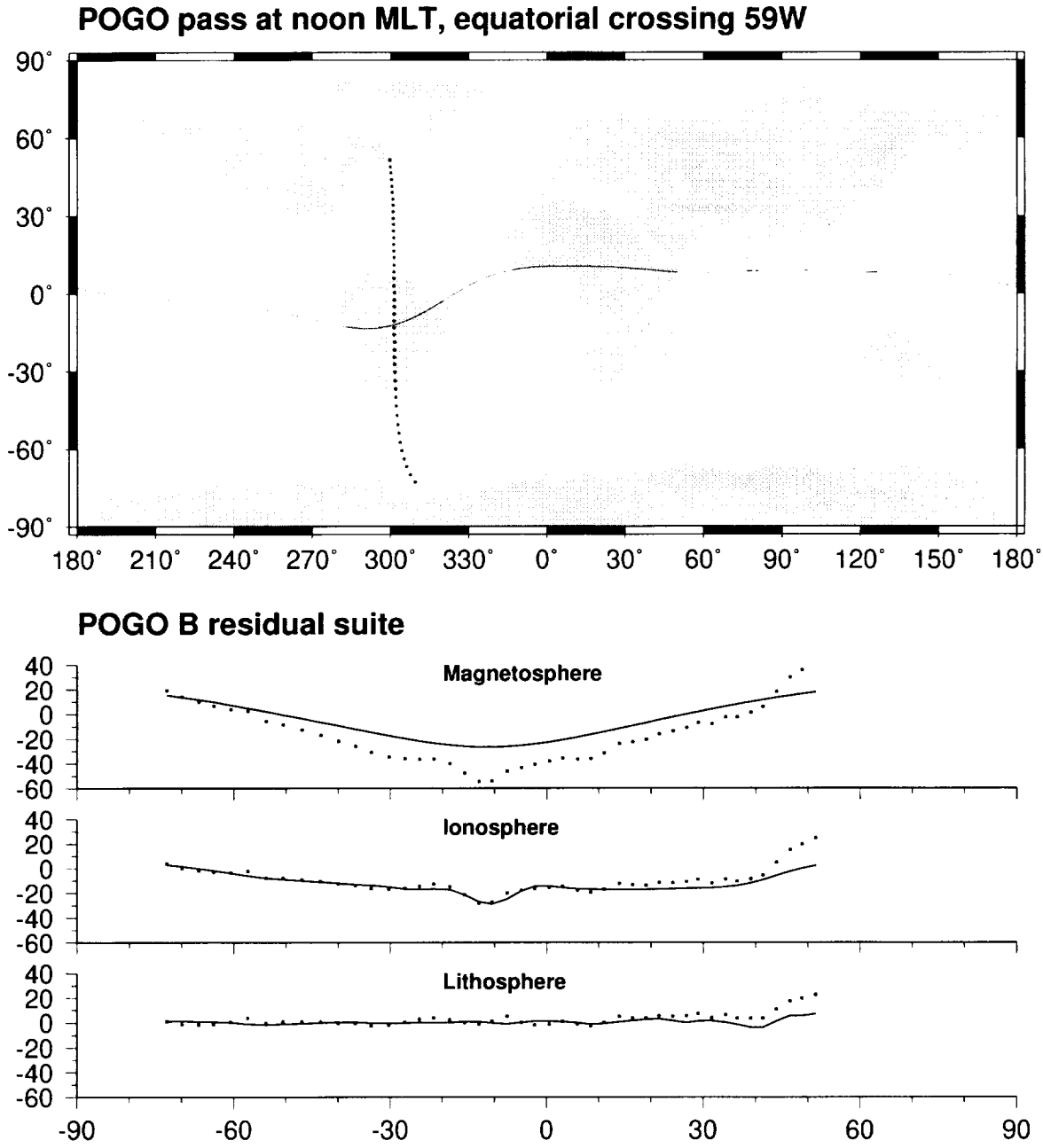

Figure 8: Fit of the CMP3 model to the scalar (B) values of a particular POGO pass used to derive the model. The top panel shows the angular positions of the pass locus, which in this case crosses the geographic equator at 59°W at noon magnetic local time (Cylindrical Equidistant projection). The magnetic dip equator can also be seen. The bottom panel is a suite of residual plots for the B data from this pass as a function of latitude. The progression is from the top to bottom member, with a given member showing residuals with respect to the main field plus all preceding labeled fields (squares) and the component of the predicted currently labeled field in the direction of the main field plus all preceding labeled fields (black line). All ordinates are in nT.

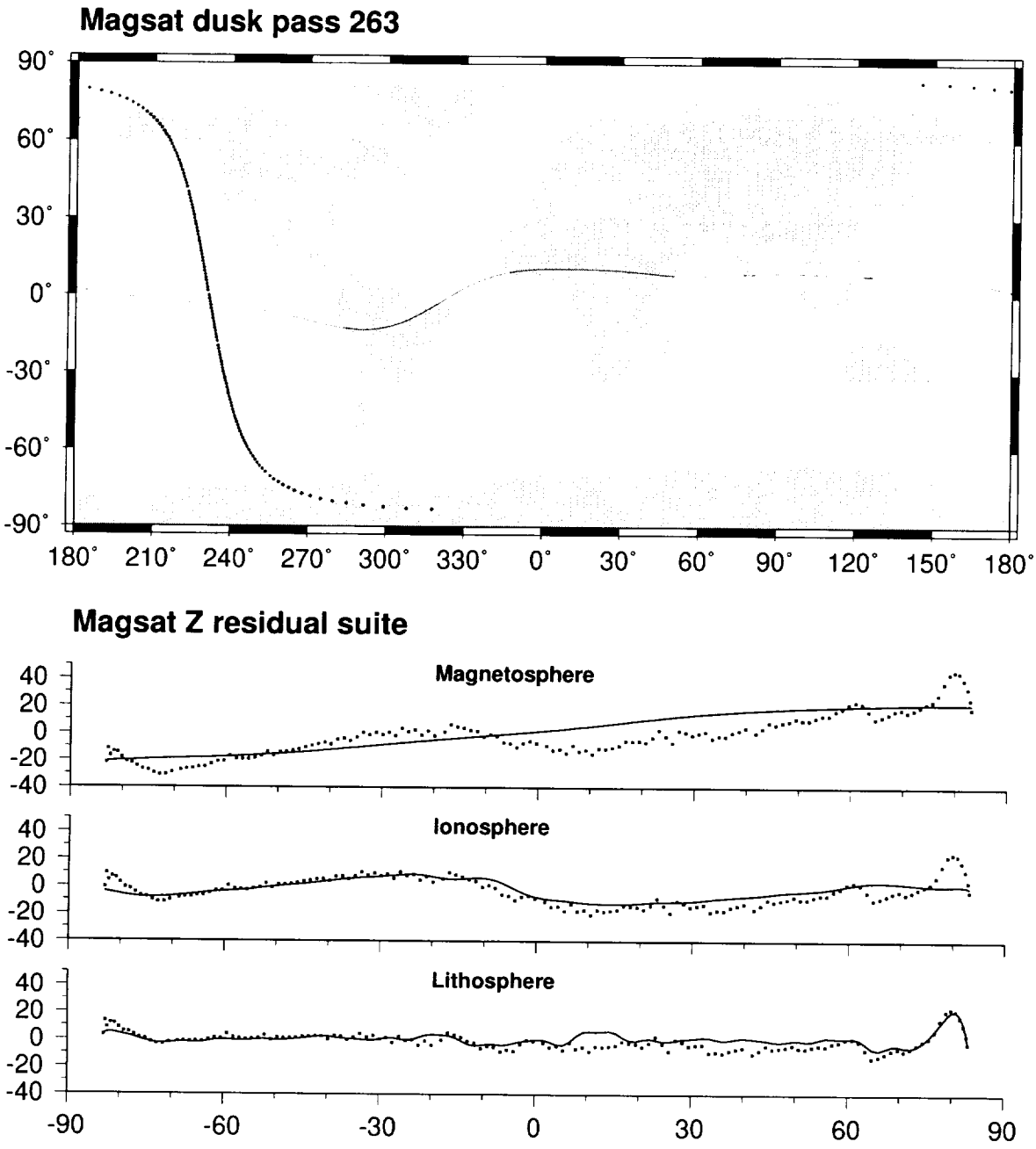

Figure 9: Fit of the CMP3 model to the Z component of the Magsat dusk pass 263, which was not used in deriving the model. The top panel shows the angular positions of the pass locus, which in this case crosses the geographic equator at 129°W (Cylindrical Equidistant projection). The magnetic dip equator can also be seen. The bottom panel is a suite of residual plots for the Z data from this pass as a function of latitude. The progression is from the top to bottom member, with a given member showing residuals with respect to the main field plus all preceding labeled fields (squares) and the Z component of the predicted currently labeled field (black line). All ordinates are in nT.

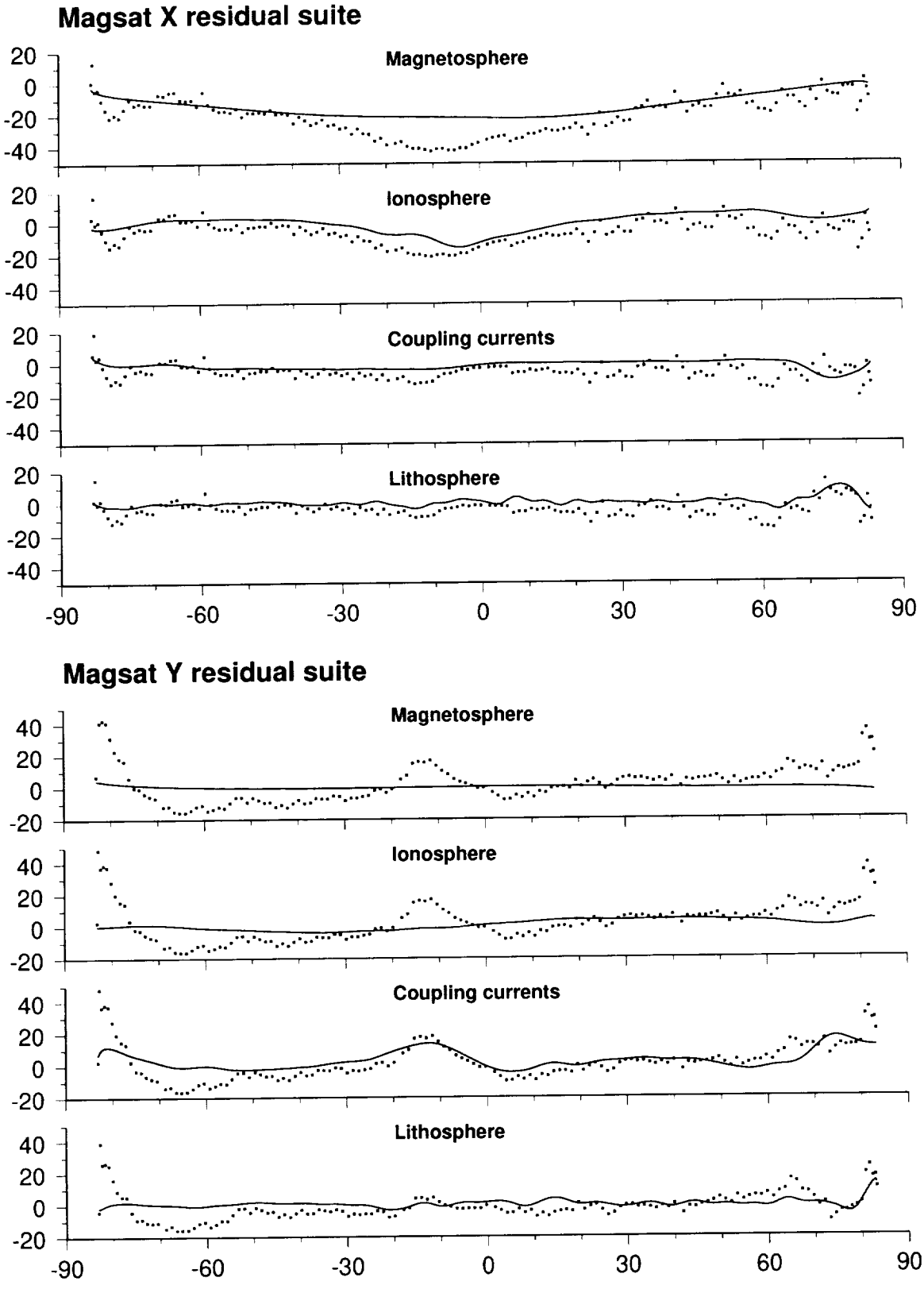

Figure 10: Fits of the CMP3 model to the X and Y components of the Magsat dusk pass 263. The top and bottom panels are suites of residual plots for the X and Y data, respectively, from this pass as a function of latitude. The progression is from the top to bottom member, with a given member showing residuals with respect to the main field plus all preceding labeled fields (squares) and the X and Y components of the predicted currently labeled field (black line). Note that fields from coupling currents are now included. All ordinates are in nT.

two local times, and POGO provides scalar measurements only. Combine this with the fact that global, high-resolution parameterizations of fields from several sources are being coestimated, and one can see that separability problems are inevitable. The usual remedy is to either reduce the number parameters or include some sort of regularization, which is commensurate to adding perfect data. To diagnose this problem, one can examine the correlations between model parameters or some linear functionals of them. If the (ij)-th element of the parameter error covariance matrix is given by:

$$(C_x)_{ij} = \nabla_{\underline{a}} x_i \cdot \nabla_{\underline{a}} x_j \tag{129}$$

where $\nabla_{\underline{a}} x_i$ is the gradient of the i-th parameter, x_i, with respect to the data (including *a priori* information), $\underline{a}$, then the (ij)-th element of the parameter correlation matrix, R_x, is given by:

$$(R_x)_{ij} = \frac{\nabla_{\underline{a}} x_i \cdot \nabla_{\underline{a}} x_j}{|\nabla_{\underline{a}} x_i| \, |\nabla_{\underline{a}} x_j|} = \cos \varphi_{ij} \tag{130}$$

where φ_{ij} is the angle between the gradients of x_i and x_j. Low or negligible correlations indicate that parameters are being distinguished by either a good data distribution of the right type of measurements and/or by regularization, while excessive correlations indicate that either the data distribution and/or the measurement types and/or the regularization is not sufficient for separability, which in any case suggest a reparameterization or enhanced regularization.

Elements of the CMP3 correlation matrix whose absolute value exceeds 0.7 were examined to gain an understanding of the separability problems. This threshold was chosen since it corresponds to a φ_{ij} of approximately 45°, the geometrical halfway point between the two extremes of being fully uncorrelated or fully correlated. The first of five major categories of correlations at this level is found between the γ_{nq}^m of Eq. 6 for $q > 0$, i.e. between the coefficients describing main field secular variation. These correlations are both positive and negative and are predominantly between the real or imaginary parts whose q values are within ± 4, but whose n and m values can be quite different. This may be attributed to the fact that the main field is no doubt over parameterized in the temporal domain, especially between the POGO and Magsat mission envelopes, and the behavior of the four quartic B-splines within each knot interval cannot be separated in many cases. Correlations between different n and m values indicate that the observatory spatial distribution is not sufficient to resolve the secular variation of all the harmonics without some type of regularization being employed.

The second category includes correlations amongst the observatory biases for both annual and hourly means. It is comprised of two types: those between biases at the same location; and those between biases at different locations. The former includes correlations across station breaks that may be due to both segments cross-talking with a main field secular variation which itself is correlated at that time scale, and correlations between the annual and hourly biases. Correlations between biases at spatially distinct points are intriguing because they may provide insight into spatial correlation lengths of crustal field sources on local scales. To investigate this, a global map was produced in which the locations of spatially distinct observatories were connected by a line if any annual or hourly means bias component of one was correlated with any annual or hourly means bias component of the other with an absolute value above 0.7, and is shown in the top panel of Fig. 11. The box outlines the European sector, which is zoomed in on in the bottom panel, and the circles have been added to help guide the eye to some of the more obscure lineations. The first thing to notice is that none of the line segments is longer than about 6° of arc and most are much shorter. This corresponds well with the resolution limit of the $N_{max} = 65$ truncation level of the core and lithospheric field expansion, and one would expect that any coherence at lengths longer than this would be described by the model. The second thing to notice is that the largest concentration and length of lines are found in Europe. This follows from the fact that the highest concentration of observatories is found in Europe. If a significant crustal correlation length is present elsewhere in the world, but is only sampled by one observatory, then this exercise will fail to detect it. Although a detailed interpretation will certainly not be attempted here, it must be said that some of the lineation patterns in Europe do appear to be related to known geological features. The polygon defined by the Tromsø(TRO), Abisko (ABK), and Kiruna (KIR) observatories agrees well with the location of the Kiruna crustal anomaly, while the east-west lineation between Nurmijärvi (NUR) and Voyeykovo (LNN) may be related to the Kursk anomaly. The complex of Wien Kobenzl (WIK), O Gyalla Pesth (OGY), Tihany (THY), and Nagycenk (NCK) and its extension to Fürstenfeldbruck (FUR) and Castellaccio (CAO) seems to follow the fabric of the Alpine region, while the east-west lineations in the Iberian peninsula may also be following regional trends.

The third group contains correlations found between the real or imaginary parts of the ionospheric parameters, $\tilde{\varepsilon}_{ksp}^l$, and are mostly of the type having like s, p, and l indicial values, but different k values, usually above 27.

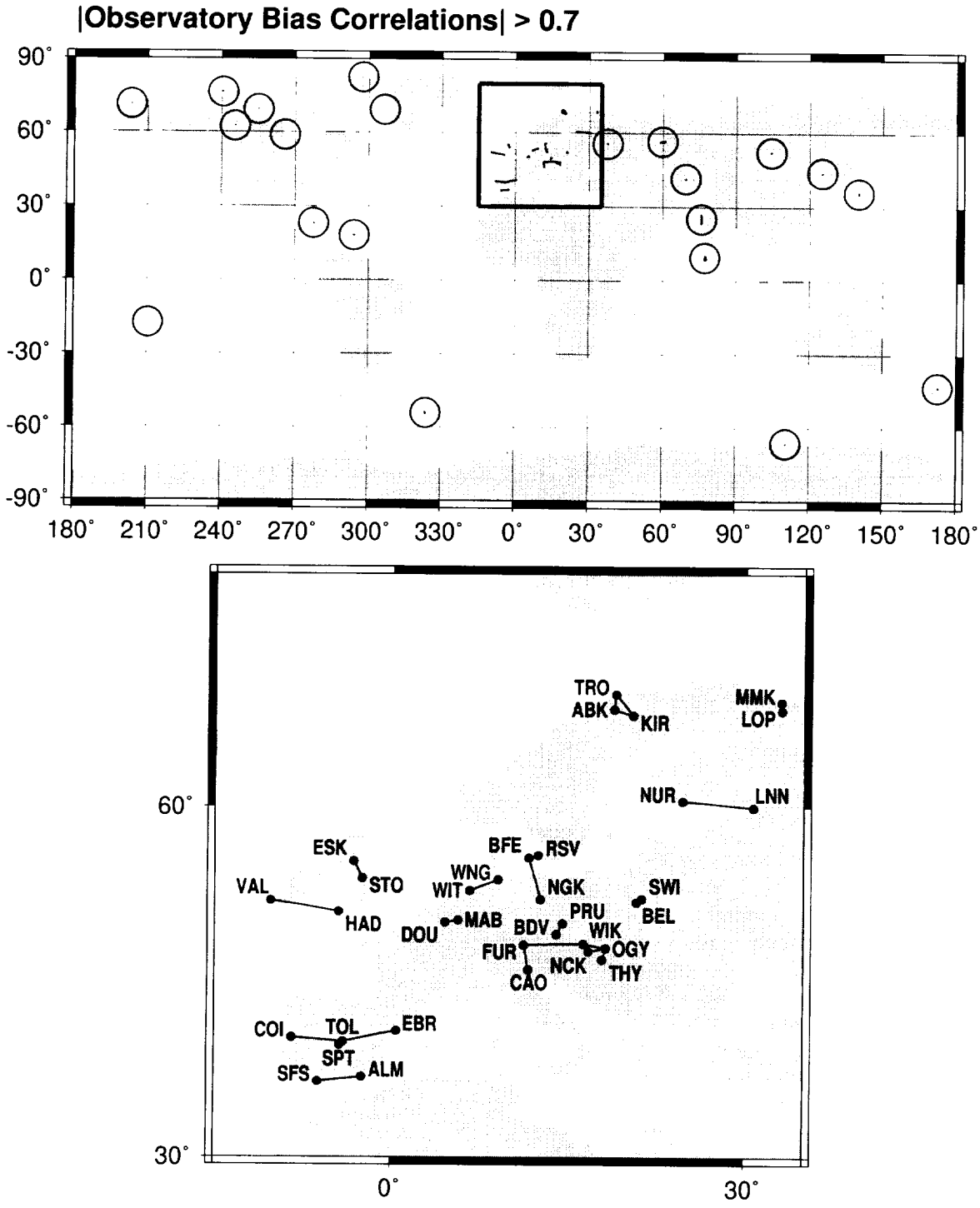

Figure 11: Observatory bias correlations between spatially distinct locations with absolute values above 0.7 shown as connecting lines (Cylindrical Equidistant projection). This includes correlations between any component of one observatory bias with any component of another. Circles have been added to the top panel as a visual aid in locating some of the more obscure lineations.

Apparently the high latitudinal resolution provided by each of these functions is not being distinguished by the data or the regularization.

Similarly, the fourth group contains correlations that are exclusively between the real or imaginary parts of the dawn or dusk coupling current parameters, $\tilde{\phi}^l_{ks}$, with like k and l indicial values, but different s values. Even with the phases of the basis functions fixed, the Magsat data and regularization are unable to resolve the associated amplitudes at this level.

The first four major categories of correlations involved those between parameters describing the same field source. These have been present in the main, ionospheric, and local crustal anomaly (biases) fields and fields from ionospheric coupling currents, and may be attributed for the most part to an over parameterization in time or space. The last category, however, represents the only significant cross-talk between field sources in the model. It involves negative correlations between the parameters of the non-D_{st} dependent magnetosphere, μ^l_{ksp}, and the ionosphere, $\tilde{\varepsilon}^l_{ksp}$, having like k, l, s, and p values. In a preliminary CMP3-type model that does not include the $\mathcal{Q}_{|\Delta \underline{B}_{tq}|}$ smoothing, these correlations exist in the $k \leq 4$ band. For the CMP3 model, these correlations exceed the 0.7 threshold (-0.70 to -0.81) only for the "tilt" component ($k = l = p = 1$) of the magnetic local time dipole, and most of that is in the noon-midnight direction (real part). Separation of these two field sources can only be accomplished by the Magsat and POGO satellite data, which of course sample the region between them. Hence, these correlations are considered diagnostic of poor data distribution and/or data type. To further illuminate this problem and judge its effects, the raw parameter correlations were mapped into measurement space, i.e. correlations were computed between two linear functionals of the parameters. If two field measurement types, B_a and B_b, are represented by the two functionals, $\underline{f}_a$ and $\underline{f}_b$, respectively, such that:

$$B_a = \underline{f}_a^T \underline{x}, \qquad B_b = \underline{f}_b^T \underline{x} \tag{131}$$

then their correlation, R_{ab}, is given by:

$$R_{ab} = \frac{\underline{f}_a^T C_x \underline{f}_b}{\sqrt{\underline{f}_a^T C_x \underline{f}_a} \sqrt{\underline{f}_b C_x \underline{f}_b}} \tag{132}$$

Specifically, Fig. 12 shows global maps (Mollweide projections) of the correlations between the predicted Z components of the magnetospheric and ionospheric fields from the preliminary CMP3-type model at Magsat altitude (450 km) for March 21, 1980, centered on noon magnetic local time, but for different magnetic universal times (MUT). As expected, the correlations are negative over almost the entire globe. The most striking features are the twin negative lobes located symmetrically about the geographic equator in the dusk sector, which persist for much of MUT. A peak negative correlation of -0.76 is found on the northern lobe. Hence, these correlations exceed the 0.7 threshold only over very localized portions of the maps, and may indicate that the overall cross-talk between magnetosphere and ionosphere is not that severe. However, inspection of predicted ionospheric field components at some observatory locations indicates substantial compensation by the magnetosphere, particularly over the summer and fall seasons where there is a paucity of Magsat data. For CMP3, a similar plot shows correlations whose magnitudes do not exceed 0.3, and predicted observatory time series show little if any compensation between magnetosphere and ionosphere.

5.3 Resolution and calibration

In a statistical framework, the LS objective function, $\mathcal{L}(\underline{x})$, is the negative exponent of a Gaussian probability density function (*pdf*) whose maximum likelihood is sought, and its terms represent the conjunction of information coming from products of Gaussian *pdf*'s. The relative importance of these pieces of information is conveyed through the data misfit factors and the damping parameters. How these are chosen and what their effects are upon the model state are matters of resolution and calibration. The former gives insight into what and how many parameters are determined by which particular pieces of information, at least in the statistical sense, while the latter provides a guide to making the formal errors consistent with reality, at least as measured by the data.

Various quantities related to these matters have been computed for the CMP3 model and listed in Table 3. All have been introduced in Section 4.2, and reflect both the data subsets defined in Table 2 and the various norms discussed

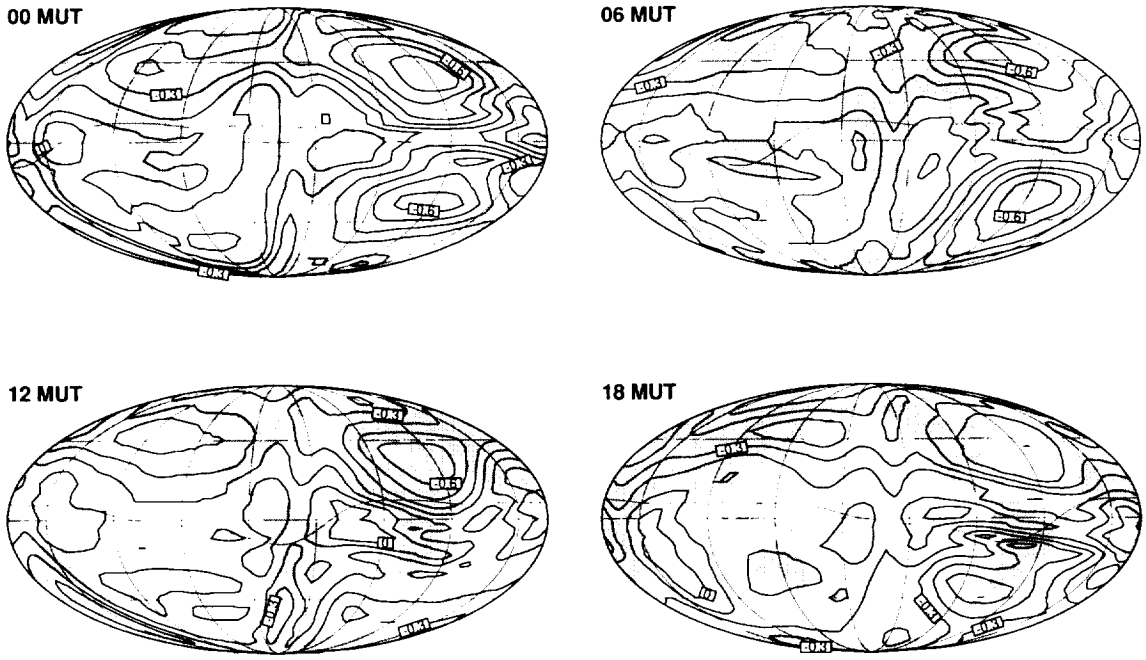

Figure 12: Global correlation map between the predicted Z components of the magnetospheric and ionospheric portions of the field from a preliminary CMP3-type model, with no $\mathcal{Q}_{|\Delta \underline{B}_{itd}|}$ smoothing, on the sphere $r = 6821.2$ km for March 21, 1980 (Mollweide projection). Each of the four panels is centered on noon magnetic local time, but for different magnetic universal times (MUT). The associated induced contributions are included in both magnetospheric and ionospheric Z.

Table 3: CMP3 resolution and calibration information.

Data subset	$\mathcal{L}_{r_i}(\underline{\tilde{x}})$	N_i	$tr\,[R_{d_i}]$	$E\,[\mathcal{L}_{r_i}(\underline{\tilde{x}})]$	$s^2_{d_i}$
Observatory annual-means	14851.7	12141	2005.7	10135.3	1.47
Observatory hourly-means					
$\|90° - \theta_d\| < 50°$	163532.9	169957	2088.4	167868.6	0.97
$\|90° - \theta_d\| \geq 50°$	165512.9	196168	1378.4	194789.6	0.85
Magsat dusk	24975.8	39488	2731.6	36756.4	0.68
Magsat polar dusk	12177.0	15973	213.2	15759.8	0.77
Magsat dawn	27684.6	44136	2639.7	41496.3	0.67
Magsat polar dawn	14861.5	16928	193.0	16735.0	0.89
POGO decimated	25608.1	22685	636.8	22048.2	1.16
POGO pass	9011.4	6754	189.4	6564.6	1.37
subtotal	458216.0	524230	12076.2	512153.8	0.89
Norm	$\mathcal{L}_{e_i}(\underline{\tilde{x}})$	M_i	$tr\,[R_{a_i}]$	$E\,[\mathcal{L}_{e_i}(\underline{\tilde{x}})]$	$s^2_{a_i}$
$\mathcal{Q}_{\|\underline{J}_{eq}\|}$	10355.6	5520	1668.2	3851.8	2.69
$\mathcal{Q}_{\|\nabla^2_S \underline{J}_{eq,p>0}\|}$	1173.2	4910	1459.9	3450.1	0.34
$\mathcal{Q}_{\|\Delta \underline{B}_{itd}\|}$	3040.9	740	617.6	122.4	24.85
$\mathcal{Q}_{\|J_r\|}$ dawn	757.9	1044	474.6	569.4	1.33
$\mathcal{Q}_{\|J_r\|}$ dusk	746.2	1044	524.4	519.6	1.44
subtotal	16073.8	13258	4744.8	8513.2	1.89
grandtotal	474289.8	537488	16821.0	520667.0	0.91

in Section 4.3. Focusing on the fourth column, which gives the trace of the resolution matrix corresponding to either the data subset or the norm, it can be seen that the combined data sets are resolving about 72% of the 16821 total parameters. Of these, about 45%, 48%, and 7% are resolved by the observatories, Magsat, and POGO, respectively. As for the norms, 10%, 8.5%, and 3.5% of the parameters are resolved by $\mathcal{Q}_{|\underline{J}_{eq}|}$, $\mathcal{Q}_{|\nabla_s^2 \underline{J}_{eq,p>0}|}$, and $\mathcal{Q}_{|\Delta \underline{B}_{ltd}|}$, respectively, while $\mathcal{Q}_{|J_r|}$ dawn and dusk both resolve about 3% of the parameters.

While these numbers tell how many parameters are resolved by a certain piece of information, they do not tell which of the parameters are resolved. In many cases a common sense approach can be used. For instance, it is very likely that the main field baseline terms, whose epoch is 1980, are resolved by the Magsat data. The secular variation is resolved by the observatories and also by POGO when inside its mission envelope. The high degree lithospheric field is probably resolved mostly by Magsat, and the fields from coupling currents certainly are, though regularization is present. It is not so obvious, however, which data sets are resolving what parameters in the magnetospheric and ionospheric expansions. To address this, consider the resolution matrix from the j-th data subset, R_{d_j}. Its i-th row is the resolving kernel, or averaging function, for the expected value of that portion of the i-th estimated parameter, $E[\tilde{x}_i]$, attributable to the j-th data subset, denoted $E[\tilde{x}_{i,j}]$, over the true parameter space, $\underline{x}$. One can also construct resolving kernels for the expected value of that portion of some estimated quantity, $E[\tilde{z}]$, attributable to the j-th data subset, denoted $E[\tilde{z}_j]$, that is a linear functional, $\underline{f}_z$, of the parameters:

$$E[\tilde{z}_j] = E\left[\underline{f}_z^T \underline{\tilde{x}}_j\right] = \underline{f}_z^T E\left[\underline{\tilde{x}}_j\right] = \underline{f}_z^T R_{d_j} \underline{x} = \underline{r}_{z,j}^T \underline{x} \tag{133}$$

The $E[\tilde{z}_j]$ then gives a statistical measure of the contribution of the j-th data subset to $\tilde{z}$. Unfortunately, these cannot be directly compared since the true values, $\underline{x}$, are unknown, but one can establish upper-bounds on the contributions which can be compared:

$$\begin{aligned} |E[\tilde{z}_j]| &= |\underline{r}_{z,j}^T \underline{x}| && (134) \\ &\leq |\underline{r}_{z,j}|\,|\underline{x}| && (135) \\ \frac{|E[\tilde{z}_j]|}{|\underline{x}|} &\leq |\underline{r}_{z,j}| \equiv \rho_{z,j} && (136) \end{aligned}$$

If the Euclidean norm is used, then the $\rho_{z,j}$ factor gives a statistical upper-bound on the ratio of the absolute $\tilde{z}$ contribution from the j-th data subset to the length of $\underline{x}$. Although these upper-bounds are very loose, they may still help in determining which parameters are likely resolved by what data.

Rather than compute ρ factors for the real and imaginary parts of each parameter in the magnetospheric and ionospheric expansions, factors were instead computed for the amplitude of the complex parameters propagated to March 21 and June 21, 1980 for the observatories, Magsat, and POGO. These are shown in Fig. 13. These seasons were chosen because their Magsat data concentrations vary so significantly, and a single year was chosen because both fields have a 12 mo periodicity, when excluding $F_{10.7}$ and D_{st} effects. The propagations (linear functionals) eliminate the need to show s explicitly. The factor for the amplitude of a complex coefficient, $\rho_{|z|}$, is related to the factors for its real, $\rho_{\Re[z]}$, and imaginary, $\rho_{\Im[z]}$, parts as:

$$\rho_{|z|} = \sqrt{\rho_{\Re[z]}^2 + \rho_{\Im[z]}^2} \tag{137}$$

The top panel shows the results for the ionosphere. The upper-bounds for the Magsat data consistently dwarf those of the observatories and POGO across all parameters and both seasons. The bounds diminish with increasing k for fixed p and l for all three subsets. Although there appears to be no significant variation between pl-brackets, there is a slight decease in baseline of the bounds with increasing l. This behavior with k is probably related to the influence of the $\mathcal{Q}_{|\nabla_s^2 \underline{J}_{eq,p>0}|}$ norm, which generally increases with k. The bottom panel shows the results for the magnetosphere. Here, the effects of the D_{st} dependence are accounted for by using its value at midnight on the given days. Again, the upper-bounds for the Magsat data are orders of magnitude larger than those of the observatories and POGO, and again, there is a general decrease in bounds with increasing k, probably a result of $\mathcal{Q}_{|\Delta \underline{B}_{ltd}|}$. The effects of the higher D_{st} level on June 12 can also be seen in the $k = 1$ factors. There also appears to be a strong peak at $k = l = p = 1$ across both ionospheric and magnetospheric profiles at both seasons. This is probably related to the correlation between these parameters which still remains in the CMP3 model, and may be illustrating a "smearing" of the resolving kernels for those parameters. Although it is plausible that Magsat could have a higher potential influence on these fields than both

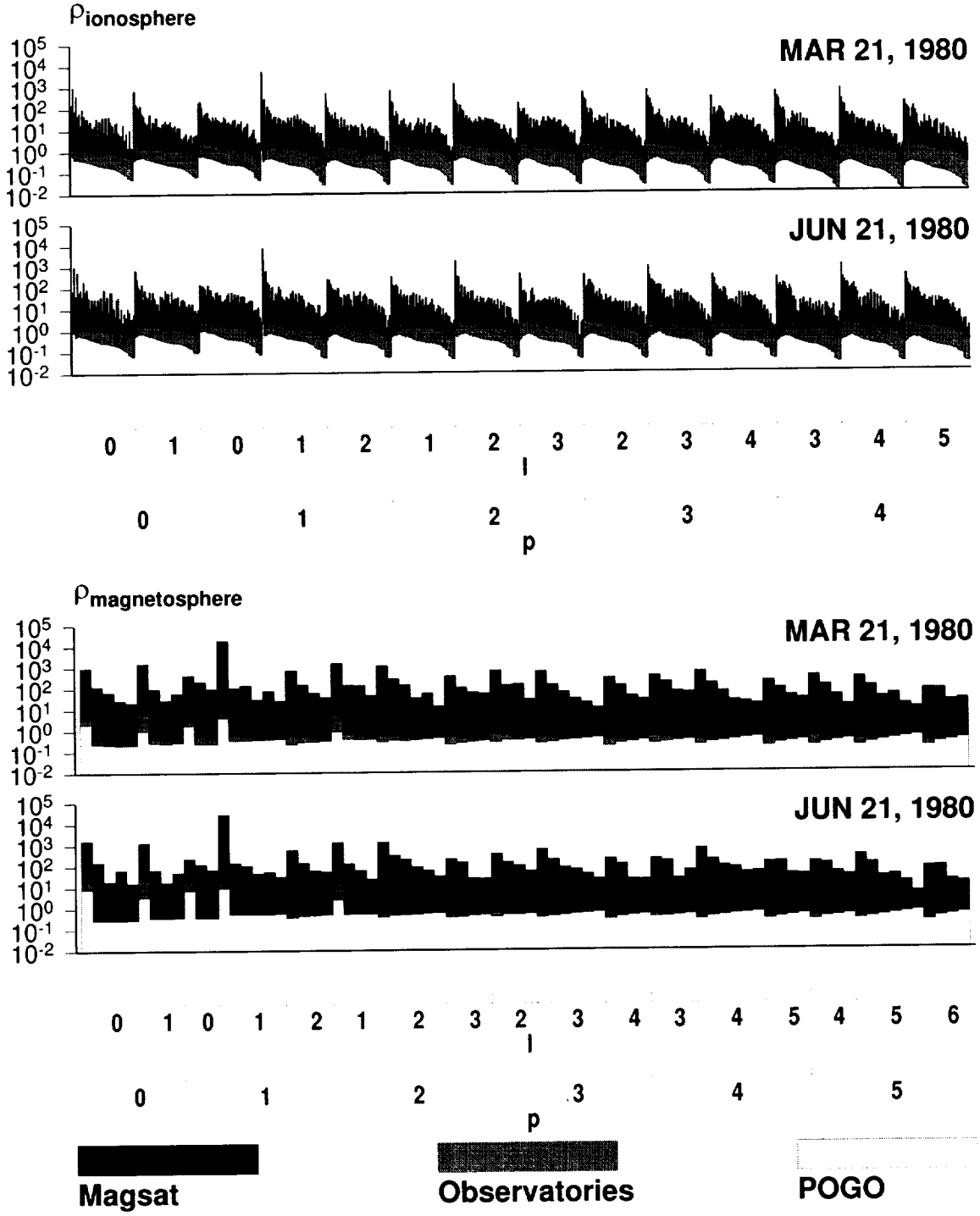

Figure 13: The "ρ factors" for the ionospheric parameter amplitudes $|\bar{\varepsilon}^l_{kp}|$ and magnetospheric parameter amplitudes $|\mu^l_{kp}|$ on March 21 and June 21, 1980 for Magsat, POGO, and the observatory hourly means. The k index increases linearly to the right over the appropriate range within the p and l bracket. The ρ for $|\mu^l_{kp}|$ also includes the effects of D_{st} activity at midnight for the given days, being 5 nT and 13 nT for March 21 and June 21, respectively.

observatories and POGO, differences of several orders of magnitude in the "ρ factor" upper-bounds is surprising, but may be explainable by some sort of "smearing" mechanism.

Returning to Table 3, the last column lists the data and prior misfit factors. As discussed in Section 4.2, these are measures of the consistency between the predicted and actual errors of the model, and give an indication as to how the relative importance of the terms in $\mathcal{L}(\underline{x})$ should be adjusted to attain this consistency. These factors are of course not independent and the adjustment of one will affect the others in complicated ways (see *Seber and Wild* [1989] for discussions on the related topic of iteratively reweighted least-squares (IRLS)). However, values of $s^2_{d_i}$ or $s^2_{a_i}$ above (below) unity would suggest a relative decrease (increase) in influence is warranted for the information from that data subset or norm. Hence, the data misfits show that the mid/low dipole latitude observatory hourly means subset is about right, the observatory annual means and both POGO subsets are too zealous, and the others are too meek. This may be partly due to substantial outliers in the annual means and POGO pass subsets that must be down-weighted. Meanwhile, the prior misfits reveal aggressive damping on all but the $\mathcal{Q}_{|\nabla^2_s \underline{J}_{eq,p>0}|}$ norm, which is evidently under damped. Given that it is difficult to make definitive statements about the effects of changing damping parameters, perhaps the fact that the $\mathcal{Q}_{|\underline{J}_{eq}|}$ misfit is over 2.5 times and $\mathcal{Q}_{|\Delta \underline{B}_{ltd}|}$ is over 24 times larger than their optimal values suggests that their level of damping should be decreased, though the latter is smoothing terms which are considered, as a whole, minor. Finally, the misfit over all data subsets, s^2, is 0.89. This suggests that the data uncertainties, as well as the elements of the error covariance matrix, be reduced by 11% to achieve calibrated error estimates. Given the complexity of the CMP3 model, the *a priori* data weights, as a whole, are not considered far from optimal.

6 Discussion

In this section the examination of the CMP3 model moves to more physical grounds. The salient features of the model are compared with, and assessed in light of, other works and with the known physics of the near-Earth magnetic field.

6.1 Previous comprehensive models

Before a discussion of the various source fields is undertaken, it is instructive to compare the CMP3 model with its predecessors introduced in Section 1.3 in terms of residual statistics alone. As stated earlier, both GSFC(12/93) and GSFC(8/95-SqM) are based upon quiet time POGO, Magsat, and observatory hourly means data. Annual means data are also included. The GSFC(12/93) model incorporates two separate degree/order 13 main field spherical harmonic expansions, one for $1965 - 1970$ covering the POGO mission and one for $1979 - 1980$ covering the Magsat mission, but common magnetospheric and ionospheric expansions of degree/order 5 and degree 20/order 4, respectively. Furthermore, the longitudinal dependence of these latter expansions is in terms of the local time angle, and the magnetospheric expansion includes degree-one terms which are linearly dependent upon the D_{st} index in order to model ring-current variations. An associated induced field expansion of degree 20/order 4 was also estimated along with observatory vector biases for the combined hourly and annual means.

The GSFC(8/95-SqM) model uses the same continuous main field parameterization as CMP3. The magnetospheric field is the same as for GSFC(12/93), but now includes annual and semi-annual seasonal variations; the ionospheric and induced fields are also the same except that the expansions are now truncated at degree 8 and annual and semi-annual variations are present; and separate observatory biases are also estimated for the hourly and annual means.

A comparison of the unweighted residual statistics for these models, as well as for the GSFC/CU(12/96) model introduced in Section 4.5, is given in Table 4. Note that the data sets are only identical between CMP3 and GSFC/CU(12/96), otherwise the statistics are arranged by qualitatively similar groupings. The first things to notice are the large residual means and standard deviations for the observatory data with respect to the GSFC(12/93) model. These are a result of estimating a single set of vector biases for both hourly and annual means at a particular station, a practice discontinued in subsequent models. With the exception of mid/low dipole latitude Y between CMP3 and GSFC/CU(12/96), the σ_r for all components of the hourly means data decrease with increasing model sophistication.

This is not so, however, for the annual means data and is probably due to the fact that these data are down-weighted in CMP3 and GSFC/CU(12/96) relative to GSFC(8/95-SqM). The Magsat data sets also exhibit a decrease in σ_r as the models progress, even when considering the corrected versus uncorrected dusk data sets. For CMP3, the σ_r for the vector components of the mid/low latitude Magsat data are actually less than the 6 nT fluxgate accuracy quoted by *Langel and Hinze* [1998]. The σ_r for the larger of the two POGO data sets does not increase when progressing from GSFC(8/95-SqM) to CMP3, but increased slightly for the special whole pass data set when progressing from GSFC/CU(12/96) to CMP3. Overall, the CMP3 model is providing superior data fits to that of the other models, however, this is to be expected given the larger number of DOF's in this model.

6.2 Core and lithospheric fields

By virtue of their high quality measurements of Earth's magnetic field through time at fixed spatial locations, observatory time series are uniquely qualified to assess the validity of the main field secular variation. Recall from Section 5.1 that the predicted main field was in good agreement with the Y and Z components of the Tucson annual means (see Fig. 6) and the X and Y components of the Huancayo annual means (see Fig. 7). The agreement is actually good for all components for the vast majority of the annual means stations used in the model and this is taken to indicate that the main field secular variation is properly represented in CMP3.

While observatory time series can characterize the temporal variation of the field, the R_n spectrum of *Lowes* [1974] and *Mauersberger* [1956], which measures the mean-squared internal field magnitude over a sphere at a particular epoch per spherical harmonic degree, can provide information on the spatial character of the model. The spectrum for CMP3, computed at $r = 6371.2$ km and epoch 1980, shows the expected distinct change in slope of $\ln(R_n)$ around $n = 14$ where core gives way to crustal domination, as noted by *Langel and Estes* [1982]. However, there also appears to be a distinct noise "floor" emerging prior to $n = 50$. This type of behavior is also reported in the spectrum of the M07AV6 model of *Cain et al.* [1989b]. This suggests at least three spectral regimes: a low-degree core dominated, a mid-degree crustal dominated, and a high-degree noise dominated. Since the assignment of boundaries between the regimes can be somewhat subjective, especially when done visually, a more objective approach was developed in which a three-segment best fit linear piecewise regression (BFLPR) to unweighted $\ln(R_n)$ (excluding $\ln(R_1)$) was performed as a function of degree partitioning, i.e. the degree boundaries were chosen which minimized the total misfit. The resulting BFLPR is:

$$\ln(R_n) = \begin{cases} (-1.27 \pm 0.07) \cdot n + (20.8 \pm 0.7) & \text{for } n = 2 - 14; \\ (\ 0.05 \pm 0.02) \cdot n + (\ 1.7 \pm 0.7) & \text{for } n = 15 - 42; \\ (\ 0.11 \pm 0.03) \cdot n - (\ 0.7 \pm 1.7) & \text{for } n = 43 - 65; \end{cases} \tag{138}$$

and is shown along with the raw R_n values in the top panel of Fig. 14. Points of intersection between regressions for core and crustal, core and noise, and crustal and noise dominated regimes occur at $n = 14.5$, $n = 15.6$, and $n = 42.4$, respectively, as compared to the core and crustal value of $n = 14.2$ given by *Cain et al.* [1989b]. Under the assumptions of optimal (Wiener) filtering [*Press et al.*, 1992], the noise spectrum is considered uncorrelated with that of the core and the crust and is hypothesized to follow the same trend at lower degrees as established at higher degrees. The bottom panel of Fig. 14 shows the BFLPR, over the same core and crustal dominated regimes of the top panel, to $\ln(R_n)$ after subtraction from R_n of noise values extrapolated from the linear regression for the high-degree spectrum, and is given by:

$$\ln(R_n) = \begin{cases} (-1.27 \ \pm 0.07\ ) \cdot n + (20.8 \pm 0.7) & \text{for } n = 2 - 14; \\ (-0.016 \pm 0.023) \cdot n + (\ 2.8 \pm 0.7) & \text{for } n = 15 - 42. \end{cases} \tag{139}$$

While the noise correction has had a negligible affect on the core dominated spectrum, it has removed practically all of the slope in the linear regression for the crustal dominated portion, rendering it nearly level. The radius, R', at which the spectra become level may be an indication of the maximum depth of the current source layers associated with that part of the magnetic field, and for a power law of the form $R_n = c \cdot (d)^n$ at radius R it can be shown that [*Cain et al.*, 1989b]:

$$R' = R\sqrt{d} \tag{140}$$

where $\ln(d)$ is the slope of the linear regression. Applying this to the corrected core spectrum yields a leveling depth of 107 ± 125 km below the seismic core-mantle boundary (CMB) at $r = 3485$ km. This falls generally in between

Table 4: Comparison of unweighted residual statistics (μ_r and σ_r in units of nT).

Component	CMP3			GSFC/CU(12/96)		GSFC(8/95-SqM)			GSFC(12/93)		
	Number	μ_r	σ_r	μ_r	σ_r	Number	μ_r	σ_r	Number	μ_r	σ_r
Observatory annual-means (Magsat epoch)											
X	—	—	—	—	—	—	—	—	932	7.8	228.5
Y	—	—	—	—	—	—	—	—	932	16.4	202.4
Z	—	—	—	—	—	—	—	—	932	28.4	413.8
Observatory annual-means (POGO epoch)											
X	—	—	—	—	—	—	—	—	1901	11.7	232.3
Y	—	—	—	—	—	—	—	—	1901	31.7	300.2
Z	—	—	—	—	—	—	—	—	1901	28.8	397.8
Observatory annual-means											
X	4047	0.0	29.7	0.0	28.5	4048	0.0	26.0	—	—	—
Y	4047	0.0	44.3	0.0	40.1	4048	0.0	26.0	—	—	—
Z	4047	0.0	37.4	0.0	33.7	4048	0.0	31.9	—	—	—
Observatory hourly-means (Magsat epoch)											
X	—	—	—	—	—	—	—	—	25200	7.6	57.5
Y	—	—	—	—	—	—	—	—	25200	1.5	58.9
Z	—	—	—	—	—	—	—	—	25200	-0.8	48.9
Observatory hourly-means (POGO epoch)											
X	—	—	—	—	—	—	—	—	250488	-1.0	22.3
Y	—	—	—	—	—	—	—	—	250488	-0.4	21.8
Z	—	—	—	—	—	—	—	—	250488	-0.2	26.8
Observatory hourly-means											
$\lvert 90^\circ - \theta_d \rvert < 50^\circ$											
X	56963	0.0	10.1	0.0	11.4	153544	0.0	14.8	—	—	—
Y	57016	0.0	12.8	0.0	12.1	153544	0.0	14.2	—	—	—
Z	55978	0.0	9.1	0.0	10.2	153544	0.0	11.1	—	—	—
$\lvert 90^\circ - \theta_d \rvert \geq 50^\circ$											
X	65451	0.0	17.0	0.0	17.9	74712	0.0	19.4	—	—	—
Y	65487	0.0	15.5	0.0	17.6	74712	0.0	17.5	—	—	—
Z	65230	0.0	19.9	0.0	20.8	74712	0.0	22.4	—	—	—
Magsat corrected dusk											
X	—	—	—	—	—	11060	0.3	10.3	11060	1.2	11.4
Y	—	—	—	—	—	11060	0.3	13.4	11060	1.4	14.7
Z	—	—	—	—	—	11060	0.3	8.2	11060	-0.2	10.7
B	—	—	—	—	—	12399	-0.3	7.5	12399	-0.2	9.3
Magsat dusk											
X	9381	-0.04	4.6	-0.04	5.3	—	—	—	—	—	—
Y	9321	-0.03	5.8	0.0	6.8	—	—	—	—	—	—
Z	9382	0.2	4.4	0.1	5.4	—	—	—	—	—	—
B	11404	0.5	3.7	1.04	5.5	—	—	—	—	—	—
Magsat polar dusk											
X	7985	-1.8	15.8	-2.5	17.6	—	—	—	—	—	—
Y	7988	0.3	16.5	1.0	17.6	—	—	—	—	—	—
Magsat dawn											
X	10570	0.2	4.4	-0.3	5.1	10595	-0.4	7.1	10595	-0.6	8.4
Y	10537	-0.002	4.6	-0.1	5.2	10595	-0.1	7.4	10595	-0.4	9.6
Z	10588	-1.9	3.8	-0.8	4.7	10595	-0.2	6.2	10595	-0.1	9.2
B	12441	-0.1	3.6	-0.6	5.2	12460	-0.6	7.4	12460	-0.1	9.7
Magsat polar dawn											
X	8483	-0.6	17.4	-1.3	18.3	—	—	—	—	—	—
Y	8445	0.1	18.2	-1.8	19.4	—	—	—	—	—	—
POGO original											
B	—	—	—	—	—	57434	-2.0	8.0	172300	0.1	5.7
POGO decimated											
B	22685	-0.2	5.1	0.0	5.1	—	—	—	—	—	—
POGO pass											
B	6754	-0.05	6.7	0.0	6.4	—	—	—	—	—	—

the values of 174 km given by *Langel and Estes* [1982] and 80 ± 46 km given by *Cain et al.* [1989b], although the unweighted error envelope encompasses these values as well as several km above the CMB. The leveling depth for the crustal spectrum is 50 ± 74 km below Earth's surface, where the *Cain et al.* [1989b] value is 21 km, and though this may be a satisfying result in and of itself, it should not be taken out of context given the overly simplifying assumptions that have been made. There is evidence from the statistical models of crustal magnetization of *Jackson* [1994] that the crustal power may be increasing with degree over this range and only at higher degrees ($n = 200$) does it begin to fall off. For comparative purposes, however, these exercises show that the R_n spectrum of CMP3 is in good agreement with previous work.

In light of the discussion on R_n, the lithospherically dominated portion of the internal field model is taken to be $n = 15-42$ and inspection of global maps of B_r for $n > 42$ confirms that noise and external field contamination begin to dominate in that range. Therefore, the nominal lithospheric B_r map from CMP3 reflecting degrees $n = 15 - 42$ is shown in Fig. 15. The ΔZ (or $-\Delta B_r$) map for $n = 15 - 65$ of *Ravat et al.* [1995], henceforth referred to as the RLPAA map, will be the standard by which the CMP3 lithospheric field will be compared. It is derived from Magsat data using various data processing techniques as well as techniques for modeling and removing ionospheric fields, and a covariant spherical harmonic analysis procedure to isolate common dawn and dusk lithospheric anomaly features. The first point to make is that both maps are in excellent agreement with regards to the shapes and locations of the major well-known anomalies such as Kiruna (A), Kursk (B), Bangui (C), Gulf of Mexico (D), Kentucky (E), Australian Bight (F), etc. (where the letter identifies the corresponding anomaly in Fig. 15), however, the CMP3 anomalies in many instances appear to have larger magnitudes, as much as $30 - 50\%$ in some cases. This may be an effect of applying Kaiser filtering [*Kaiser*, 1974] with a cutoff of 12000 km to equatorial/mid latitude Magsat vector data used in deriving RLPAA, resulting in diminished amplitudes. Another effect of this type of along-track filtering, in the case of Magsat, is the removal of generally north-south trending anomaly features. Some evidence of this may be seen, for instance, when comparing the maps in the eastern Australian basin region (G) (see *Purucker et al.* [1997]) and the region of the Izu-Bonin subduction zone (H) (30°N, 140°E). Other CMP3 north-south lineations, such as those in the South American mid-continent region just south of the dip equator (I), do not appear to be of lithospheric origin, but rather are manifestations of external field contamination. There is also a very conspicuous feature centered near 55°N, 90°E in northern Siberia (J) on the CMP3 map interpreted to be an artifact of poor data control due to the fact that gaps exist in the selected Magsat dawn and dusk pass coverage in that area.

To facilitate the comparison at high latitudes, polar maps above 60°N and below 60°S of the nominal lithospheric B_r are shown in Fig. 16. Because the RLPAA map is derived from Magsat data alone, it is not considered valid above about 83°N or below about 83°S. However, within the region of plausibility, the RLPAA and CMP3 maps agree very well in general shape and location of the major known anomalies. Again, the anomaly intensities run generally higher for the CMP3 maps. There are a couple of notable differences, such as the slight shift of the northern Greenland anomaly (K) (where the letter identifies the corresponding anomaly in Fig. 16) from a position on the northwest coast in RLPAA to a more north-central position in CMP3, and the emergence of a significant negative anomaly centered over the south magnetic dipole position (L) (79°S, 109°E) in CMP3 that is absent in RLPAA. The polar maps also reveal quite a lot of structure in the CMP3 lithospheric model that lies near the geographic poles, outside the region of Magsat data coverage. Recall that CMP3 includes data from the POGO satellites OGO-2, OGO-4, and OGO-6, whose orbit inclinations were 87.3°, 86.0°, and 82.0°, respectively. Thus, the gap in polar coverage for CMP3 has been reduced to caps of half-angle of about 3°. A better standard for comparison in these regions is therefore the POGO-derived anomaly maps of *Langel* [1990]. Since these are maps of scalar anomalies reduced to pole, they should be very close to ΔZ and ΔB_r near the north and south poles, respectively. The strong positive-negative anomaly pair entwined at the north pole (M) also appear on the POGO map, except here the intensities are stronger than can be accounted for by upward continuation to the 500 km level of the POGO maps. Near the south pole there is a strong negative lineation (N) that parallels the $135°-315°$ meridian and corresponds very well with the Trans-Antarctic mountain chain. This feature is diffuse and fragmented at best in the POGO map. Again, the strong negative anomaly over the south magnetic dipole (L) is missing in the POGO map. Finally, there is a new feature (O) in the CMP3 map located at about 86°S, 90°E which has the distinction of being the most instense of all anomalies in this degree range (almost 30 nT). While it has no counterpart in the POGO map, the CMP3 model does include POGO measurements over the bulk of this region. However, since the POGO data gap also transects this feature, an interpretation must be suspended until further analysis is done.

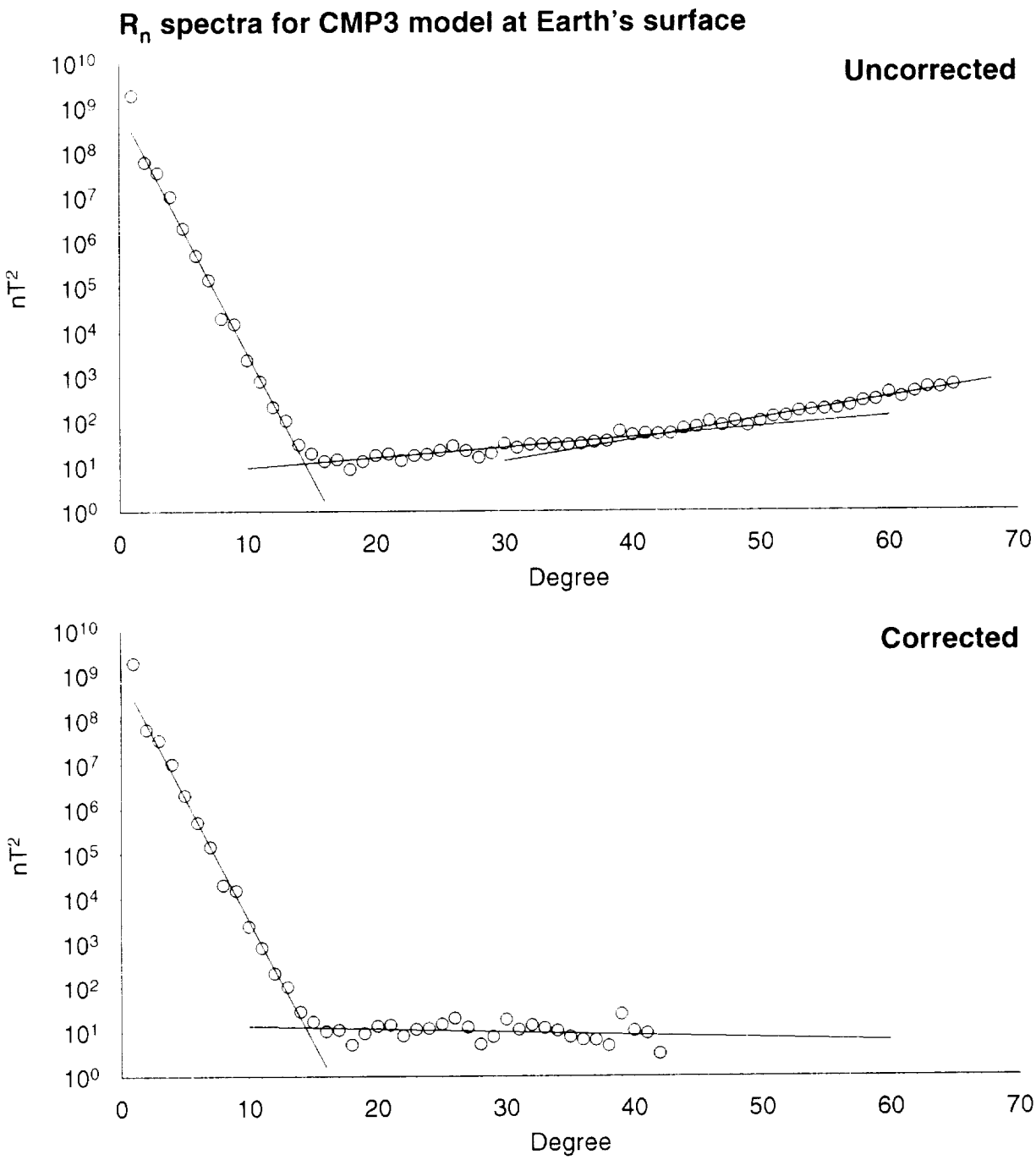

Figure 14: A comparison of R_n spectra for the CMP3 model at $r = 6371.2$ km for epoch 1980 corrected (bottom) and uncorrected (top) for high degree noise contamination. The solid lines in the uncorrected plot are the three best fit linear piecewise regressions (BFLPR) to $\ln(R_n)$ as a function of degree partitioning. The solid lines in the corrected plot are the BFLPR, over the same low and mid degree segments, to $\ln(R_n)$ after subtraction of values extrapolated from the linear regression for the high degree segment in the uncorrected spectrum.

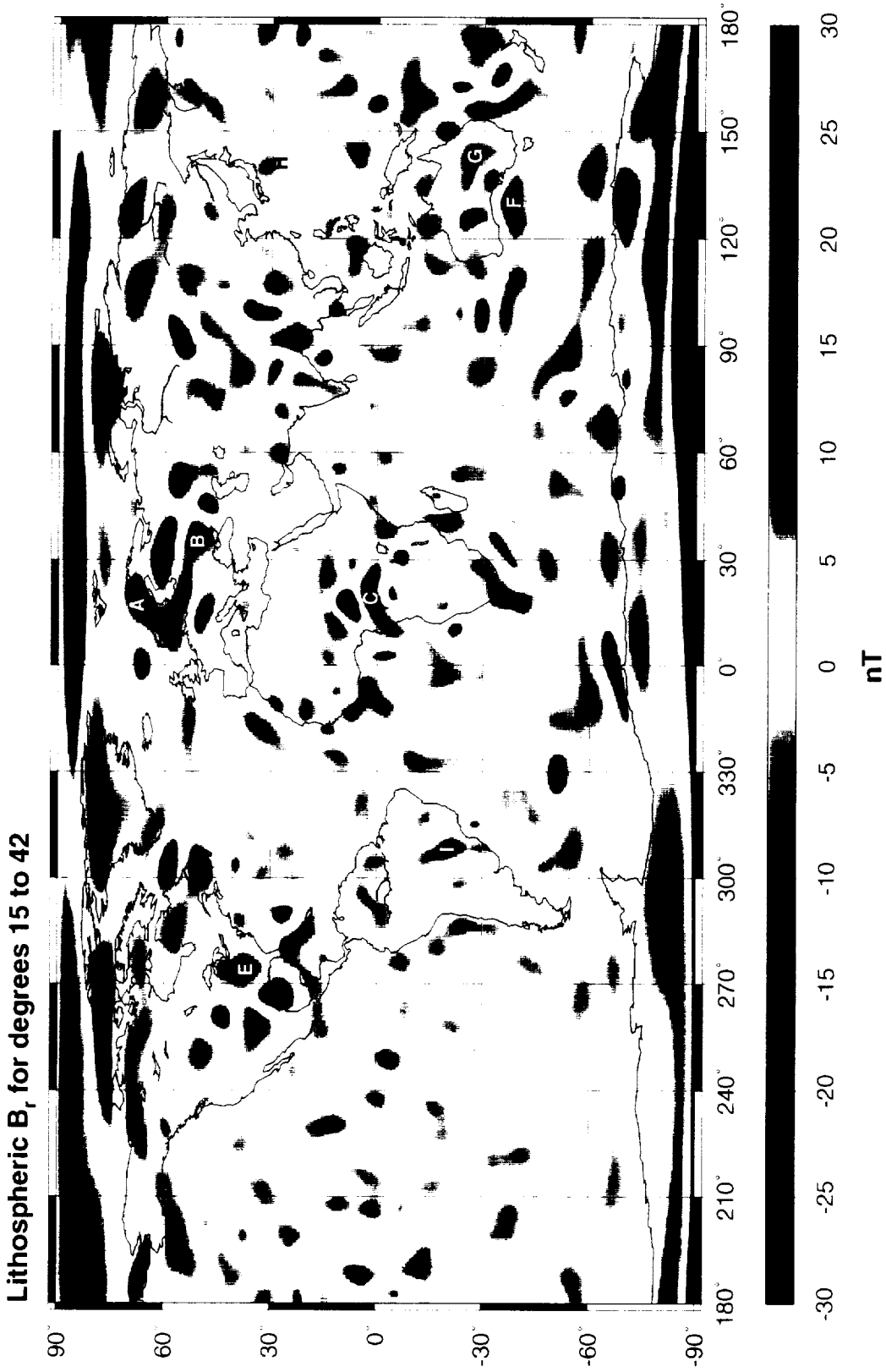

Figure 15: Global map of the CMP3 lithospheric contribution (degrees 15 to 42) to B_r on the sphere $r = 6771.2$ km (Cylindrical Equidistant projection). Letters identify particular anomalies referenced in the discussion.

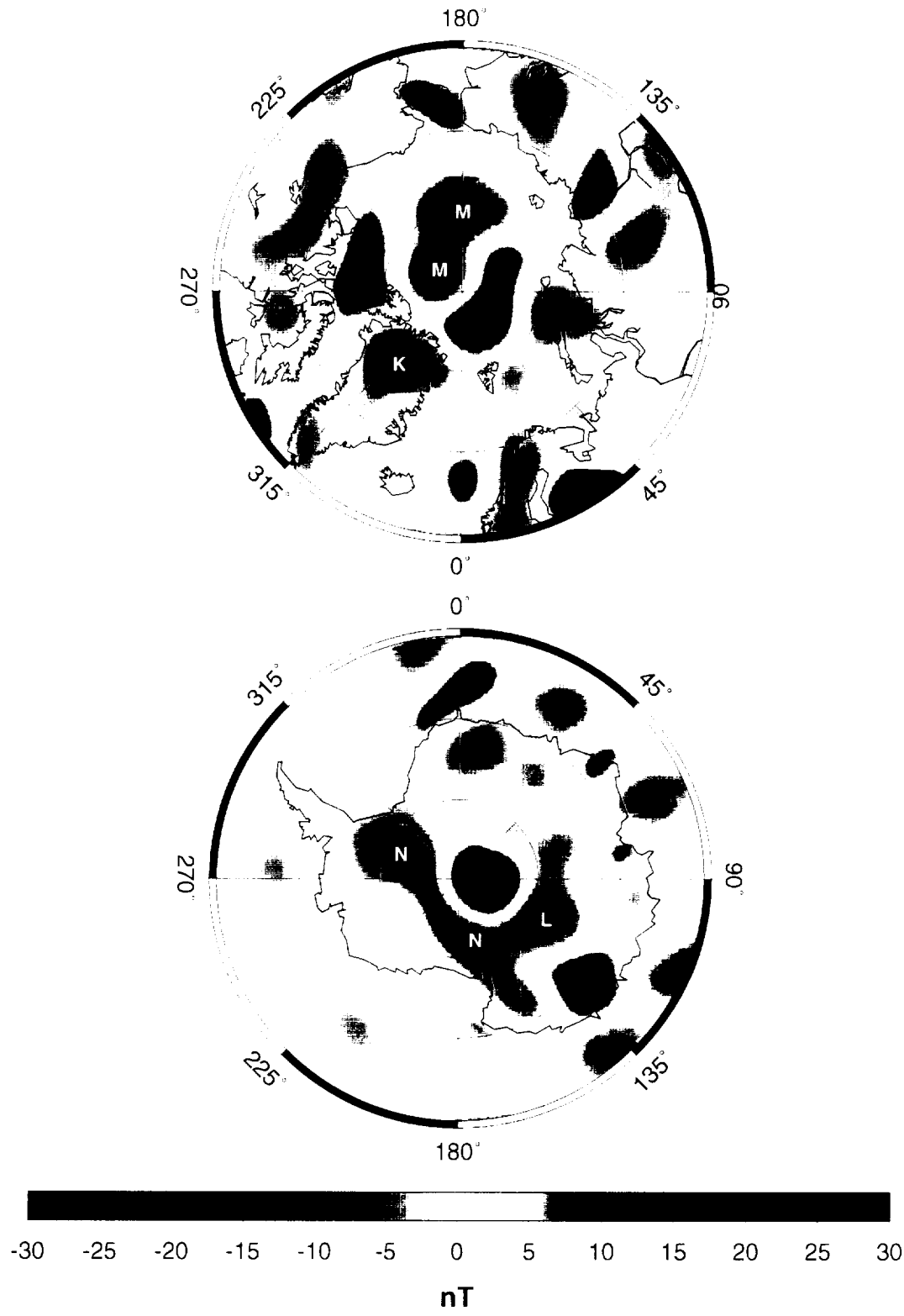

Figure 16: Polar maps above 60°N (top) and below 60°S (bottom) of the CMP3 lithospheric contribution (degrees 15 to 42) to B_r on the sphere $r = 6771.2$ km (Stereographic projections). Letters identify particular anomalies referenced in the discussion.

As alluded to earlier, the observatory vector biases are closely related to that portion of the crustal signal which resides above the truncation level of the internal field expansion. A listing of the CMP3 biases and their associated calibrated 1σ error is given in the tables of Appendix A for both the OHM and OAM. Of the 203 stations providing both hourly and annual means data, 1σ error envelopes of corresponding X, Y, and Z components of the hourly and annual means bias vectors overlapped in 180, 186, and 187 cases, respectively. Of the 30 assigned OHM station breaks, 1σ error envelopes of corresponding X, Y, and Z bias components of adjacent segments overlapped in 18, 19, and 23 cases, respectively, while of the 62 assigned OAM station breaks, the same counts were 13, 37, and 42, respectively. This means that the baselines of the hourly and annual means are statistically indistinguishable at the 1σ level for the majority of stations providing both. Likewise, more than half of the assigned hourly and annual means station breaks are not seen at the 1σ level. The implications are that perhaps a reduction in the model parameter space commensurate with these statistics be undertaken, although it is noted that these statistics depend upon the spatial and temporal structure of the basis functions and not the actual field values themselves.

6.3 Ionospheric field

The most dominant of the E-region ionospheric expansion coefficients are $\Re\{\tilde{z}^1_{2,0,1}\} = 2.8$ nT followed by $\Re\{\tilde{z}^2_{3,0,2}\} = -1.5$ nT. Both are magnetic local time terms ($l = p$) with no seasonal variation ($s = 0$) whose maximum amplitudes are centered at the sub-solar point (real parts) and contribute to the two major Sq foci of anti-polarity in the northern and southern hemispheres ($k = l = 1$). The first coefficient, however, describes the clear, regular diurnal variation ($p = 1$) of such a field through the course of a solar day, while the second imparts some semi-diurnal variation ($p = 2$) to this.

The influence of $\Re\{\tilde{z}^1_{2,0,1}\}$ can be seen in global maps of the E-region equivalent current function Ψ of Eq. 105. In Fig. 17, Ψ is shown at magnetic local noon on March 21, 1980, but for different values of MUT, thus allowing behavior with respect to universal time to be probed. A value of $F_{10.7} = 140.0 \cdot 10^{-22}\mathrm{W/m^2/Hz}$, an average over the time span of this model, was used to generate the maps. The dual Sq foci are indeed the major features, showing a slightly asymmetric current load (with respect to the roughly equal magnitude expected at equinox) flowing in oppositely directed vortices in the northern (counter-clockwise) and southern (clockwise) hemispheres in accordance with Eq. 104. The total current flowing in the northern (southern) vortex is the same (slightly lower) than that reported by *Malin and Gupta* [1977], who also included $p = 0$ terms. Besides these, there are several other items of interest: a significant decrease in $|\nabla\Psi|$ exists for much of the darkside hemisphere at all MUT, indicating that the $\mathcal{Q}_{|\underline{J}_i|}$ constraint is effective; the boundary between the two foci is coincident with the dip equator at all MUT, i.e. current flows tangent to the dip equator at and near local noon, thus affirming the utility of the QD constraints; there is also some amplitude and shape modulation with MUT that is beyond what is inherent in the QD constraints and which is attributable to non-local time variation; and there is a marked increase in $|\nabla\Psi|$ parallel to the dip equator at and near local noon for all MUT revealing an enhanced eastward current flow, which is in fact the EEJ.

In Fig. 18, Ψ is shown at noon magnetic local time in the center of the figure, but for the equinoxes and solstices of the various seasons, thus allowing behavior with respect to seasonal angle to be analyzed. A distinct seasonal variation is evident, as expected. Very clearly, the summer focus occurs at earlier local time than the winter focus, a known feature which persists at all MUT. Though not apparent in Fig. 18 at noon MUT, similar plots at midnight MUT show a minimum northern (southern) focal current intensity in December (June) and a maximum northern focal intensity in June, as expected, but a maximum southern focal intensity in September. This general peculiarity in focal intensity variation with season is likely attributable to the $\mathcal{Q}_{|\underline{J}_i|}$ constraint which imposes circuit closure on the dayside hemisphere and, together with the static ionospheric field, may very well be modifying the expected variation. Seasonal oscillations in Ψ focal intensities with respect to a preliminary CMP3 model including no $\mathcal{Q}_{|\underline{J}_i|}$ constraint are indeed of higher amplitude, confirming this idea.

The signatures of the current systems implied by Ψ can be seen in the ionospheric contributions to the vector components of Magsat dusk pass 263 in Figs. 9 and 10. If the foci were perfectly symmetric about the equator, and if the ascending pass of a satellite tracked directly over their centers, then X and Z would be even and odd functions of latitude, respectively, and Y would vanish. Specifically, as the satellite moved from the polar flank to center of the southern focus, X would rise from zero to its maximum and then fall to zero while Z would rise from its minimum,

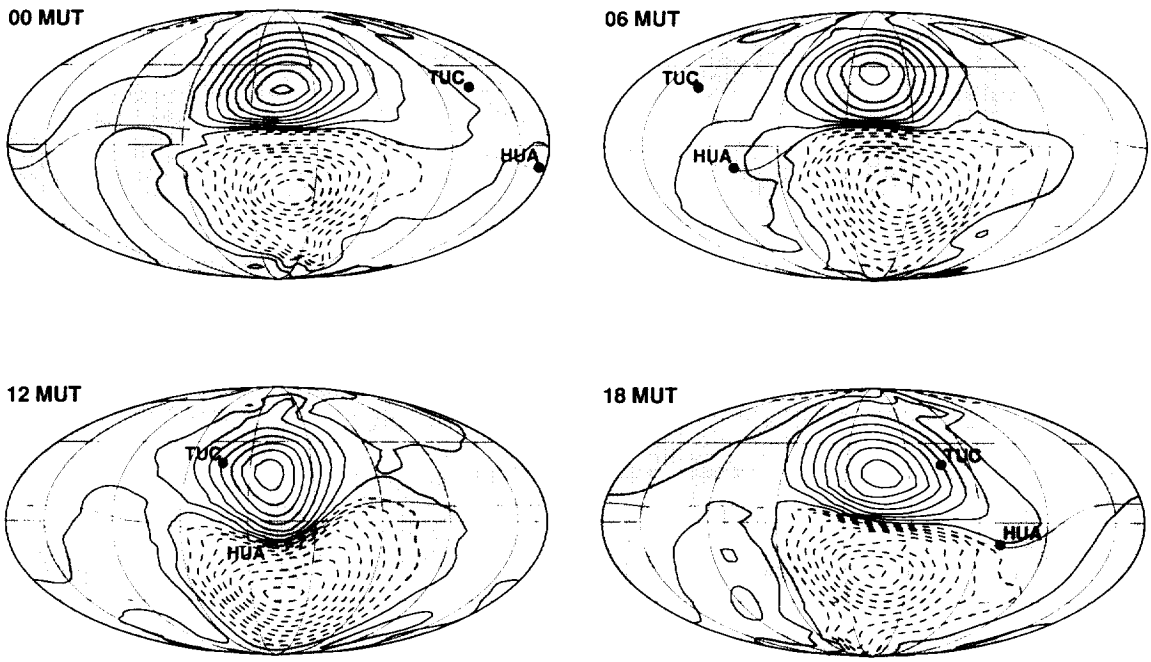

Figure 17: Global maps of ionospheric E-region equivalent current function Ψ for March 21, 1980 (Mollweide projection). A value of $F_{10.7} = 140.0 \cdot 10^{-22}\mathrm{W/m^2/Hz}$, an average over the time span of this model, was used to generate the maps. Recall from Eq. 105 that Ψ is defined on the sphere $r = 6481.2$ km. Each of the four panels is centered on noon magnetic local time, but for different magnetic universal times (MUT). The associated induced contribution is not included here. A 20 kA current flows between the contours. Locations of the Tucson (TUC) and Huancayo (HUA) observatories are shown.

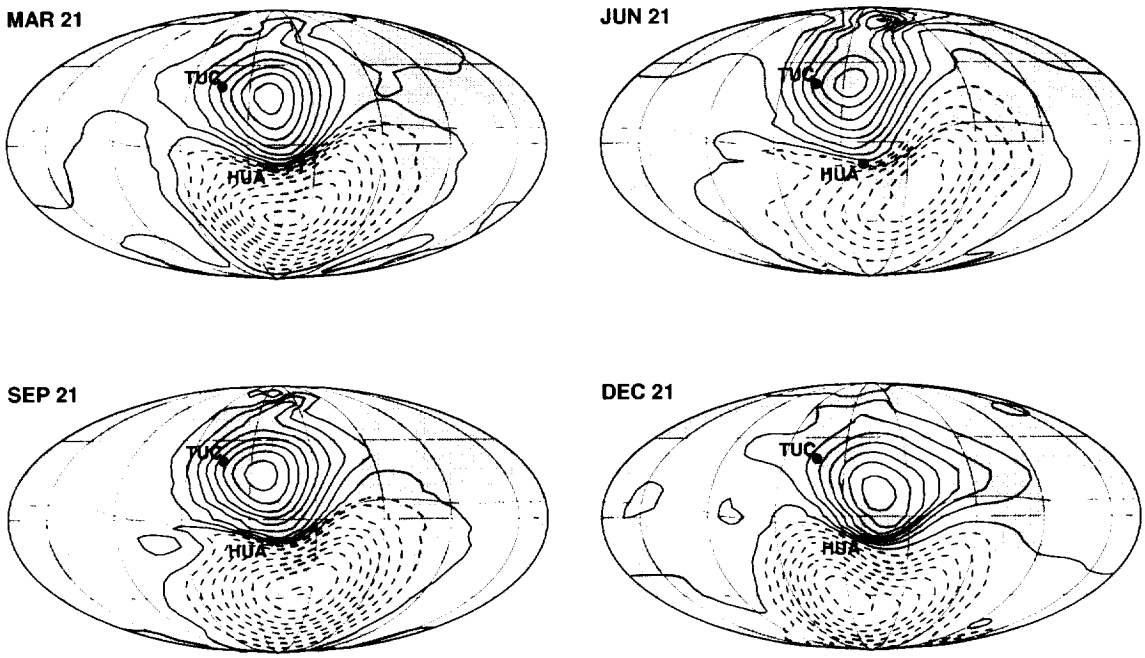

Figure 18: Global maps of ionospheric E-region equivalent current function Ψ defined on the sphere $r = 6481.2$ km (Mollweide projection). A value of $F_{10.7} = 140.0 \cdot 10^{-22}\mathrm{W/m^2/Hz}$, an average over the time span of this model, was used to generate the maps. Each of the four panels is centered on noon magnetic local and universal time, but for different seasons, i.e. December 21, 1979 and March 21, June 21, and September 21, 1980. The associated induced contribution is not included here. A 20 kA current flows between the contours. Locations of the Tucson (TUC) and Huancayo (HUA) observatories are shown.

Table 5: Magnetospheric annual variation (nT) from *Malin and Mete Isikara* [1976] compared to CMP3-type models.

	M&MI		CMP3		CNXS	
$c^l_{kp}(t)$	A	φ	A	φ	A	φ
$\Re\{\mu^0_{1,0}\}$	3.7	189°	2.7	231°	3.2	227°
$\Re\{\mu^0_{2,0}\}$	6.1	8°	0.1	343°	2.0	350°
$\Re\{\mu^1_{2,1}\}$	1.3	23°	0.04	56°	1.0	92°
$\Re\{\mu^0_{1,0}+\tilde{\varepsilon}^0_{1,0}\}$	—	—	2.4	228°	2.8	222°
$\Re\{\mu^0_{2,0}+\tilde{\varepsilon}^0_{2,0}\}$	—	—	0.9	348°	2.5	350°
$\Re\{\mu^1_{2,1}+\tilde{\varepsilon}^1_{2,1}\}$	—	—	0.1	321°	0.6	82°

through zero, to its maximum. Moving from the southern focal center to equator, X would fall to its minimum while Z would fall to zero. If the pass is off center towards dusk, then the symmetry of the X and Z signatures would be the same with smaller amplitudes, but Y would now be an odd function of latitude; falling from zero to its minimum, then rising to zero when moving from the polar flank to center of the southern focus, and then to the equator. This is indeed what is seen in the component plots, along with a possible accentuation of the X minimum over the dip equator from the dusk extent of the EEJ. The EEJ signature can also be clearly seen in the ionospheric contribution to the scalar intensity of the POGO pass in Fig. 8 at local noon over the dip equator.

Vector component plots of the hourly means measured at the Tucson (Fig. 6) and Huancayo (Fig. 7) observatories on the quietest day of each month over the course of a year also reveal something of the daily, seasonal, and spatial structure of the ionospheric field. Noting that the daily segments begin at 0 UT, it can be seen that Tucson X and Z both have a single negative spike at local noon while Y spikes positive just before and negative just after local noon. This agrees with the location of Tucson being below and just north of the northern focus of Ψ in Fig. 17. At Huancayo, X spikes strongly positive (the EEJ) and Z spikes negative at local noon, which agrees with its location below and perhaps slightly north of the dip equator as shown in Fig. 17. In addition, Tucson Y and Z and all Huancayo components indicate an intensification of the ionospheric contribution to the diurnal signal during their respective summers.

6.4 Magnetospheric field

As expected, the static term along the dipole axis, $\Re\{\mu^0_{1,0,0}\}$, is by far the most dominant in the magnetospheric expansion, having a value of 21.4 nT. The magnitudes of the annual and semi-annual variations along this axis are about 13% and 7% of the magnitude of the static value, respectively. Although the mean tilt of the non-D_{st} dependent magnetospheric dipole field over season is only about 2.9° towards magnetic local noon, i.e. $\Re\{\mu^1_{1,0,1}\} = 1.1$ nT, the seasonal fluctuation about this mean is much larger, being predominantly in the annual term, with peak tilt magnitude being 15.7° at the solstices, i.e. $|\Re\{\mu^1_{1,1,1}\} + \Re\{\mu^1_{1,-1,1}\}| = 4.9$ nT.

Given that the magnetospheric model is dominated by the first degree terms, nevertheless the higher degree terms make important contributions that reflect the geometry of the magnetosphere. Some of these terms have been detected in previous studies. *Malin and Mete Isikara* [1976] studied the annual variation of midnight values of observatory data and found contributions to $\mu^0_{1,1,0}$, $\mu^0_{2,1,0}$, and $\mu^1_{2,1,1}$ that they attributed to seasonal movement of the ring-current relative to the equatorial plane. Note that their analysis is unable to distinguish annual variation of the magnetospheric part (μ^l_{ksp}) from that of the ionospheric part ($\tilde{\varepsilon}^l_{ksp}$). If a particular coefficient, $c^l_{kp}(t)$, is Fourier analyzed for annual periodicity such that:

$$c^l_{kp}(t) = A\cos(\omega_s t - \varphi) \tag{141}$$

then Table 5 summarizes their results, denoted M&MI, and shows the comparable results from the CMP3 model and a preliminary CMP3-type model without $\mathcal{Q}_{|\Delta \underline{B}_{ltd}|}$ smoothing, denoted CNXS, both for magnetospheric terms alone and for the sum of magnetospheric and ionospheric terms of similar indices. Although there are differences in the spatial basis functions with similar k and l values for the magnetosphere and ionosphere, due to QD constraints, they are considered minor here. The three models are in fairly close agreement with regards to $\Re\{\mu^0_{1,0}\}$, with M&MI and

Table 6: Magnetospheric expansion terms (nT) from T87We [*Peredo et al.*, 1993] compared to CMP3-type models.

	μ^l_{kp}	Season	T87We ($K_p = 0$)		T87We ($K_p = 3$)		CMP3		CNXS	
Diurnal	$\mu^1_{1,1}$	December	2.99	180°	3.33	180°	3.93	183°	3.49	180°
		Equinox	0	—	0	—	0.70	57°	2.02	161°
	$\mu^1_{2,1}$	December	1.19	359°	2.28	359°	0.23	344°	1.44	359°
		Equinox	1.42	357°	2.72	357°	0.28	353°	3.11	2°
	$\mu^0_{1,1}$	December	1.34	181°	1.88	181°	0.10	318°	0.87	247°
		Equinox	0	—	0	—	0.16	103°	0.69	43°
Semi-diurnal	$\mu^2_{2,2}$	December	0.04	359°	0.06	359°	0.11	349°	0.48	317°
		Equinox	0	—	0	—	0.06	328°	2.50	355°
	$\mu^1_{1,2}$	December	0.83	181°	1.06	181°	0.09	168°	0.60	183°
		Equinox	0.70	174°	0.68	174°	0.09	238°	0.43	183°

CMP3 at the extremes. When the effects of $\Re\{\tilde{\varepsilon}^0_{1,0}\}$ are added in, the agreement with M&MI actually appears to degrade, especially with respect to the amplitude, A. For $\Re\{\mu^0_{2,0}\}$, neither of the CMP3-type models comes close to matching the amplitude of M&MI, even when ionospheric effects are added. However, the phases, φ, appear to be relatively close, within 25°. For $\Re\{\mu^1_{2,1}\}$, the CMP3 amplitude, with and without the ionospheric term, is much smaller than that of M&MI. The CNXS amplitude is much closer, however, though it degrades when ionospheric effects are taken into account. Clearly, the $\mathcal{Q}_{|\Delta \underline{B}_{itd}|}$ smoothing is damping much of the amplitude of the $k = 2$ terms in the CMP3 model, perhaps excessively if M&MI is correct. However, recall that significant correlations exist between the $k \geq 2$ terms of the magnetosphere and ionosphere in the CNXS model and that this is the motivation for applying $\mathcal{Q}_{|\Delta \underline{B}_{itd}|}$.

Olsen [1996] has investigated possible magnetospheric field contributions to daily magnetic field variations. He examined several semi-empirical models of the magnetospheric field, reporting primarily on results from *Tsyganenko* [1987, 1989] and in particular, the model designated T87We in *Peredo et al.* [1993]. A comparison of the amplitude and phase of the above coefficients from T87We, CMP3, and CNXS is given in Table 6. The agreement of both amplitude and phase of $\mu^1_{1,1}$ in December is considered very good across the models, with the CMP3 coefficient diminishing more readily towards the T87We value of zero at equinox. For $\mu^1_{1,1}$, CMP3 appears overdamped with respect to T87We while CNXS shows good agreement in all seasons. For $\mu^0_{1,1}$, CMP3 again appears overdamped while the CNXS amplitude is roughly half that of T87We in December, but has not decayed away at equinox. In the case of semi-diurnal variation, the $\mu^2_{2,2}$ coefficient of CMP3 appears to be in much closer agreement with that of T87We while the converse is true for $\mu^1_{1,2}$. Evidently, the CNXS model, on the whole, is in good agreement with T87We, but deviations from the local time tilted dipole may be overdamped in the CMP3 model.

A visual picture of the predicted near-Earth magnetospheric field is realized by the vectorgrams in Figs. 19 and 20 for 12 and 0 MUT, respectively, for December 21, March 21, and June 21, with $D_{st} = -2.5$ nT. The top panel shows a cross section of the vector field in the magnetic noon-midnight plane containing the main dipole axis. The bottom panel shows a cross section of the vector field in the magnetic local time equatorial plane. The circles indicate the trace of the mean radius of the Earth at $r = 6371.2$ km, and the perpendicular distance from these circles to the cross section edges is 450 km. Hence, most of the Magsat measurements reside within the cross section region. The seasonal variation in strength of the components along and perpendicular to the dipole axis can be clearly seen in the plots; it is minimal at the equinoxes and maximal at the solstices, particularly northern summer. Note how the magnetic local noon-midnight component dominates the dawn-dusk component at the solstices. While the tilt of the dipole is in the direction needed to maintain perpendicularity with the Earth-Sun line at the solstices, the angles are only about 12.1° and 9.6° for northern and southern summer, respectively, in contrast to the expected average tilt of 23.4°. This is very similar to the results of the GSFC(8/95-SqM) model of *Langel et al.* [1996]. In addition, there are perceptible second-order variations between the fields at the two MUT values due to non-local time terms, mostly in the dipole equatorial component. Remember, however, that these are damped by the $\mathcal{Q}_{|\Delta \underline{B}_{itd}|}$ smoothing.

The magnetospheric model predictions of the scalar intensity along the POGO pass shown in Fig. 8 and the vector components along the Magsat dusk pass 263 in Figs. 9 and 10 are clearly those of an axial dipole whose moment is aligned, on average, near perpendicular to the orbit normals of the satellites. Furthermore, the behavior of the model

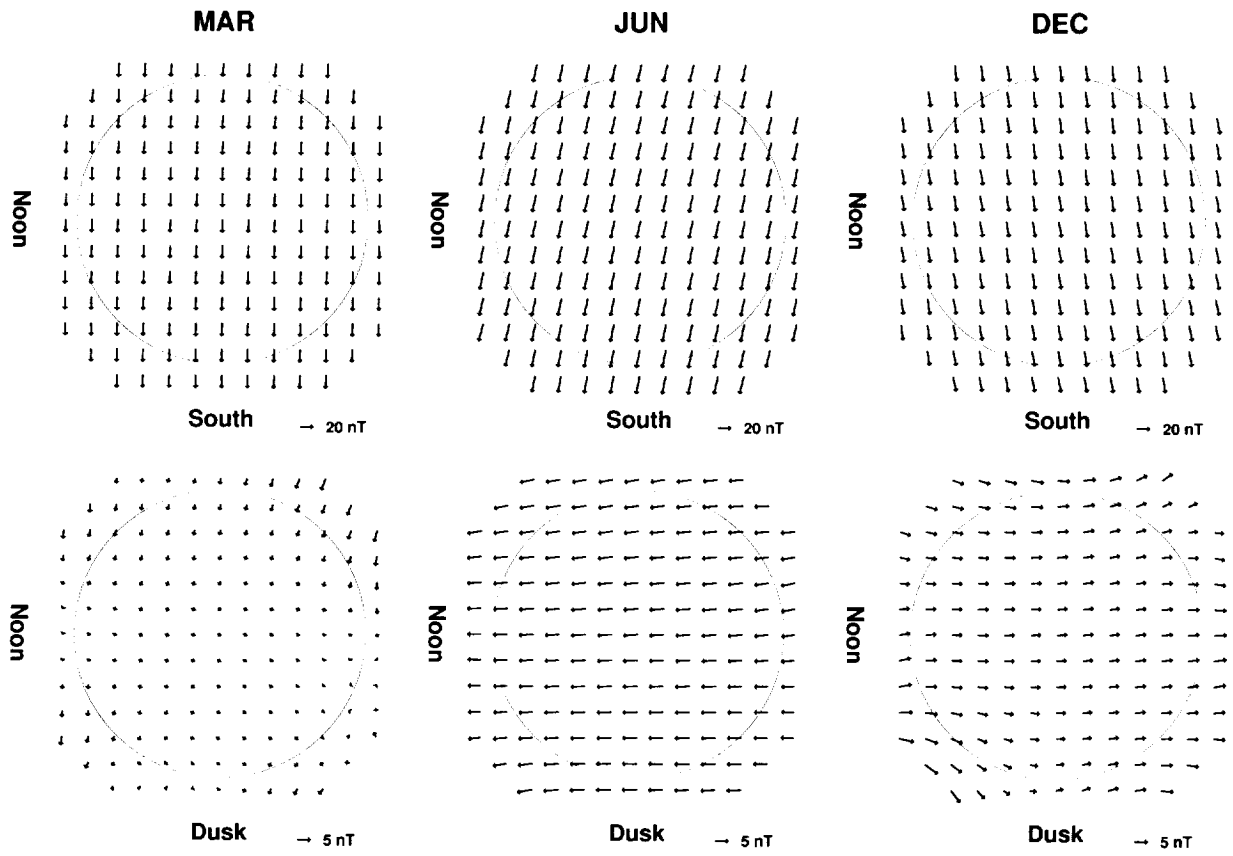

Figure 19: Near-Earth magnetospheric field at noon MUT for December 21, March 21, and June 21, with $D_{st} = -2.5$ nT. The top panel shows the component in the magnetic local noon-midnight meridian containing the main dipole axis. The bottom panel shows the component in the magnetic local time equatorial plane perpendicular to the main dipole axis. The circles show the location of the mean radius of the Earth, $r = 6371.2$ km, and the perpendicular distance from these circles to the top and bottom vector rows and the left and right vector columns is 450 km. Note the change in vector length scale between the top and bottom panels.

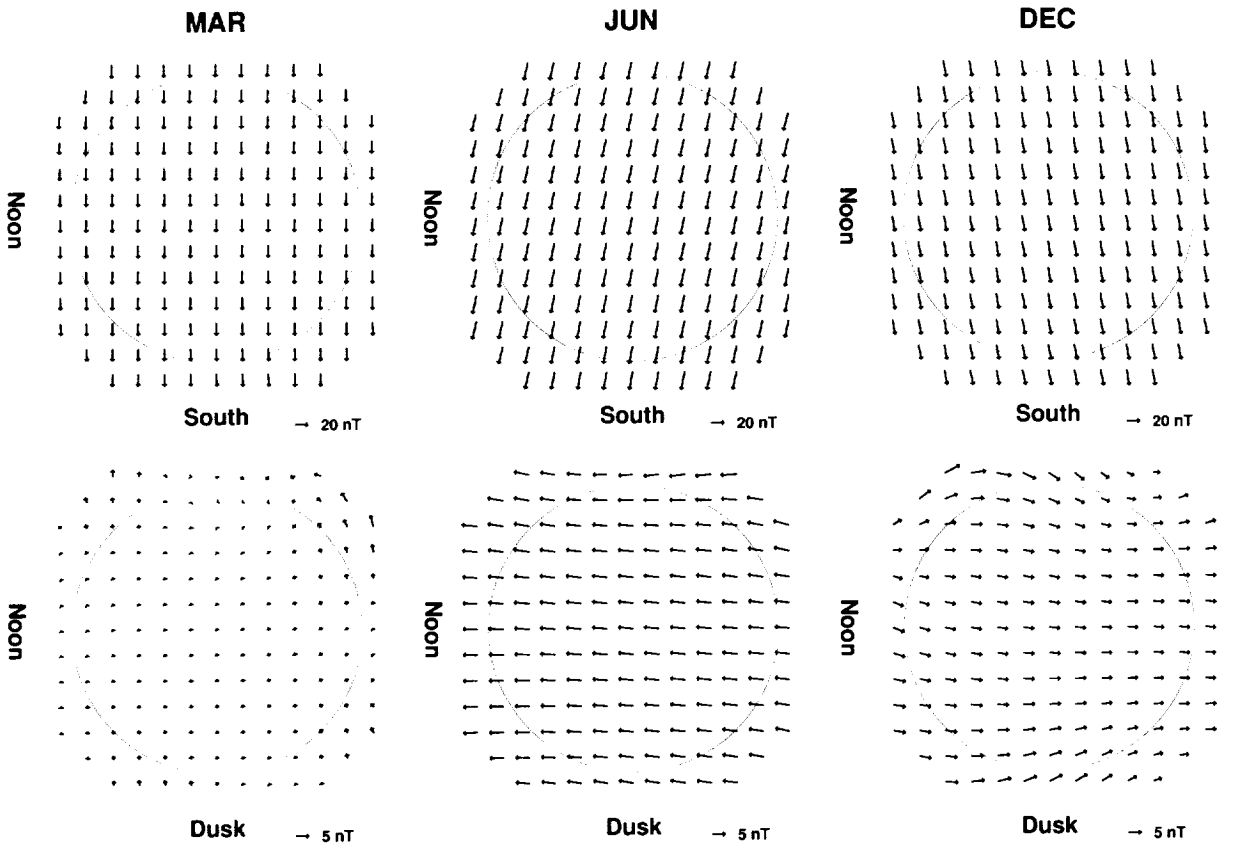

Figure 20: Near-Earth magnetospheric field at midnight MUT for December 21, March 21, and June 21, with $D_{st} = -2.5$ nT. The top panel shows the component in the magnetic local noon-midnight meridian containing the main dipole axis. The bottom panel shows the component in the magnetic local time equatorial plane perpendicular to the main dipole axis. The circles show the location of the mean radius of the Earth, $r = 6371.2$ km, and the perpendicular distance from these circles to the top and bottom vector rows and the left and right vector columns is 450 km. Note the change in vector length scale between the top and bottom panels.

as a function of the D_{st} index is illustrated in the X and Z components of Tucson in 1967 (see Fig. 6) where very large discontinuities are found in the magnetic records between the quietest days chosen for May and June. They are evidently the result of a ring-current adjustment, which is described quite well by D_{st}, and hence, the model fits them with little problem.

6.5 Fields from ionospheric coupling currents

The CMP3-derived radial current density (J_r) of the ionospheric coupling currents at dusk local time is shown in Fig. 21 for March and December 21. Note that this figure does not show the current density at any particular univeral time as a function of longitude, but rather, it shows the current density which is predicted to flow at different longitudes at dusk local time. As expected, the largest radial current flows at polar latitudes. During the morning (not shown), currents flow into the ionosphere ($J_r < 0$) at the poleward boundary of the polar oval (region 1 currents), and out of the ionosphere at the equatorial boundary (region 2 currents). During evening the current direction is reversed. The evening data also show upward currents at the dip equator and downward currents at nearby low latitudes. This is the radial component of the meridional current system of the equatorial electrojet, first observed in Magsat data by *Maeda et al.* [1982]. There is no evidence for such a current system in the morning sector.

A strong seasonal variation can be seen in J_r between March and December. During southern summer it is much more intense in the south polar oval region than in the north, while during equinox the intensities are more equal. In addition, the radial component of the meridional current system is better defined during equinox than during solstice. Although these findings are in keeping with those of *Olsen* [1997a], he finds current intensities which are in general significantly higher than those predicted by CMP3. This discrepancy, however, may be attributed to the difference in data selection: all days versus quiet days.

Olsen [1997a] has also detected larger scale upward currents in the north and downward currents in the south in the evening, and opposite this in the morning, for the December Magsat data. These are obscure in Fig. 21, if present at all. This may likely be due to the application of the $\mathcal{Q}_{\parallel J_r}$ smoother at both the dawn and dusk local times, and again to data selection. Such interhemispheric coupling currents are small or absent during the equinoxes and are expected to reverse during northern summer.

The toroidal field signature of the meridional current system may be clearly seen in the Y component of Magsat dusk pass 263 in Fig. 10. Because this pass occurs on Nov 19, 1979, near southern summer, the current density vortex just to the south of the dip equator is stronger than that just to the north, resulting in a stronger eastward and weaker westward field just south and north of the dip equator, respectively. The CMP3 model, in turn, predicts this asymmetry very well. The high amplitude excursions in the X and particularly the Y components at high latitudes are probably also of the field-aligned variety, however, these are also probably very transient in nature, and are thus fit very poorly by a model of this type which sees mean temporal and spatial field effects best.

7 Conclusions

The paradigm of comprehensive modeling is quite worthwhile, yet quite formidable. Progress is usually slow and incremental, and with new satellite missions and new technology on the horizon, a "final model" is simply an ideal to work towards. In this final section an attempt will be made to gauge the position of CMP3 and its methodology in the continuum of comprehensive modeling.

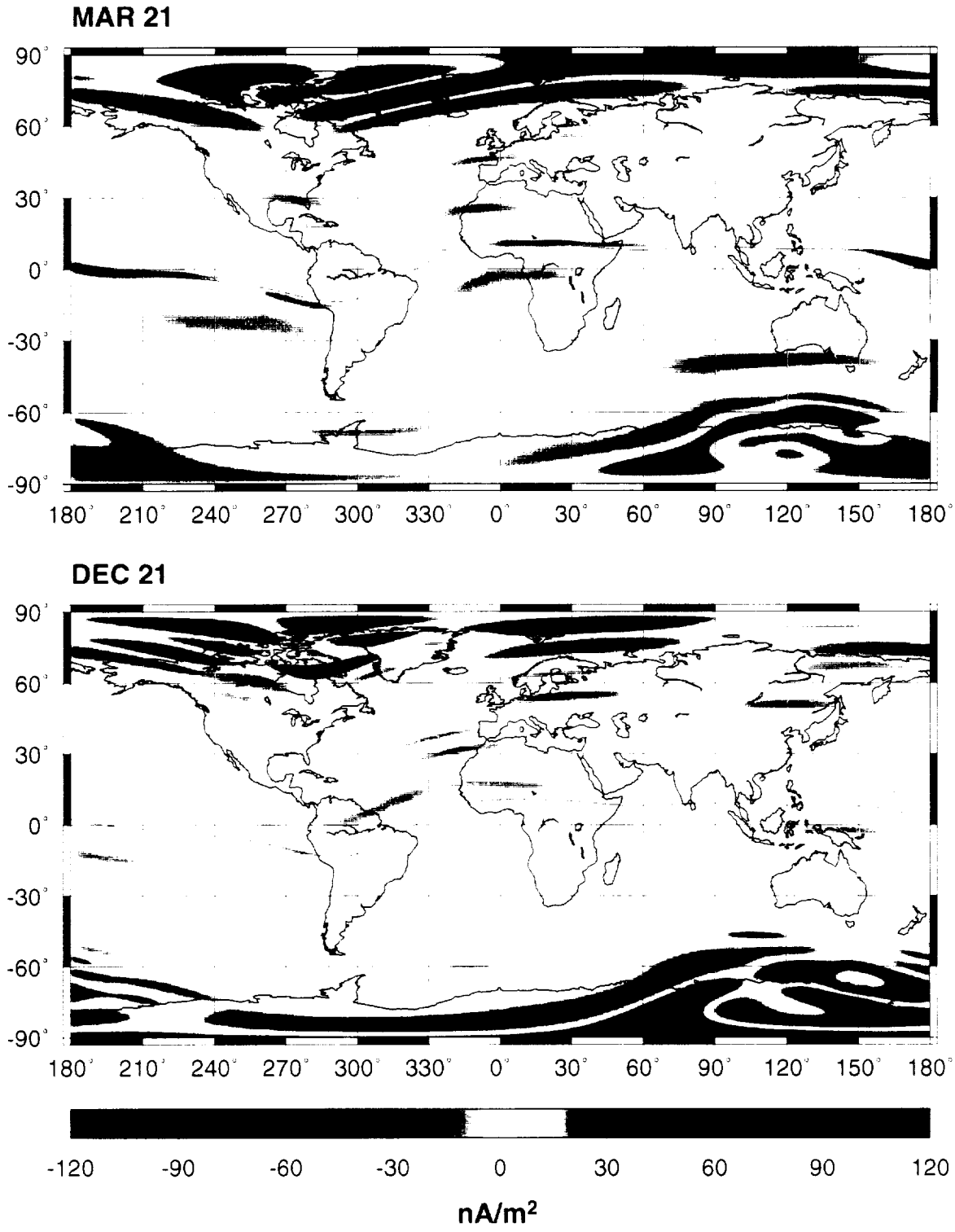

Figure 21: Global maps of the radial component of the ionospheric coupling currents at dusk on the sphere $r = 6821.2$ km (J_r in Eq. 125) for March 21 and December 21 (Cylindrical Equidistant projection).

7.1 New features

Perhaps the best and most obvious way to assess the progess made in the current phase is to simply compare it to the previous phase. Hence, features of the CMP3 model which are new with respect to the GSFC(8/95-SqM) model [*Langel et al.*, 1996] will be enumerated in this section.

The main field and attendant secular variation portions (triple summation in Eq. 6) of the models are identical, but CMP3 includes a static representation of the high degree lithospheric field (double summation in Eq. 6), which has successfully captured most of the known crustal anomaly fields seen at satellite altitude. Discrete point representations of the anomaly fields in the form of observatory biases are also provided by both models.

As for the ionosphere, the CMP3 parameterization has higher latitudinal resolution such as to fit the field of the EEJ. Both non-local time terms and QD constraints allow the CMP3 field to better respond to the ambient field, especially in terms of the conductivity distribution. Furthermore, the $Q_{|\underline{J}_{eq}|}$ constraint injects known physical limits on the conductivity patterns at night time. The GSFC(8/95-SqM) model includes no such features. Finally, rigid contraction and expansion of the ionospheric field in response to solar activity is also found in the CMP3 model, but not GSFC(8/95-SqM).

The magnetospheric field of CMP3 differs in two major ways from that of GSFC(8/95-SqM): first, it has the possibility of displaying smaller-scale features in both latitude and longitude; and second, it contains non-local time terms. Unfortunately, because of separability problems between the magnetospheric and ionospheric fields inherent in the data sets used, the full impact of these differences could not be explored. However, the CNXS model (no $Q_{|\Delta \underline{B}_{ltd}|}$ smoothing) does fit such data as the Y component of Magsat dawn significantly better ($\mu_r = 0.01$ nT, $\sigma_r = 4.3$ nT), which may indicate that this small-scale magnetospheric signal is present and worth pursuing.

Fields that are induced in the Earth from ionospheric and magnetospheric time-varying fields are included in both models. For GSFC(8/95-SqM), the field parameterization is explicit, that is, independent of that of the primary sources. For CMP3, the induced field parameterization is coupled with that of the primary sources through an *a priori* conductivity model. The reason for this is to reduce the size of the already large parameter set. Though the independent approach is inevitably of more interest, the coupled approach does allow for very complicated conductivity distributions to be included in the model, via the Q matrix of Eq. 16, with no additional parameters or computational cost.

The parameterization of fields from ionospheric coupling currents is completely absent in the GSFC(8/95-SqM) model. This is obviously a very significant part of the measured field for satellites moving through these current regions, as can be attested to by Y component plots of Magsat dusk data (e.g. Fig. 10). In addition, the CMP3 representation is fairly sophisticated in that it includes seasonal variation and a mechanism for conforming to the existing conductivity patterns through the use of QD constraints.

7.2 Future work

While the previous section discussed in some sense how far the comprehensive modeling effort has come, this section will hopefully give some clue as to how far it has to go, at least in the near-future. Future work falls into two major categories: first, that work which is truly new and never before tried; and second, that work which was, admittedly, not done quite right the first time around.

Much of the future work concerns data issues: The presence of the large, presumably spurious lithospheric anomaly centered near 55°N, 90°E in northern Siberia in Fig. 15 is most certainly an artifact of poor Magsat data coverage. The deviations of the predicted main field X component at Tucson and Z component at Huancayo from the annual means data outside the POGO and Magsat mission envelopes, shown in Figs. 6 and 7, respectively, are indications that substantial outliers may still exist in the observatory data sets. These instances both point to the need for better data selection in future models. On a more positive note, the anticipated inclusion of vector data from the Oersted satellite mission is expected to greatly enhance the validity of the models in local times other than dawn and dusk. Furthermore,

this data will aid in the separation of ionospheric and magnetospheric fields which has plagued the current study. One could also expand the scope of future models by considering measurements from more magnetically disturbed times.

As for parameterization issues, the list of future work items could be quite extensive, but a few that are possible in the near-future include: The proper handling of the annual means data which currently only affect the core and lithospheric parameters (see Eq. 86), but are assuredly functions of long-term variation in the external fields. The extension of the main field secular variation domain to Oersted epoch in order to include that data in a unified model. The inclusion of a J_θ component to the strictly radial coupling current density which is presently implemented, and if Oersted data is used, then move to a continuous diurnally-varying toroidal field rather than explicit dawn and dusk expansions. A proper treatment of the fields from the ionosphere and from associated coupling currents with respect to polar currents that are dependent upon the interplanetary magnetic field (IMF). Finally, the parameterization of the induced fields could be made independent again, or more complicated *a priori* conductivity models could be used.

Without question, the assignment of general weights (data uncertainties and constraint damping levels) in a model is of critical importance to its success, and models such as CMP3, which attempt to estimate a large number of parameters in an optimal fashion from imperfect data sets with the help of some hopefully judiciously placed constraints, are no exception. Though the assignment of data uncertainties followed a semi-quantitative procedure, as described in Section 4.4, the assignment of damping parameters for the constraints was largely subjective (based upon what was visually appealing). Yet, a systematic exploration of the weighted residual and error variance tradeoff surfaces in a 5-dimensional space seems a bit overwhelming. Hence, it would simplify modeling efforts to develop general weighting schemes and automate such searches.

7.3 Possible uses

The success of comprehensive modeling is in part driven by its utility to the scientific community. The method of coestimating fields from several sources and its affect on model consistency is of scientific interest in its own right; however, additional merit of the comprehensive models lies in their use as application tools, or reference models (if you will). Indeed, with the possible exception of the high degree lithospheric field where new, physically meaningful features might be found, most source fields are parameterized so as to model the well known, regular, quiet time features. Hence, comprehensive models are well qualified at removing known fields from the data so as to not obfuscate that which is unknown.

The CMP3 model may be regarded as a provider of field predictions from at least seven sources: the internal field, which is a superposition of fields from core and lithospheric sources; the ionospheric field from E-region currents and its associated induced counterpart; the magnetospheric field and its associated induced counterpart; and the field from ionospheric F-region coupling currents. In addition, there are discrete point models of the remaining lithospheric fields at the observatory locations in the form of vector biases. Though these models of the source fields may be considered reference fields, one must be cautious when applying them outside their scope, that is, extrapolating them to regimes which were not sampled by the data sets used in deriving them. For example, it is not recommended that the D_{st}-dependent portion of the magnetospheric field model be extrapolated much beyond the range of D_{st} found in the model data sets. However, the remaining portion may be valid over much longer time spans since it represents annual mean-field effects.

7.4 Availability

In accordance with the previous section, a forward modeling code is available which predicts the various CMP3 source fields given spatial and temporal positions and D_{st} and $F_{10.7}$ values. This code is in the form of an ANSI standard Fortran subroutine called CMP3FIELD. It returns the local (North, East, Down) components of $\underline{B}$ in nT on a sphere or on the IAU1966 ellipsoid from internal, primary and induced ionospheric, primary and induced magnetospheric, and dawn or dusk coupling current field sources. Two evaluations of the internal field are accommodated per two given spherical harmonic degree ranges. This is helpful when separate predictions are desired from the core dominated

and lithosphere dominated portions of the expansion. The CMP3 model information is input to the CMP3FIELD subroutine on the initial call from a sequentially accessed ASCII file. Both the forward code file and the CMP3 model information file are available from the authors by request.

Acknowledgments. We would like to thank Art Richmond at HAO/NCAR for his expertise in several external field related issues and for help with the initial stages of the manuscript. We also thank Mike Purucker at NASA/GSFC for his critique of the lithospheric field portions of the manuscript, as well as Herb Frey, Coerte Voorhies, and Pat Taylor, all at NASA/GSFC, for their careful reviews of the entire manuscript. TJS was supported under NASA Contract NAS5-31760.

References

Arkani-Hamed, J., and D.W. Strangway, 1985a. Intermediate-scale magnetic anomalies of the Earth, *Geophys., 50*, 2817-2830.

Arkani-Hamed, J., and D.W. Strangway, 1985b. Lateral variations of apparent susceptibility of lithosphere deduced from Magsat data, *J. Geophys. Res., 90*, 2655-2664.

Arkani-Hamed, J., and D.W. Strangway, 1986. Band-limited global scalar magnetic anomaly map of the Earth derived from Magsat data, *J. Geophys. Res., 91*, 8193-8203.

Arkani-Hamed, J., R.A. Langel, and M.E. Purucker, 1994. Magnetic anomaly maps of Earth derived from POGO and Magsat data, *J. Geophys. Res., 99*, 24075-24090.

Backus, G.E., 1986. Poloidal and toroidal fields in geomagnetic field modeling, *Rev. Geophys., 24*, 75-109.

Barton, C.E., 1997. International geomagnetic reference field: The seventh generation, *J. Geomag. Geoelec., 49*, 123-148.

Bloxham, J., D. Gubbins, and A. Jackson, 1989. Geomagnetic secular variation, *Phil. Trans. R. Soc. Lond., 329*, 415-502.

Cain, J.C., D.R. Schmitz, and L. Muth, 1984. Small-scale features in the Earth's magnetic field observed by Magsat, *J. Geophys. Res., 89*, 1070-1076.

Cain, J.C., Z. Wang, C. Kluth, and D.R. Schmitz, 1989a. Derivation of a geomagnetic model to $n = 63$, *Geophys. J., 97*, 431-441.

Cain, J.C., Z. Wang, D.R. Schmitz, and J. Meyer, 1989b. The geomagnetic spectrum for 1980 and core-crustal separation, *Geophys. J., 97*, 443-447.

Cain, J.C., B. Holter, and D. Sandee, 1990. Numerical experiments in geomagnetic modeling, *J. Geomag. Geoelec., 42*, 973-987.

Campbell, W.H., 1989. The regular geomagnetic field variations during quiet solar conditions, In: *Geomagnetism (3)*, Jacobs, J.A., (Ed.), Academic Press, London, 385-460.

Chapman, S., and J. Bartels, 1940. Geomagnetism, Clarendon Press, Oxford.

IAGA Division I Working Group 1, 1981. International Geomagnetic Reference Fields: DGRF 1965, DGRF 1970, DGRF 1975, and IGRF 1980, textitEos Trans. AGU, *57*, 120-121.

Jackson, A., 1994. Statistical treatment of crustal magnetization, *Geophys. J. Int., 119*, 991-998.

Kaiser, J.F., 1974. Nonrecursive digital filter design using the Io-sinh window function, *Proc. IEEE Int. Symp. Circuits Syst., 1974*, 20-23.

Kanasewich, E.R., 1981. Time sequence analysis in geophysics, The University of Alberta Press, Edmonton.

Langel, R.A., 1974. Near-earth magnetic disturbance in total field at high latitudes, 1, Summary of data from OGO 2, 4, and 6, *J. Geophys. Res., 79*, 2363-2371.

Langel, R.A., R.L. Coles, and M.A. Mayhew, 1980. Comparisons of magnetic anomalies of lithospheric origin measured by satellite and airborne magnetometers over western Canada, *Canad. J. of Ear. Sci., 17*, #7.

Langel, R.A., R.H. Estes, and G.D. Mead, 1982. Some new methods in geomagnetic field modeling applied to the 1960-1980 epoch, *J. Geomag. Geoelec., 34*, 327-349.

Langel, R.A., and R.H. Estes, 1982. A geomagnetic field spectrum, *Geophys. Res. Lett., 9*, 250-253.

Langel, R.A., and R.H. Estes, 1985a. Large-scale, near-Earth magnetic fields from external sources and the corresponding induced internal field, *J. Geophys. Res., 90*, 2487-2494.

Langel, R.A., and R.H. Estes, 1985b. The near-Earth magnetic field at 1980 determined from Magsat data, *J. Geophys. Res., 90*, 2495-2510.

Langel, R.A., 1987. The main geomagnetic field, In: *Geomagnetism (1)*, Jacobs, J.A., (Ed.), Academic Press, London, 249-512.

Langel, R.A., 1990. Global magnetic anomaly maps derived from POGO spacecraft data, *Phys. Earth Planet. Inter., 62*, 208-230.

Langel, R.A., and R.T. Baldwin, 1991. Geodynamics branch data base for main magnetic field analysis, *NASA Tech. Mem., 104542.*

Langel, R.A., M.E. Purucker, and M. Rajaram, 1993. The equatorial electrojet and associated currents as seen in Magsat data, *J. Atmos. Terr. Phys., 55*, 1233-1269.

Langel, R.A., T.J. Sabaka, R.T. Baldwin, and J.A. Conrad, 1996. The near-Earth magnetic field from magnetospheric and quiet-day ionospheric sources and how it is modeled, *Phys. Earth Planet. Inter., 98*, 235-267.

Langel, R.A., and W.J. Hinze, 1998. The magnetic field of the Earth's lithosphere: The satellite perspective, Cambridge University Press, Cambridge.

Lowes, F.J., 1974. Spatial power spectrum of the main geomagnetic field, and extrapolation to the core, *Geophys. J. R. Astr. Soc., 36*, 717-730.

Maeda, H., T. Iyemori, T. Araki, and T. Kamei, 1982. New evidence of a meridional current system in the equatorial ionosphere, *Geophys. Res. Lett., 9*, 337-340.

Malin, S.R.C., 1973. Worldwide distribution of geomagnetic tides, *Phil. Trans. Roy. Soc. Lond., A274*, 551-594.

Malin, S.R.C., and J.C. Gupta, 1977. The Sq current system during the International Geophysical Year, *Geophys. J. R. Astr. Soc., 49*, 515-529.

Malin, S.R.C., and A. Mete Isikara, 1976. Annual variation of the geomagnetic field, *Geophys. J. R. Astr. Soc., 47*, 445-457.

Matsushita, S., and H. Maeda, 1965. On the geomagnetic quiet solar daily variation field during the IGY, *J. Geophys. Res., 70*, 2535-2558.

Mauersberger, P., 1956. Das Mittel der Energiedichte des geomagnetischen Hauptfeldes an der Erdoberfläche und seine säkulare Änderung, *Gerlands Beitr. Geophys., 65*, 207-215.

Mayaud, P.N., 1972. The aa indices: a 100-year series characterizing magnetic activity, *J. Geophys. Res., 77*, 6870.

Mayaud, P.N., 1980. Derivation, meaning and use of geomagnetic indices, *Geophys. Monogr. Am. Geophys. Union, 22.*

Musmann, G., and E. Seiler, 1978. Detection of meridional currents in the equatorial ionosphere, *J. Geophys., 44*, 357-372.

Olsen, N., 1993. The solar cycle variability of lunar and solar daily geomagnetic variations, *Annales Geophys., 11*, 254-262.

Olsen, N., 1996. Magnetospheric contributions to geomagnetic daily variations, *Annales Geophys., 14*, 538-544.

Olsen, N., 1997a. Ionospheric *F*-region currents at middle and low latitudes estimated from Magsat data, *J. Geophys. Res., 102*, 4563-4576.

Olsen, N., 1997b. Geomagnetic tides and related phenomena, In: *Lecture notes in Earth Sciences, 66*, Wilhelm, H., (Ed.).

Olsen, N., 1998. The electrical conductivity of the mantle beneath Europe derived from C-Responses from 3 h to 720 h, *Geophys. J., 133*, 298-308.

Olsen, N., 1999. Induction studies with satellite data, *Surveys in Geophys.*, accepted.

Peredo, M., D.P. Stern, and N. A. Tsyganenko, 1993. Are existing magnetospheric models excessively stretched?, *J. Geophys. Res., 98*, 15343-15354.

Potemra, T.A., 1982. Birkeland currents: present understanding and some remaining questions, In: *High-Latitude Space Plasma Physics*, Hultqvist, B., and T. Hagfors, (Eds.), *Nobel Symposium, 54.*

Press, W.H., S.A. Teukolsky, W.T. Vetterling, and B.P. Flannery, 1992. Numerical recipes in FORTRAN: the art of scientific computing, Cambridge University Press, Cambridge.

Purucker, M.E., T.J. Sabaka, R.A. Langel, and N. Olsen, 1997. The missing dimension in Magsat and POGO anomaly studies, *Geophys. Res. Lett., 24*, 2909-2912.

Rangarajan, G.K., 1989. Indices of geomagnetic activity, In: *Geomagnetism (3)*, Jacobs, J.A., (Ed.), Academic Press, London, 323-384.

Ravat, D.N., R.A. Langel, M.E. Purucker, J. Arkani-Hamed, and D.E. Alsdorf, 1995. Global vector and scalar Magsat magnetic anomaly maps, *J. Geophys. Res., 100*, 20111-20135.

Richmond, A.D., 1995. Ionospheric electrodynamics using magnetic apex coordinates, *J. Geomag. Geoelec.*, *47*, 191-212.

Russell, C.T., 1971. Geophysical coordinate transformations, In: *Cosmic Electrodynamics*, *2*, D. Reidel, Dordrecht-Holland, 184-196.

Sabaka, T.J., and R.T. Baldwin, 1993. Modeling the Sq magnetic field from POGO and Magsat satellite and cotemporaneous hourly observatory data: Phase I, *Contract Report HSTX/G&G9302*, Hughes STX Corp. for NASA/GSFC Contract NAS5-31760.

Sabaka, T.J., R.A. Langel, R.T. Baldwin, and J.A. Conrad, 1997. The geomagnetic field 1900-1995, including the large-scale field from magnetospheric sources, and the NASA candidate models for the 1995 revision of the IGRF, *J. Geomag. Geoelec.*, *49*, 157-206.

Schmitz, D.R., J. Meyer, and J.C. Cain, 1989. Modeling the Earth's geomagnetic field to very high degree and order, *Geophys. J.*, *97*, 421-430.

Schmucker, U., 1985. Magnetic and electric fields due to electromagnetic induction by external sources, In: Landolt-Börnstein, New-Series, 5/2b, Springer-Verlag, Berlin-Heidelberg.

Schumaker, L.L., 1981. Spline functions: Basic theory, John Wiley & Sons, New York.

Seber, G.A.F., and C.J. Wild, 1989. Nonlinear regression, John Wiley & Sons, New York.

Sorenson, H.W., 1980. Parameter estimation, Marcel Dekker, Inc., New York.

Takeda, M., and H. Maeda, 1983. F-region dynamo in the evening - interpretation of equatorial ΔD anomaly found by Magsat, *J. Atmos. Terr. Phys.*, *45*, 401-408.

Tarantola, A., and B. Valette, 1982. Generalized non-linear inverse problems solved using the least squares criterion, *Rev. Geophys. Space Phys.*, *20*, 219-232.

Toutenburg, H., 1982. Prior information in linear models, John Wiley & Sons, New York.

Tsyganenko, N.A., 1987. Global quantitative models of the geomagnetic field in the cislunar magnetosphere for different disturbance levels, *Planet. Space Sci.*, *35*, 1347-1358.

Tsyganenko, N.A., 1989. A magnetospheric magnetic field model with a warped tail current sheet, *Planet. Space Sci.*, *37*, 5-20.

Voorhies, C.V., 1995. Time-varying fluid flow at the top of earth's core derived from definitive geomagnetic reference field models, *J. Geophys. Res.*, *100*, 10029-10039.

Winch, D.E., 1981. Spherical harmonic analysis of geomagnetic tides, 1964-1965, *Phil. Trans. Roy. Soc. Lond.*, *303*, 1-104.

A Observatory data synopsis

This appendix contains information pertinent to the observatory hourly (Tables 7-10) and annual (Tables 11-15) means data sets used in the CMP3 model, such as station breaks, location, time span, measurement count, and CMP3 vector biases and formal errors.

Table 7: Observatory hourly means listing.

Station	Lat. (deg)	Lon. (deg)	Height (km)	Time Span Begin	Time Span End	Number X	Number Y	Number Z	CMP3 Bias (Error) X (nT)		Y (nT)		Z (nT)	
Abisko vi	68.36	18.82	0.38	1968.0	1971.5	503	503	502	105	(20)	13	(20)	−95	(28)
Addis ababa	9.03	38.76	2.44	1965.7	1970.9	756	756	744	430	(24)	−265	(27)	−141	(37)
Agincourt	43.78	280.73	0.17	1965.7	1969.2	516	516	516	13	(27)	192	(29)	−111	(36)
Alert	82.50	297.65	0.06	1965.7	1982.9	1272	1282	1251	−26	(25)	−13	(17)	−78	(32)
Alibag ii	18.64	72.87	0.01	1965.7	1971.5	852	852	840	−112	(24)	346	(28)	623	(40)
Alibag iii	18.64	72.87	0.01	1980.0	1982.9	432	432	432	−202	(24)	429	(28)	617	(40)
Alma ata	43.25	76.92	1.30	1965.7	1982.9	1164	1164	1152	150	(22)	−9	(25)	−259	(34)
Almeria	36.85	357.54	0.06	1965.7	1966.2	60	60	60	−14	(21)	33	(22)	65	(31)
Amatsia	31.55	34.92	0.00	1979.9	1980.4	0	0	84	-----	(-)	-----	(-)	260	(30)
Amberley ii	−43.15	172.72	0.04	1965.7	1971.5	852	852	0	50	(26)	−2	(29)	-----	(-)
Annamalaina ii	11.37	79.68	0.00	1980.0	1982.9	407	407	432	128	(30)	−101	(34)	−82	(46)
Annamalainagar	11.37	79.68	0.00	1965.7	1967.8	72	72	71	177	(30)	−46	(34)	−39	(46)
Apia iv	−13.81	188.23	0.00	1965.7	1982.9	1164	1164	1235	−44	(26)	162	(30)	−811	(37)
Aquila	42.38	13.32	0.63	1965.7	1982.0	1164	1164	1152	2	(21)	26	(21)	−29	(28)
Argentine islnd	−65.24	295.74	0.01	1965.7	1982.9	1308	1308	1308	115	(32)	−34	(41)	594	(44)
Arti	56.43	58.57	0.29	1979.9	1982.9	456	456	444	80	(22)	−263	(22)	437	(31)
Baker lake iii	64.33	263.97	0.03	1965.7	1966.0	48	48	48	137	(24)	19	(26)	−186	(34)
Baker lake iv	64.33	263.97	0.03	1966.0	1969.0	432	432	432	139	(24)	19	(26)	−176	(33)
Baker lake v	64.33	263.97	0.03	1969.0	1971.5	372	372	360	229	(24)	−74	(26)	−160	(33)
Baker lake vii	64.33	263.97	0.03	1979.9	1982.9	444	444	452	153	(24)	50	(26)	−124	(33)
Bangui ii	4.44	18.57	0.39	1965.7	1966.0	48	48	48	115	(28)	8	(30)	186	(42)
Bangui iii	4.44	18.57	0.39	1966.0	1971.5	755	755	767	61	(28)	2	(30)	181	(42)
Bangui iv	4.44	18.57	0.39	1979.9	1982.9	240	240	240	15	(28)	−145	(29)	124	(41)
Barrow iv	71.30	203.25	0.00	1965.7	1971.5	766	766	767	58	(21)	−44	(21)	−28	(33)
Barrow v	71.32	203.38	0.00	1979.9	1982.9	442	444	444	67	(21)	−31	(21)	−26	(33)
Beijing ii	40.04	116.18	0.07	1979.9	1981.0	168	168	156	567	(25)	−253	(26)	345	(36)
Belsk ii	51.84	20.79	0.18	1966.0	1982.9	1259	1259	1260	90	(17)	61	(20)	279	(27)
Bereznayki	49.82	73.08	0.00	1965.7	1971.5	826	826	790	−420	(22)	−75	(21)	295	(34)
Bereznayki ii	49.82	73.08	0.00	1980.1	1980.5	60	60	60	−380	(22)	−209	(21)	295	(34)
Borok	58.03	38.97	0.00	1980.0	1982.9	420	420	420	−45	(23)	−69	(23)	−355	(33)
Boulder	40.14	254.76	1.65	1967.0	1982.9	1080	1080	1092	9	(26)	42	(25)	−158	(37)
Brorfelde	55.63	11.67	0.08	1981.1	1982.9	276	276	288	45	(19)	−122	(23)	−243	(29)
Byrd ii	−80.02	240.48	1.52	1965.7	1968.5	238	238	238	−27	(32)	87	(27)	−136	(41)
Cambridge bay	69.12	254.97	0.02	1979.9	1982.9	452	444	452	69	(21)	−92	(23)	58	(30)
Canberra	−35.31	149.36	0.85	1979.9	1982.9	384	384	384	43	(27)	57	(31)	127	(39)
Cape wellen iii	66.16	190.16	0.01	1965.7	1982.9	1231	1267	1259	−55	(21)	66	(22)	−64	(30)
Cha pa	22.35	103.83	0.00	1965.7	1966.0	46	46	47	205	(25)	−361	(28)	15768	(39)
Chambon for ii	48.02	2.26	0.14	1965.7	1971.5	852	852	852	−33	(23)	−16	(22)	103	(32)
Changchun ii	43.83	125.30	0.23	1979.9	1981.0	144	144	144	−121	(20)	44	(22)	142	(32)
Chelyuskin iv	77.72	104.28	0.01	1965.7	1982.9	1293	1296	1303	−43	(21)	−55	(20)	−34	(28)
Coimbra	40.22	351.58	0.10	1965.7	1966.0	48	48	48	0	(24)	2	(23)	89	(39)
College iii	64.86	212.16	0.09	1965.7	1982.9	1305	1306	1307	35	(21)	−22	(22)	−89	(31)
Dallas	32.99	263.25	0.21	1965.7	1971.5	730	730	742	−32	(28)	52	(28)	−60	(41)
Dikson iv	73.54	80.56	0.01	1965.7	1971.5	837	838	827	−33	(22)	−119	(21)	−241	(30)
Dikson v	73.54	80.56	0.01	1979.9	1982.9	440	444	455	−46	(22)	−84	(21)	−252	(30)
Dombas iii	62.07	9.12	0.66	1965.7	1969.7	84	84	84	−43	(20)	−185	(21)	−313	(30)
Dourbes	50.10	4.59	0.21	1965.7	1982.9	1308	1308	1308	20	(22)	8	(24)	114	(31)
Dumont durville	−66.67	140.01	0.04	1965.7	1982.9	1168	1141	1202	−208	(32)	−381	(32)	−2680	(51)
Dusheti ii	42.09	44.71	0.98	1965.7	1982.9	1308	1284	1308	−194	(23)	−10	(26)	−129	(32)
Ebro iv	40.82	0.49	0.05	1965.7	1966.8	156	168	168	19	(19)	1	(21)	1	(28)
Eights	−75.23	282.83	0.45	1965.7	1965.7	12	12	12	152	(32)	192	(30)	211	(45)
Eskdalemuir	55.32	356.80	0.24	1965.7	1982.9	1284	1284	1284	−7	(20)	5	(23)	−25	(29)
Eyrewell	−43.42	172.35	0.39	1979.9	1982.9	443	443	407	28	(25)	−25	(30)	105	(39)
Fort church ii	58.76	265.91	0.01	1968.0	1982.9	955	958	956	−97	(26)	68	(26)	−241	(37)
Fort churchill	58.76	265.91	0.01	1965.7	1967.9	323	312	298	−98	(26)	63	(26)	−220	(37)
Fredericksburg	38.21	282.63	0.07	1965.7	1980.3	924	924	924	49	(24)	−151	(27)	170	(35)
Fuquene	5.47	286.26	2.54	1965.7	1969.7	213	213	202	142	(28)	−87	(29)	112	(43)
Furstnfeldbruck	48.17	11.28	0.57	1965.7	1982.9	1303	1303	1305	−7	(19)	2	(19)	2	(27)
Gnangara	−31.78	115.95	0.06	1965.8	1982.9	1270	1270	1270	15	(38)	−139	(37)	52	(52)
Godhavn	69.24	306.48	0.01	1965.7	1971.5	851	851	850	243	(22)	−285	(21)	448	(34)
Godhavn ii	69.25	306.47	0.02	1979.9	1982.9	394	396	395	289	(22)	−332	(21)	741	(34)
Gornotayezh ii	43.68	132.17	0.30	1965.7	1982.9	1247	1259	1197	16	(24)	−28	(23)	−48	(35)
Great whale r	55.27	282.22	0.02	1965.8	1982.9	1230	1246	1236	314	(24)	39	(26)	−144	(38)
Grocka	44.63	20.77	0.23	1965.7	1966.0	48	48	48	19	(20)	−49	(22)	−72	(30)
Guam	13.58	144.87	0.15	1965.7	1980.3	886	886	875	122	(25)	102	(30)	48	(37)
Guangzhou	23.09	113.34	0.01	1979.9	1980.0	24	24	24	82	(28)	64	(29)	34	(39)

Table 8: Observatory hourly means listing (continued).

Station	Lat.	Lon.	Height	Time Span		Number			CMP3 Bias (Error)					
	(deg)	(deg)	(km)	Begin	End	X	Y	Z	X (nT)		Y (nT)		Z (nT)	
Guangzhou ii	23.09	113.34	0.01	1980.0	1981.0	144	144	144	110	(28)	53	(29)	58	(39)
Halley bay	−75.52	333.40	0.03	1965.7	1967.9	336	336	336	144	(31)	332	(31)	−274	(44)
Hartebeesthoek	−25.88	27.71	1.52	1980.0	1982.9	339	339	271	104	(29)	−67	(32)	41	(39)
Hartland	50.99	355.52	0.09	1965.7	1982.9	1308	1308	1308	−30	(21)	12	(22)	13	(31)
Havana	22.98	277.68	0.00	1965.7	1968.5	132	132	96	24	(29)	78	(29)	22	(42)
Heiss island	80.62	58.05	0.02	1965.7	1970.0	622	624	599	64	(23)	−652	(19)	1199	(31)
Hermanus	−34.42	19.23	0.03	1965.7	1982.9	1272	1272	1284	46	(29)	−39	(31)	−56	(43)
Honolulu iv	21.32	202.00	0.00	1965.7	1980.3	898	898	900	−161	(23)	101	(26)	−323	(35)
Huancayo	−12.05	284.66	3.31	1965.7	1980.3	372	372	384	69	(32)	−34	(32)	−67	(48)
Hyderabad	17.41	78.56	0.50	1965.7	1966.0	24	24	24	311	(28)	108	(35)	478	(45)
Irkutsk ii	52.27	104.27	0.50	1965.7	1982.9	1308	1295	1284	153	(25)	183	(25)	−152	(32)
Jaipur	26.92	75.80	0.00	1979.9	1982.9	395	395	431	191	(25)	−432	(28)	84	(39)
Kakioka iii	36.23	140.19	0.03	1965.7	1982.9	1248	1248	1248	−2	(24)	36	(26)	−53	(32)
Kanoya	31.42	130.88	0.11	1965.7	1982.9	1248	1248	1248	−65	(23)	116	(24)	−29	(34)
Kanozan	35.25	139.96	0.34	1980.0	1981.0	144	144	132	−22	(23)	29	(24)	−28	(33)
Kiev	50.72	30.30	0.10	1965.7	1982.9	1308	1308	1296	15	(19)	39	(21)	283	(28)
Kiruna	67.83	20.42	0.39	1965.7	1966.4	120	120	120	−764	(20)	−1813	(20)	−218	(27)
Kiruna ii	67.83	20.42	0.39	1967.7	1967.8	24	24	24	−856	(21)	−1848	(21)	−213	(28)
Kiruna iii	67.83	20.42	0.39	1970.1	1970.2	24	24	24	−758	(21)	−1824	(21)	−207	(28)
Klyuchi	55.03	82.90	0.00	1967.0	1971.5	624	624	624	227	(24)	−108	(26)	−285	(33)
Klyuchi ii	55.03	82.90	0.00	1979.9	1982.9	444	444	444	207	(24)	−31	(26)	−169	(33)
Kodaikanal ii	10.23	77.46	2.32	1980.0	1980.5	72	72	60	−543	(27)	301	(34)	−44	(43)
Koror ii	7.33	134.50	0.01	1965.7	1966.2	36	36	72	93	(27)	−154	(31)	530	(40)
La quiaca iv	−22.10	294.39	3.45	1965.7	1966.2	47	47	48	−15	(30)	36	(37)	425	(45)
Lanzhou	36.09	103.85	1.56	1980.0	1981.0	144	144	144	−51	(23)	−21	(26)	25	(34)
Leirvogur	64.18	338.30	0.00	1965.7	1982.9	1130	1135	1196	−300	(20)	590	(20)	−510	(29)
Lerwick ii	60.13	358.82	0.09	1965.7	1982.9	1308	1308	1308	−83	(22)	179	(23)	2	(32)
Logrono	42.46	357.49	0.44	1965.7	1966.2	60	60	60	0	(20)	−6	(22)	34	(29)
Lovo	59.35	17.83	0.03	1965.7	1981.0	276	276	444	68	(20)	−39	(21)	20	(28)
Luanda bela ii	−8.92	13.17	0.05	1965.7	1967.8	35	35	24	289	(26)	−14	(25)	65	(39)
Lunping	25.00	121.17	0.10	1980.0	1982.9	432	432	432	43	(26)	−43	(26)	112	(37)
Lvov ii	49.90	23.75	0.40	1965.7	1971.5	852	852	852	109	(20)	68	(19)	75	(28)
Lwiro	−2.25	28.80	1.68	1965.7	1966.0	48	48	48	315	(25)	−60	(29)	271	(38)
M bour	14.39	343.04	0.00	1965.7	1982.9	1008	1008	1008	96	(24)	26	(28)	106	(38)
Macquarie i ii	−54.50	158.95	0.00	1965.7	1968.3	131	131	121	336	(34)	−23	(36)	253	(42)
Maputo ii	−25.92	32.58	0.05	1980.0	1982.9	416	416	417	376	(27)	89	(29)	−126	(39)
Martin vivies	−37.83	77.57	0.00	1981.3	1982.9	240	240	240	−498	(37)	−688	(33)	−2030	(51)
Mawson	−67.61	62.88	0.00	1965.7	1982.9	491	492	491	32	(32)	0	(32)	104	(45)
Meanook iii	54.62	246.65	0.70	1965.7	1982.9	1296	1296	1296	142	(23)	31	(25)	−115	(35)
Memambetsu ii	43.91	144.19	0.04	1965.7	1982.9	1284	1284	1272	−170	(23)	143	(22)	−19	(32)
Mirnyy ii	−66.55	93.02	0.02	1965.7	1966.9	192	192	192	−115	(34)	4	(39)	−232	(51)
Mirnyy iii	−66.55	93.02	0.02	1967.0	1982.9	1101	1103	1094	−111	(34)	−17	(38)	−278	(51)
Misallat	29.52	30.89	0.12	1965.7	1966.0	48	48	48	−50	(23)	−12	(25)	120	(33)
Mizusawa	39.01	141.08	0.12	1980.0	1982.9	432	432	432	−158	(24)	83	(27)	−162	(35)
Moca	3.34	8.66	1.35	1965.7	1969.7	276	276	276	−121	(21)	5	(29)	106	(33)
Molodezhnaya	−67.67	45.85	0.00	1965.7	1971.5	848	848	708	−50	(29)	−76	(30)	−114	(42)
Moscow	55.73	37.63	0.08	1965.7	1982.9	1308	1308	1308	333	(23)	25	(23)	169	(34)
Mould bay	76.32	240.64	0.04	1965.7	1982.9	1305	1304	1303	12	(21)	112	(21)	−4	(32)
Muntinlupa	14.37	121.01	0.06	1965.7	1971.5	838	838	839	−155	(27)	765	(33)	407	(44)
Murmansk ii	68.95	33.05	0.21	1965.7	1980.8	990	992	995	400	(20)	300	(20)	−613	(29)
Nairobi	−1.33	36.81	1.67	1965.7	1967.4	108	108	108	87	(26)	295	(28)	711	(39)
Narssarssuaq	61.10	314.80	0.00	1968.1	1982.9	825	826	848	−385	(21)	283	(22)	516	(29)
Newport	48.26	242.88	0.78	1966.3	1982.9	1224	1224	1212	−38	(23)	98	(24)	−63	(34)
Niemegk ii	52.07	12.67	0.08	1965.7	1982.9	1284	1284	1284	−25	(19)	−2	(21)	−12	(29)
Novo kazalinsk	45.80	62.10	0.00	1980.0	1980.5	72	72	72	−19	(25)	−143	(26)	7	(34)
Novolazarev ii	−70.77	11.83	0.46	1969.0	1971.5	371	371	371	−186	(29)	45	(29)	102	(43)
Novolazarevskay	−70.77	11.83	0.46	1965.7	1969.0	480	480	479	−176	(29)	38	(29)	244	(43)
Nurmijarvi	60.51	24.66	0.11	1965.7	1982.9	1308	1308	1308	325	(19)	−46	(21)	134	(29)
O gyalla pesth	47.87	18.19	0.12	1965.7	1982.0	347	347	348	45	(19)	−8	(20)	−18	(26)
Ottawa	45.40	284.45	0.08	1968.5	1982.9	864	852	864	137	(25)	−159	(26)	145	(36)
Pamatai ii	−17.57	210.43	0.09	1968.0	1971.5	515	515	513	−694	(29)	−678	(30)	−164	(43)
Pamatai iii	−17.57	210.43	0.09	1979.9	1982.9	384	384	384	−654	(28)	−660	(29)	−105	(42)
Panagyurishte	42.51	24.18	0.56	1965.7	1966.0	48	48	48	−192	(21)	−202	(22)	−196	(30)
Paramaribo	5.81	304.78	0.00	1965.7	1969.7	287	287	286	−39	(26)	78	(29)	−23	(39)
Paratunka	52.90	158.43	0.11	1969.0	1982.9	804	804	803	−359	(20)	194	(22)	197	(32)
Pilar ii	−31.67	296.12	0.34	1965.7	1968.5	323	323	299	36	(33)	−60	(34)	23	(47)

Table 9: Observatory hourly means listing (continued).

Station	Lat.	Lon.	Height	Time Span		Number			CMP3 Bias (Error)					
	(deg)	(deg)	(km)	Begin	End	X	Y	Z	X (nT)		Y (nT)		Z (nT)	
Pionerskaya	−69.73	95.50	2.70	1971.1	1971.5	72	72	72	104	(34)	70	(38)	321	(51)
Plateau	−79.25	40.50	3.62	1966.2	1968.9	369	369	365	1	(30)	−42	(28)	−28	(47)
Pleshenitzi	54.50	27.88	0.20	1965.7	1982.9	1271	1271	1284	258	(19)	135	(22)	−171	(28)
Podkam tung ii	61.60	90.00	0.00	1980.0	1982.9	384	384	395	30	(22)	−42	(22)	−192	(33)
Podkam tunguska	61.60	90.00	0.00	1969.0	1980.0	384	384	384	97	(22)	1	(22)	−316	(33)
Port moresby	−9.41	147.15	0.08	1965.7	1982.9	1270	1270	1269	13	(31)	65	(35)	407	(48)
Port-alfred	−46.43	51.87	0.00	1979.9	1981.0	168	168	168	−620	(28)	1225	(29)	121	(45)
Port-alfred ii	−46.43	51.87	0.00	1981.1	1982.9	287	287	287	−707	(28)	1078	(30)	101	(45)
Port-aux-franca	−49.35	70.20	0.05	1965.7	1982.9	1217	1217	1242	205	(34)	233	(35)	548	(50)
Pruhonice	49.99	14.55	0.33	1965.7	1966.0	36	36	36	8	(19)	51	(20)	−57	(28)
Quetta	30.19	66.95	1.75	1965.7	1966.0	48	48	48	−7	(24)	−45	(29)	−4	(38)
Resolute bay	74.69	265.10	0.03	1965.7	1982.9	1035	1056	1033	−6	(21)	87	(20)	49	(31)
Roburent	44.30	7.89	0.81	1965.8	1966.0	24	36	36	−23	(18)	−28	(22)	51	(27)
Roi baudoui ii	−70.43	24.30	0.14	1965.7	1966.9	191	191	180	−52	(28)	−120	(28)	53	(41)
Rude skov	55.84	12.46	0.05	1965.7	1982.0	1140	1140	1140	38	(20)	−19	(22)	−110	(29)
Sabhawala	30.36	77.80	0.50	1965.7	1966.9	192	192	192	16	(27)	−65	(28)	32	(39)
San fernando	36.46	353.80	0.03	1965.7	1966.2	60	60	0	83	(21)	6	(24)	----	(-)
San juan ii	18.11	293.85	0.40	1965.7	1982.9	1223	1223	1211	−55	(22)	215	(26)	260	(36)
San miguel iii	37.77	334.35	0.17	1965.8	1965.9	24	24	24	727	(20)	425	(23)	1723	(31)
Sanae i	−70.30	357.63	0.05	1965.7	1970.9	755	755	743	49	(29)	−8	(30)	28	(41)
Sanae ii	−70.32	357.66	0.05	1971.0	1971.5	48	24	48	38	(29)	7	(30)	36	(41)
Sanae iii	−70.31	357.59	0.05	1980.0	1982.9	420	420	420	49	(29)	−9	(30)	18	(41)
Scott base ii	−77.85	166.78	0.01	1965.7	1982.9	1219	1239	1228	−2236	(32)	−820	(32)	−3824	(46)
Sheshan	31.10	121.19	0.10	1965.7	1982.9	1296	1296	1307	−190	(22)	480	(27)	274	(35)
Shillong	25.57	91.88	0.00	1980.0	1982.9	431	431	420	−62	(33)	−79	(35)	−489	(44)
Simosato	33.58	135.94	0.06	1965.7	1966.0	48	48	48	−90	(24)	17	(24)	−32	(35)
Sitka iii	57.06	224.68	0.02	1965.7	1982.9	1246	1246	1247	−12	(22)	29	(23)	−38	(32)
Sodankyla ii	67.37	26.63	0.18	1965.7	1982.9	1308	1308	1308	−124	(20)	−23	(20)	−669	(28)
South georg ii	−54.52	323.98	0.58	1979.9	1982.2	348	348	348	−20	(30)	−307	(34)	288	(46)
South pole	−89.99	346.68	2.80	1965.7	1971.5	741	741	717	−1332	(69)	−3344	(72)	53	(148)
St john s	47.59	307.32	0.10	1968.7	1982.0	744	744	744	124	(26)	37	(26)	16	(37)
Stekoliniy	60.12	151.02	0.00	1966.8	1980.0	720	720	720	−230	(20)	−664	(21)	−16	(28)
Stekoliniy ii	60.12	151.02	0.00	1980.0	1982.9	432	432	432	−68	(20)	38	(21)	22	(28)
Stepanovka iii	46.78	30.88	0.14	1965.7	1982.9	1284	1308	1308	−96	(19)	−699	(21)	76	(29)
Stonyhurst iii	53.85	357.53	0.12	1965.7	1966.0	48	48	48	47	(20)	52	(23)	−2	(29)
Sukkertoppen	65.42	307.08	0.00	1965.8	1966.2	36	36	36	−61	(21)	12	(23)	966	(32)
Surlari ii	44.68	26.25	0.08	1965.7	1966.0	48	48	36	7	(22)	−54	(23)	−127	(31)
Swider	52.12	21.25	0.10	1965.7	1966.0	48	48	36	−329	(18)	−179	(20)	200	(27)
Tahiti	−17.56	210.39	0.09	1966.2	1970.2	131	131	118	−639	(29)	−1070	(30)	306	(43)
Tananarive iii	−18.92	47.55	1.38	1965.7	1970.2	318	330	323	438	(26)	−15	(27)	−373	(40)
Tangerang	−6.17	106.63	0.01	1965.8	1969.7	125	143	120	−500	(26)	141	(30)	−686	(37)
Tatuoca ii	−1.20	311.49	0.01	1965.7	1965.9	36	36	36	−14	(30)	−46	(33)	266	(43)
Tehran	35.74	51.38	1.37	1965.7	1967.6	72	72	72	−24	(21)	53	(23)	−215	(32)
Teoloyucan vi	19.75	260.82	2.28	1965.7	1966.0	48	48	48	−90	(26)	73	(29)	−42	(40)
Thule i ii	77.48	290.83	0.06	1965.7	1982.9	1308	1306	1289	−39	(21)	26	(20)	−109	(28)
Tihany	46.90	17.89	0.19	1965.7	1966.0	48	48	48	34	(18)	−9	(21)	−15	(28)
Tiksi v	71.58	129.00	0.04	1965.7	1967.8	311	311	300	−41	(20)	−140	(21)	−79	(30)
Tiksi vi	71.58	129.00	0.04	1969.1	1982.9	501	503	211	−31	(20)	−164	(21)	−69	(29)
Toledo iii	39.88	355.95	0.50	1965.7	1980.3	298	298	288	39	(20)	−2	(24)	−16	(31)
Tomsk	56.47	84.93	0.20	1965.8	1966.0	36	36	36	82	(25)	−41	(24)	−388	(35)
Toolangi iii	−37.53	145.47	0.46	1965.7	1970.2	420	420	419	−16	(29)	−1	(30)	80	(43)
Trelew	−43.25	294.68	0.03	1965.7	1968.2	348	348	336	172	(30)	86	(37)	−53	(47)
Trivandrum	8.48	76.95	0.30	1965.7	1982.9	370	370	393	228	(26)	221	(35)	198	(39)
Tromso	69.66	18.95	0.11	1965.7	1968.3	96	96	95	106	(20)	−445	(20)	173	(27)
Tsumeb	−19.22	17.70	0.08	1965.8	1982.0	1116	1116	1116	57	(30)	−64	(32)	90	(42)
Tucson	32.25	249.17	0.77	1965.8	1982.9	1293	1293	1260	−70	(22)	−105	(29)	90	(32)
Ujjain	23.18	75.78	0.00	1980.0	1982.9	371	383	431	−277	(26)	178	(28)	347	(41)
Valentia iii	51.93	349.75	0.01	1965.7	1982.9	1308	1308	1308	138	(20)	−70	(22)	13	(29)
Vannovskaya ii	37.95	58.11	0.57	1965.7	1982.9	1139	1139	1140	199	(22)	91	(22)	48	(32)
Vassouras	−22.40	316.35	0.46	1968.2	1980.5	108	108	108	90	(31)	4	(32)	120	(49)
Victoria	48.52	236.58	0.20	1965.7	1982.9	1284	1284	1296	13	(26)	−20	(25)	−400	(38)
Vieques	18.15	294.55	0.02	1965.7	1965.9	36	36	36	−579	(24)	−404	(26)	12157	(38)
Vostok	−78.45	106.87	3.50	1965.7	1982.9	1171	1170	1160	0	(38)	63	(32)	188	(50)
Voyeykovo	59.95	30.70	0.07	1965.7	1982.9	1296	1296	1308	30	(20)	−65	(21)	−165	(32)
Vysokay dub iii	56.73	61.07	0.29	1965.7	1966.9	192	192	192	−264	(22)	−111	(22)	−500	(31)
Vysokay dub iv	56.73	61.07	0.29	1967.0	1971.5	660	660	660	−263	(22)	−105	(22)	−474	(31)
Vysokay dub v	56.73	61.07	0.29	1979.9	1981.0	168	168	156	333	(22)	−287	(22)	−164	(31)

Table 10: Observatory hourly means listing (continued).

Station	Lat. (deg)	Lon. (deg)	Height (km)	Time Span Begin	Time Span End	Number X	Number Y	Number Z	CMP3 Bias (Error) X (nT)		CMP3 Bias (Error) Y (nT)		CMP3 Bias (Error) Z (nT)	
Whiteshell	49.75	264.75	0.00	1980.0	1980.6	96	96	96	199	(26)	−222	(30)	−242	(38)
Wien kobenzl	48.26	16.32	0.40	1965.7	1966.0	48	48	48	57	(19)	4	(19)	40	(26)
Wilkes	−66.25	110.58	0.01	1965.7	1966.0	60	48	60	672	(43)	−390	(41)	126	(60)
Wingst	53.74	9.07	0.05	1965.7	1966.0	48	48	48	10	(22)	47	(21)	−36	(30)
Witteveen	52.81	6.67	0.02	1965.7	1982.9	1308	1308	1308	2	(21)	30	(21)	−46	(31)
Wuhan	30.53	114.56	0.04	1980.0	1981.0	144	144	144	73	(25)	5	(28)	−25	(37)
Yakutsk iii	62.02	129.72	0.10	1965.7	1982.9	1296	1296	1308	80	(19)	−1155	(21)	95	(28)
Yangi-bazar ii	41.33	69.62	0.81	1965.7	1980.5	912	912	912	−274	(23)	24	(24)	−115	(34)
Yellow-knife	62.48	245.52	0.20	1979.9	1982.9	456	456	419	455	(23)	−201	(23)	115	(34)
Yuzhno sakh ii	46.95	142.72	0.07	1965.7	1970.0	588	588	588	48	(23)	−63	(25)	−187	(31)
Yuzhno sakh iii	46.95	142.72	0.07	1970.1	1971.5	228	228	228	−123	(23)	−30	(25)	96	(31)
Yuzhno sakh iv	46.95	142.72	0.07	1979.9	1982.9	432	420	444	−93	(23)	0	(25)	108	(31)
Zaymishche ii	55.83	48.85	0.08	1965.7	1971.5	852	852	852	−219	(20)	−265	(23)	−335	(29)
Zaymishche iii	55.83	48.85	0.08	1979.9	1982.9	456	456	456	−65	(20)	−89	(23)	33	(29)

Table 11: Observatory annual means listing.

Station	Lat.	Lon.	Height	Time Span		Number			CMP3 Bias (Error)					
	(deg)	(deg)	(km)	Begin	End	X	Y	Z	X (nT)		Y (nT)		Z (nT)	
Abisko vi	68.36	18.82	0.38	1965.5	1984.5	20	20	20	97	(21)	25	(22)	−67	(29)
Acacias	−35.01	302.31	0.02	1964.5	1984.5	21	21	21	−44	(26)	−1	(32)	−99	(43)
Adak	51.87	183.36	0.00	1964.8	1966.0	3	3	3	−404	(29)	29	(29)	−103	(36)
Addis ababa	9.03	38.76	2.44	1960.5	1974.5	15	15	15	408	(26)	−265	(29)	−134	(39)
Addis ababa ii	9.03	38.76	2.44	1976.5	1984.5	9	9	9	547	(28)	−276	(30)	129	(40)
Agincourt	43.78	280.73	0.17	1960.5	1969.1	10	10	10	−10	(29)	194	(31)	−87	(38)
Alert	82.50	297.50	0.06	1961.9	1984.5	22	22	22	−3	(26)	−9	(18)	−40	(32)
Alibag ii	18.64	72.87	0.01	1960.5	1977.5	18	18	18	−155	(26)	365	(29)	638	(41)
Alibag iii	18.64	72.87	0.01	1978.5	1984.5	7	7	7	−231	(27)	428	(30)	607	(42)
Alma ata	43.25	76.92	1.30	1963.4	1984.5	22	22	22	118	(23)	−9	(26)	−256	(34)
Almeria	36.85	357.54	0.06	1960.5	1984.5	25	25	25	−79	(22)	22	(23)	65	(32)
Amatsia	31.55	34.92	0.00	1976.5	1984.5	9	9	9	70	(24)	22	(26)	217	(33)
Amberley ii	−43.15	172.72	0.04	1960.5	1977.5	18	18	18	17	(28)	−13	(30)	165	(42)
Annamalaina ii	11.37	79.68	0.00	1979.5	1984.5	6	6	6	107	(32)	−107	(36)	−85	(48)
Annamalainagar	11.37	79.68	0.00	1960.5	1978.5	17	17	17	149	(31)	−46	(35)	−67	(47)
Apia iv	−13.81	188.23	0.00	1960.5	1984.5	25	25	25	−69	(27)	158	(31)	−817	(38)
Aquila	42.38	13.32	0.63	1960.5	1984.5	25	25	25	−25	(22)	31	(22)	−17	(29)
Arctowski	−62.16	301.52	0.01	1978.5	1984.5	7	7	7	−218	(39)	349	(38)	733	(54)
Argentine islnd	−65.24	295.74	0.01	1960.5	1983.5	24	24	24	87	(33)	−32	(42)	584	(45)
Arti	56.43	58.57	0.29	1973.5	1984.5	12	12	12	54	(24)	−258	(24)	458	(32)
Baker lake iii	64.33	263.97	0.05	1960.5	1965.5	6	6	6	137	(29)	27	(31)	−137	(39)
Baker lake iv	64.33	263.97	0.05	1966.5	1968.5	3	3	3	126	(30)	19	(32)	−147	(38)
Baker lake v	64.33	263.97	0.05	1969.5	1972.5	4	4	4	220	(29)	−75	(30)	−133	(37)
Baker lake vii	64.33	263.97	0.05	1975.5	1984.5	10	10	10	126	(26)	42	(28)	−95	(35)
Bangui ii	4.44	18.57	0.39	1960.3	1965.5	6	6	6	51	(34)	49	(35)	191	(47)
Bangui iii	4.44	18.57	0.39	1966.5	1972.5	7	7	7	37	(30)	12	(32)	186	(43)
Bangui iv	4.44	18.57	0.39	1973.5	1984.5	12	12	12	−15	(30)	−124	(31)	161	(43)
Barrow iii	71.30	203.25	0.00	1960.5	1962.5	3	3	3	89	(35)	−66	(31)	152	(45)
Barrow iv	71.30	203.25	0.00	1963.5	1984.5	21	21	21	35	(22)	−59	(22)	−2	(34)
Beijing ii	40.04	116.18	0.07	1960.5	1984.5	25	25	25	634	(26)	−157	(27)	369	(37)
Belsk ii	51.84	20.79	0.18	1966.5	1984.5	19	19	19	66	(19)	71	(22)	293	(28)
Bereznayki	49.82	73.08	0.00	1965.5	1976.5	12	12	12	−446	(24)	−60	(23)	310	(35)
Bereznayki ii	49.82	73.08	0.00	1977.5	1980.5	4	4	4	−423	(27)	−229	(27)	300	(37)
Bereznayki iii	49.82	73.08	0.00	1981.5	1984.5	4	4	4	−447	(27)	−284	(27)	247	(38)
Binza	−4.27	15.37	0.00	1960.5	1973.5	14	14	14	−95	(28)	−31	(30)	−120	(41)
Bjornoya ii	74.50	19.20	0.08	1960.5	1984.5	25	25	25	−116	(21)	−3	(21)	4	(30)
Borok	58.03	38.97	0.00	1977.5	1984.5	8	8	8	−64	(26)	−57	(26)	−347	(35)
Boulder	40.14	254.76	1.65	1964.5	1984.5	21	21	21	−22	(27)	37	(26)	−129	(38)
Brorfelde	55.63	11.67	0.08	1980.5	1982.5	3	3	3	27	(27)	−112	(29)	−236	(34)
Budkov	49.08	14.02	0.50	1967.5	1984.5	18	18	18	−39	(21)	9	(21)	−19	(28)
Byrd ii	−80.02	240.48	1.52	1962.5	1968.3	6	6	6	−48	(36)	96	(31)	−173	(44)
Cambridge bay	69.20	255.00	0.02	1972.5	1984.5	13	13	13	85	(23)	−86	(24)	100	(32)
Canarias	28.48	343.74	0.31	1960.5	1984.5	21	21	21	−454	(27)	166	(29)	−978	(40)
Canberra	−35.31	149.36	0.85	1979.5	1984.5	6	6	6	27	(31)	50	(34)	115	(42)
Cape wellen iii	66.16	190.16	0.01	1960.5	1984.5	25	25	25	−71	(22)	43	(23)	−57	(31)
Casey	−66.28	110.53	0.00	1978.5	1983.5	4	4	4	859	(46)	−398	(44)	−765	(62)
Castellacci iii	44.43	8.93	0.35	1960.5	1962.5	3	3	3	4	(27)	−206	(29)	−145	(34)
Castello tesino	46.05	11.65	1.20	1965.5	1984.5	20	20	20	−9	(21)	31	(21)	−10	(30)
Castle rock	37.24	237.87	0.13	1970.5	1974.5	5	5	5	−149	(29)	−25	(32)	−62	(41)
Cha pa	22.35	103.83	0.00	1960.5	1979.5	20	20	20	171	(26)	−305	(29)	−948	(40)
Cha pa ii	22.35	103.83	0.00	1980.5	1983.5	4	4	4	−359	(30)	−118	(32)	−335	(42)
Chambon for ii	48.02	2.26	0.14	1960.5	1984.5	25	25	25	−59	(24)	−22	(23)	124	(33)
Changchun	43.83	125.30	0.23	1960.5	1978.5	19	19	19	−143	(22)	10	(23)	68	(33)
Changchun ii	44.05	125.20	0.23	1979.5	1984.5	5	5	5	−12	(25)	48	(26)	−90	(36)
Chelyuskin iii	77.72	104.28	0.01	1960.5	1962.5	3	3	3	−64	(35)	−50	(34)	−82	(43)
Chelyuskin iv	77.72	104.28	0.01	1963.5	1984.5	21	21	21	−68	(22)	−46	(21)	−3	(29)
Chichijima	27.08	142.17	0.15	1973.5	1983.5	11	11	11	−351	(25)	−41	(28)	331	(36)
Coimbra	40.22	351.58	0.10	1960.5	1984.5	25	25	25	−33	(25)	7	(24)	77	(39)
College iii	64.86	212.16	0.09	1960.5	1984.5	25	25	25	17	(23)	−36	(23)	−61	(32)
Dallas	32.99	263.25	0.21	1964.5	1974.5	11	11	11	−61	(30)	44	(30)	−53	(43)
Davis	−68.58	77.97	0.00	1981.5	1984.5	4	4	4	−324	(40)	280	(40)	296	(53)
Del rio	29.94	259.08	0.00	1982.5	1984.5	3	3	3	−138	(38)	387	(37)	−335	(51)
Dikson iii	73.54	80.56	0.01	1960.5	1962.5	3	3	3	−39	(33)	−100	(33)	−241	(43)
Dikson iv	73.54	80.56	0.01	1963.5	1973.5	11	11	11	−53	(24)	−110	(23)	−221	(32)
Dikson v	73.54	80.56	0.01	1974.5	1984.5	11	11	11	−66	(24)	−82	(23)	−217	(32)
Dombas iii	62.07	9.12	0.66	1960.5	1984.5	25	25	25	−58	(21)	−172	(22)	−297	(31)

Table 12: Observatory annual means listing (continued).

Station	Lat.	Lon.	Height	Time Span		Number			CMP3 Bias (Error)					
	(deg)	(deg)	(km)	Begin	End	X	Y	Z	X (nT)		Y (nT)		Z (nT)	
Dourbes	50.10	4.59	0.21	1960.5	1984.5	25	25	25	−3	(23)	13	(25)	129	(31)
Dumont durville	−66.66	140.01	0.04	1960.5	1984.5	24	24	24	−226	(33)	−385	(33)	−2883	(52)
Dusheti ii	42.09	44.71	0.98	1960.5	1983.5	24	24	24	−219	(24)	1	(27)	−118	(33)
Dymer	50.72	30.30	0.10	1964.5	1984.5	21	21	21	−9	(21)	52	(22)	303	(29)
Ebro iv	40.82	0.49	0.05	1960.5	1980.5	20	20	20	−3	(20)	2	(22)	−3	(29)
Eights	−75.23	282.83	0.45	1963.6	1965.4	3	3	3	165	(38)	156	(37)	253	(50)
Eskdalemuir	55.32	356.80	0.24	1960.5	1984.5	25	25	25	−26	(21)	13	(24)	−4	(30)
Etaiyapuram	9.00	78.00	0.00	1980.5	1983.5	4	4	4	22	(33)	−68	(35)	457	(50)
Eyrewell	−43.42	172.35	0.39	1978.5	1984.5	7	7	7	−2	(28)	−29	(32)	95	(41)
Fort church ii	58.77	265.90	0.04	1968.5	1984.5	17	17	17	−118	(28)	58	(27)	−206	(38)
Fort churchill	58.77	265.90	0.04	1964.5	1967.5	4	4	4	−115	(31)	61	(31)	−204	(41)
Fredericksburg	38.21	282.63	0.07	1960.5	1984.5	25	25	25	14	(25)	−140	(28)	195	(36)
Fresno	37.09	240.28	0.00	1982.5	1984.5	3	3	3	−141	(35)	168	(39)	−272	(47)
Fuquene	5.47	286.26	2.54	1960.5	1982.5	23	23	23	105	(29)	−61	(31)	138	(44)
Furstnfeldbruck	48.17	11.28	0.57	1960.5	1984.5	25	25	25	−34	(20)	8	(21)	15	(28)
Glenlea	49.60	262.90	0.00	1982.5	1984.5	3	3	3	−258	(34)	121	(34)	353	(46)
Gnangara	−31.78	115.95	0.06	1960.5	1984.5	25	25	25	−7	(39)	−137	(38)	42	(53)
Godhavn	69.24	306.48	0.02	1960.5	1975.5	16	16	16	233	(24)	−272	(23)	468	(35)
Godhavn ii	69.25	306.47	0.02	1976.5	1984.5	9	9	9	271	(25)	−328	(24)	760	(36)
Gornotayezh ii	43.68	132.17	0.30	1965.5	1984.5	20	20	20	−14	(25)	−22	(24)	−32	(35)
Gornotayezhnaya	43.68	132.17	0.30	1960.5	1964.5	5	5	5	−6	(29)	−48	(29)	−1	(39)
Grahamstown	−33.31	26.50	0.00	1974.8	1980.1	8	8	8	−160	(32)	−11	(33)	24	(42)
Great whale r	55.27	282.22	0.02	1965.5	1984.5	20	20	20	287	(25)	47	(27)	−113	(39)
Grocka	44.63	20.77	0.23	1960.5	1984.5	25	25	25	−9	(21)	−43	(23)	−66	(31)
Grytviken	−53.72	323.52	0.00	1975.5	1982.2	8	8	8	15	(33)	−185	(36)	−209	(49)
Guam	13.58	144.87	0.15	1960.5	1984.5	25	25	25	152	(26)	32	(31)	107	(39)
Guangzhou	23.09	113.34	0.01	1960.5	1979.5	20	20	20	197	(29)	540	(30)	−358	(40)
Guangzhou ii	23.09	113.34	0.01	1980.5	1984.5	5	5	5	150	(32)	73	(33)	50	(42)
Hallett station	−72.32	170.22	0.00	1960.8	1962.5	3	3	3	339	(71)	173	(101)	−576	(135)
Halley bay	−75.52	333.40	0.03	1960.5	1967.5	8	8	8	120	(34)	394	(34)	−270	(47)
Halley bay ii	−75.52	333.40	0.03	1971.5	1980.5	4	4	4	178	(36)	290	(35)	−266	(48)
Hartebeesthoek	−25.88	27.71	1.52	1980.5	1984.5	5	5	5	77	(32)	−62	(35)	39	(42)
Hartland	50.99	355.52	0.09	1960.5	1984.5	25	25	25	−50	(22)	20	(23)	29	(32)
Hatizyo ii	33.12	139.80	0.00	1981.5	1984.5	4	4	4	−22	(29)	−818	(29)	394	(37)
Havana	22.97	277.86	0.00	1968.5	1979.5	8	8	8	−8	(33)	146	(33)	−12	(45)
Havana ii	22.98	277.68	0.00	1980.5	1984.5	3	3	3	60	(41)	119	(40)	−160	(51)
Heiss islan ii	80.62	58.05	0.02	1976.5	1984.5	9	9	9	88	(26)	−653	(22)	1169	(33)
Heiss island	80.62	58.05	0.02	1960.5	1973.5	14	14	14	52	(25)	−648	(21)	1215	(32)
Hel iii	54.61	18.82	0.00	1960.5	1984.5	25	25	25	−4	(20)	−189	(22)	−127	(27)
Hermanus	−34.42	19.23	0.03	1960.5	1984.5	25	25	25	7	(30)	−28	(32)	−55	(44)
Hollandia	−2.57	140.51	0.23	1960.5	1962.3	3	3	3	−408	(125)	−110	(103)	−622	(146)
Hongkong vi	22.36	114.22	0.56	1974.5	1978.5	5	5	5	−34	(31)	431	(33)	−317	(43)
Honolulu iv	21.32	202.00	0.00	1961.5	1984.5	24	24	24	−163	(25)	118	(28)	−300	(37)
Hornsund	77.00	15.55	0.01	1978.5	1984.5	7	7	7	−37	(24)	−152	(23)	−25	(33)
Huancayo	−12.05	284.66	3.31	1960.5	1984.5	25	25	25	39	(34)	−39	(33)	−67	(49)
Hurbanovo	47.87	18.19	0.12	1960.5	1984.5	25	25	25	17	(20)	1	(21)	0	(27)
Hyderabad	17.41	78.56	0.50	1965.5	1984.5	19	19	19	271	(29)	58	(36)	431	(45)
Ibadan	7.43	3.90	0.30	1960.5	1964.5	5	5	5	−48	(34)	−509	(36)	28	(45)
Ibadan ii	7.43	3.90	0.30	1965.5	1975.5	11	11	11	25	(27)	−435	(30)	−23	(39)
Istanbl knd ii	41.06	29.06	0.13	1982.5	1984.5	3	3	3	184	(29)	121	(30)	−96	(39)
Istanbl kndilli	41.06	29.06	0.13	1960.5	1981.5	21	21	21	175	(24)	92	(25)	13	(34)
Jaipur	26.92	75.80	0.00	1979.5	1984.5	6	6	6	177	(29)	−421	(31)	95	(42)
Julianehaab ii	60.72	313.97	0.46	1960.6	1964.6	3	3	3	38	(34)	−152	(34)	287	(40)
Kakioka iii	36.23	140.19	0.03	1960.5	1984.5	25	25	25	−35	(25)	30	(27)	−53	(33)
Kanoya	31.42	130.88	0.11	1960.5	1984.5	25	25	25	−92	(24)	118	(25)	−33	(35)
Kanozan	35.25	139.96	0.34	1961.5	1984.5	24	24	24	−63	(24)	46	(25)	−41	(33)
Keles	41.42	69.20	0.45	1960.5	1963.5	4	4	4	−239	(30)	−42	(33)	10	(44)
Kiev	50.72	30.30	0.10	1960.5	1965.5	5	5	5	−39	(24)	172	(25)	303	(32)
Kiruna	67.83	20.42	0.39	1962.5	1966.5	5	5	5	−774	(25)	−1802	(25)	−218	(31)
Kiruna iii	67.83	20.42	0.00	1970.5	1983.5	14	14	14	−786	(22)	−1818	(22)	−191	(29)
Klyuchi	55.03	82.90	0.00	1967.5	1977.5	11	11	11	187	(26)	−87	(28)	−257	(34)
Klyuchi ii	55.03	82.90	0.00	1978.5	1984.5	7	7	7	174	(27)	−35	(28)	−182	(35)
Kodaikanal ii	10.23	77.46	2.32	1960.5	1984.5	25	25	25	−574	(28)	306	(35)	−62	(43)
Koror ii	7.33	134.50	0.01	1964.7	1966.2	3	3	3	117	(33)	−162	(36)	551	(45)
Krasnaya pakhra	55.48	37.31	0.20	1960.5	1984.5	25	25	25	198	(24)	89	(24)	307	(35)
Ksara	33.82	35.89	0.92	1960.5	1970.5	11	11	11	7	(22)	34	(26)	−158	(33)

Table 13: Observatory annual means listing (continued).

Station	Lat. (deg)	Lon. (deg)	Height (km)	Time Span Begin	Time Span End	Number X	Number Y	Number Z	CMP3 Bias (Error) X (nT)		Y (nT)		Z (nT)	
Kuyper iv	−6.03	106.73	0.00	1960.5	1962.5	3	3	3	149	(137)	588	(160)	−765	(196)
La paz ii	−16.54	291.90	0.43	1974.5	1976.5	3	3	3	18	(44)	178	(47)	132	(59)
La quiaca iv	−22.10	294.39	3.45	1961.5	1983.5	17	17	17	−19	(32)	−64	(38)	106	(46)
Lanzhou	36.09	103.85	1.56	1960.5	1984.5	25	25	25	100	(24)	−37	(26)	−85	(35)
Leirvogur	64.18	338.30	0.00	1960.5	1984.5	25	25	25	−318	(21)	604	(21)	−491	(30)
Lerwick ii	60.13	358.82	0.09	1960.5	1984.5	25	25	25	−99	(23)	187	(24)	23	(33)
Lhasa	29.70	91.15	3.66	1960.5	1974.5	15	15	15	131	(33)	−239	(36)	−164	(49)
Logrono	42.46	357.49	0.44	1960.5	1976.5	17	17	17	−25	(21)	1	(23)	37	(30)
Loparskoye	68.25	33.08	0.20	1961.5	1984.5	24	24	24	91	(22)	303	(22)	−439	(30)
Lovo	59.35	17.83	0.03	1960.5	1984.5	25	25	25	50	(21)	−28	(22)	36	(29)
Luanda bela ii	−8.92	13.17	0.05	1960.5	1980.3	21	21	21	258	(28)	−29	(27)	171	(40)
Luanda bela iii	−8.92	13.17	0.05	1981.5	1984.5	4	4	4	316	(34)	−125	(36)	331	(45)
Lunping	25.00	121.17	0.10	1965.7	1984.5	20	20	20	−62	(27)	258	(27)	173	(38)
Lvov ii	49.90	23.75	0.40	1960.5	1984.5	25	25	25	91	(21)	82	(21)	92	(28)
Lwiro	−2.25	28.80	1.68	1960.5	1970.5	10	10	10	290	(28)	−29	(31)	278	(40)
M bour	14.39	343.04	0.00	1960.5	1984.5	25	25	25	60	(26)	30	(29)	106	(39)
Macquarie i ii	−54.50	158.95	0.00	1960.5	1984.5	25	25	25	268	(35)	15	(37)	254	(43)
Magadan	60.12	151.02	0.00	1960.5	1966.5	6	6	6	−1326	(25)	418	(27)	1197	(34)
Majuro	7.08	171.38	0.00	1964.8	1966.1	3	3	3	−403	(39)	88	(43)	26	(58)
Manhay ii	50.30	5.68	0.44	1960.5	1973.5	13	13	13	8	(23)	9	(25)	234	(31)
Maputo	−25.92	32.58	0.05	1960.5	1963.5	4	4	4	337	(69)	202	(55)	−226	(78)
Maputo ii	−25.92	32.58	0.05	1964.5	1984.5	21	21	21	322	(28)	103	(30)	−122	(40)
Marion island	−46.87	37.85	0.00	1973.7	1980.5	8	8	8	−861	(28)	661	(30)	−1403	(41)
Martin vivies	−37.83	77.57	0.00	1981.6	1984.5	4	4	4	−534	(41)	−692	(38)	−2024	(54)
Mauritius v	−20.09	57.55	0.05	1963.5	1965.5	3	3	3	579	(40)	−340	(40)	−493	(50)
Mawson	−67.60	62.88	0.00	1960.5	1984.5	25	25	25	20	(33)	−3	(33)	100	(46)
Meanook iii	54.62	246.67	0.68	1960.5	1984.5	25	25	25	118	(24)	27	(26)	−101	(35)
Memambetsu ii	43.91	144.19	0.04	1960.5	1984.5	24	24	24	−197	(24)	137	(23)	−20	(33)
Mirnyy ii	−66.55	93.02	0.02	1960.5	1966.5	7	7	7	−117	(38)	10	(41)	−268	(54)
Mirnyy iii	−66.55	93.02	0.02	1967.5	1984.5	17	17	17	−124	(35)	−28	(40)	−327	(52)
Misallat	29.52	30.89	0.12	1960.6	1970.5	11	11	11	−75	(25)	4	(27)	134	(35)
Misallat ii	29.52	30.89	0.00	1971.5	1978.5	8	8	8	−78	(27)	55	(29)	270	(37)
Misallat iii	29.52	30.89	0.12	1979.5	1984.5	5	5	5	146	(28)	−389	(29)	242	(37)
Mizusawa	39.01	141.08	0.12	1969.5	1984.5	15	15	15	−182	(26)	84	(29)	−186	(36)
Moca	3.34	8.66	1.35	1960.5	1971.5	12	12	12	−155	(23)	−10	(30)	109	(35)
Molodezhnaya	−67.67	45.85	0.00	1965.5	1984.5	17	17	17	−34	(30)	−65	(31)	−146	(43)
Monte capellino	44.55	8.95	0.70	1960.5	1962.5	3	3	3	−45	(27)	−69	(29)	−595	(34)
Mould bay	76.20	240.60	0.15	1962.7	1984.5	23	23	23	−35	(23)	72	(22)	7	(32)
Muntinlupa	14.37	121.01	0.06	1960.5	1984.5	24	24	24	−157	(29)	517	(34)	301	(45)
Murmansk ii	68.95	33.05	0.21	1982.5	1984.5	3	3	3	376	(28)	319	(28)	−647	(35)
Nagycenk	47.63	16.72	0.16	1961.5	1980.5	20	20	20	0	(20)	−6	(21)	−21	(27)
Nagycenk ii	47.63	16.72	0.16	1981.5	1984.5	3	3	3	11	(27)	−5	(27)	−47	(32)
Nairobi	−1.33	36.81	1.67	1964.5	1980.5	16	16	16	59	(27)	−149	(29)	−228	(40)
Nampula	−15.09	39.25	0.38	1982.7	1984.5	3	3	3	−374	(40)	−738	(44)	162	(51)
Narssarssuaq	61.10	314.80	0.00	1968.9	1984.5	21	21	21	−409	(22)	284	(24)	531	(30)
New alesund	78.92	11.93	0.00	1966.5	1984.5	19	19	19	61	(22)	−5	(21)	−26	(30)
Newport	48.26	242.88	0.78	1966.6	1984.5	22	22	22	−67	(24)	89	(25)	−50	(35)
Niemegk ii	52.07	12.67	0.08	1960.5	1984.5	25	25	25	−47	(20)	4	(22)	0	(30)
Novo kazalinsk	45.80	62.10	0.00	1974.5	1984.5	11	11	11	−58	(27)	−157	(28)	34	(35)
Novolazarev ii	−70.77	11.83	0.46	1969.5	1982.5	14	14	14	−192	(31)	72	(31)	59	(45)
Novolazarevskay	−70.77	11.83	0.46	1961.5	1968.5	7	7	7	−192	(33)	67	(33)	227	(46)
Nurmijarvi	60.51	24.66	0.11	1960.5	1984.5	25	25	25	308	(20)	−36	(22)	148	(30)
Ottawa	45.40	284.45	0.76	1968.7	1984.5	17	17	17	123	(26)	−161	(27)	181	(37)
Pamatai ii	−17.57	210.43	0.09	1968.2	1972.5	5	5	5	−657	(32)	−1068	(33)	317	(45)
Pamatai iii	−17.57	210.43	0.09	1973.5	1984.5	12	12	12	−689	(31)	−672	(32)	−112	(44)
Panagyurishte	42.51	24.18	0.56	1960.5	1984.5	25	25	25	−224	(22)	−192	(23)	−202	(31)
Paramaribo	5.81	304.78	0.00	1960.5	1974.5	15	15	15	−54	(28)	91	(31)	−21	(41)
Paratunka	52.90	158.43	0.11	1969.5	1983.5	15	15	15	−404	(22)	188	(24)	181	(33)
Patrony ii	52.17	104.45	0.54	1960.5	1984.5	25	25	25	31	(25)	154	(26)	−77	(33)
Pilar ii	−31.67	296.12	0.34	1960.7	1984.5	25	25	25	−17	(34)	−73	(35)	13	(48)
Plateau	−79.25	40.50	3.62	1966.5	1968.5	3	3	3	−7	(36)	−28	(34)	−54	(50)
Pleshenitzi	54.50	27.88	0.20	1961.5	1984.5	24	24	24	236	(21)	147	(23)	−156	(29)
Podkam tung ii	61.60	90.00	0.00	1980.5	1984.5	5	5	5	1	(26)	−32	(27)	−194	(36)
Podkam tunguska	61.60	90.00	0.00	1969.5	1975.5	7	7	7	64	(25)	24	(26)	−309	(36)
Port moresby	−9.41	147.15	0.08	1960.5	1984.5	25	25	25	−16	(32)	60	(36)	404	(48)
Port-alfred	−46.43	51.87	0.00	1974.5	1980.5	7	7	7	−610	(33)	1230	(33)	130	(48)

Table 14: Observatory annual means listing (continued).

Station	Lat. (deg)	Lon. (deg)	Height (km)	Time Span Begin	Time Span End	Number X	Number Y	Number Z	CMP3 Bias (Error) X (nT)		Y (nT)		Z (nT)	
Port-alfred ii	−46.43	51.87	0.00	1981.5	1984.5	4	4	4	−727	(34)	1095	(35)	97	(49)
Port-aux-franca	−49.35	70.20	0.05	1960.5	1984.5	25	25	25	185	(35)	225	(36)	569	(51)
Pruhonice	49.99	14.55	0.33	1960.5	1972.5	13	13	13	−13	(21)	50	(22)	−39	(30)
Quetta	30.19	66.95	1.75	1960.5	1984.5	19	19	19	−27	(25)	13	(30)	4	(39)
Regensberg	47.48	8.44	0.60	1960.5	1969.5	10	10	10	32	(22)	41	(23)	−27	(28)
Resolute bay	74.70	265.10	0.03	1960.5	1984.5	25	25	25	−5	(22)	84	(22)	83	(32)
Roburent	44.30	7.89	0.81	1964.8	1968.5	5	5	5	55	(23)	−38	(26)	99	(31)
Roburent ii	44.30	7.89	0.81	1969.5	1973.5	5	5	5	62	(23)	48	(26)	56	(31)
Roi baudoui ii	−70.43	24.30	0.14	1964.7	1966.5	3	3	3	−64	(33)	−103	(34)	43	(45)
Rude skov	55.84	12.46	0.05	1960.5	1984.5	24	24	24	20	(21)	−15	(23)	−95	(30)
Sabhawala	30.36	77.80	0.50	1964.5	1973.5	10	10	10	−25	(29)	3	(29)	34	(40)
Sabhawala ii	30.36	77.80	0.50	1974.5	1984.5	11	11	11	−50	(29)	−38	(30)	38	(41)
San fernando	36.46	353.80	0.03	1960.5	1977.5	17	17	17	45	(23)	2	(26)	−71	(35)
San jose la ii	23.02	277.35	0.00	1971.5	1973.5	3	3	3	−2	(35)	23	(35)	−10	(46)
San juan	18.38	293.88	0.10	1960.5	1964.5	5	5	5	83	(36)	47	(41)	220	(51)
San juan ii	18.11	293.85	0.40	1965.5	1984.5	20	20	20	−84	(24)	222	(28)	256	(37)
San miguel iii	37.77	334.35	0.17	1960.5	1974.5	15	15	15	707	(22)	417	(25)	1731	(32)
San miguel iv	37.77	334.35	0.17	1975.5	1977.5	3	3	3	633	(34)	547	(37)	1661	(46)
San pablo	39.60	355.65	0.92	1981.5	1984.5	4	4	4	−30	(26)	17	(30)	−67	(35)
Sanae	−70.30	357.63	0.05	1962.7	1970.5	9	9	9	45	(31)	3	(32)	−4	(43)
Sanae ii	−70.32	357.63	0.05	1971.7	1978.5	8	8	8	12	(33)	−6	(33)	−33	(44)
Sanae iii	−70.31	357.59	0.05	1980.5	1984.5	5	5	5	28	(33)	6	(34)	7	(44)
Scott base ii	−77.85	166.78	0.01	1964.5	1984.5	21	21	21	−2252	(33)	−823	(33)	−3848	(47)
Sheshan	31.10	121.19	0.10	1960.5	1984.5	25	25	25	−239	(23)	226	(27)	270	(36)
Shillong	25.57	91.88	0.00	1976.5	1984.5	9	9	9	−75	(35)	−159	(37)	−478	(46)
Simosato	33.58	135.94	0.06	1960.5	1977.5	18	18	18	−135	(26)	20	(25)	−24	(36)
Sitka iii	57.06	224.68	0.02	1960.5	1984.5	25	25	25	−29	(24)	20	(24)	−20	(33)
Sodankyla ii	67.37	26.63	0.18	1960.5	1984.5	25	25	25	−144	(21)	−12	(21)	−648	(29)
South georg ii	−54.28	323.52	0.00	1975.5	1982.5	8	8	8	−85	(33)	−313	(36)	114	(49)
South pole	−89.99	346.68	2.80	1960.5	1971.5	12	12	12	−1340	(70)	−3332	(72)	23	(148)
Srednikan v	62.44	152.31	0.61	1961.5	1966.5	5	5	5	112	(25)	24	(27)	170	(33)
St john s	47.59	307.32	0.00	1968.8	1984.5	17	17	17	120	(28)	51	(27)	9	(38)
Stekoliniy	60.12	151.02	0.00	1966.5	1979.5	14	14	14	−270	(22)	−679	(23)	16	(30)
Stekoliniy ii	60.12	151.02	0.00	1980.5	1984.5	5	5	5	−264	(25)	−707	(26)	30	(32)
Stepanovka iii	46.78	30.88	0.14	1960.5	1984.5	25	25	25	−117	(20)	−686	(22)	87	(30)
Stonyhurst iii	53.85	357.53	0.12	1961.5	1967.5	7	7	7	28	(24)	70	(26)	19	(31)
Surlari ii	44.68	26.25	0.08	1961.5	1984.5	23	23	23	15	(23)	−26	(24)	−57	(32)
Swider	52.12	21.25	0.10	1960.5	1969.5	10	10	10	−348	(21)	−172	(23)	222	(29)
Syowa base	−69.01	39.59	0.00	1960.6	1962.5	3	3	3	−27	(53)	7	(48)	26	(61)
Syowa base ii	−69.01	39.59	0.00	1966.5	1984.5	18	18	18	31	(32)	−23	(29)	46	(48)
Tahiti ii	−17.56	210.39	0.09	1966.5	1972.5	6	6	6	−658	(32)	−1068	(33)	306	(45)
Tamanrasset ii	22.79	5.53	1.38	1960.5	1964.5	5	5	5	156	(30)	−200	(36)	−123	(44)
Tamanrasset iii	22.79	5.53	1.38	1965.5	1979.5	15	15	15	108	(23)	−184	(26)	−93	(34)
Tamanrasset iv	22.79	5.53	1.38	1980.5	1984.5	5	5	5	142	(28)	−177	(31)	−65	(38)
Tananarive iii	−18.92	47.55	1.38	1960.5	1976.5	17	17	17	400	(28)	17	(29)	−368	(42)
Tangerang	−6.17	106.63	0.01	1964.5	1971.5	7	7	7	−506	(29)	144	(32)	−683	(39)
Tangerang ii	−6.17	106.63	0.01	1972.5	1978.5	7	7	7	−223	(37)	77	(41)	−103	(47)
Tangerang iii	−6.17	106.63	0.01	1979.5	1984.5	6	6	6	−104	(32)	57	(35)	137	(42)
Tatuoca ii	−1.20	311.49	0.01	1960.5	1976.5	17	17	17	−13	(31)	−34	(34)	210	(44)
Tatuoca iii	−1.20	311.49	0.01	1979.5	1984.5	6	6	6	49	(35)	−231	(38)	149	(47)
Tehran	35.74	51.38	1.37	1960.5	1971.5	11	11	11	−58	(24)	65	(25)	−204	(34)
Teoloyucan vi	19.75	260.82	2.28	1960.5	1980.5	19	19	19	−71	(28)	36	(31)	−37	(41)
Thule iii	77.48	290.83	0.06	1960.5	1982.0	24	24	24	−40	(22)	33	(21)	−74	(29)
Thule iv	77.48	290.83	0.06	1982.5	1984.5	3	3	3	−199	(29)	−3	(28)	−76	(34)
Tihany	46.90	17.89	0.19	1960.5	1977.5	18	18	18	10	(20)	−3	(22)	−10	(29)
Tihany ii	46.90	17.89	0.19	1978.5	1984.5	5	5	5	−5	(23)	19	(26)	−12	(31)
Tiksi iv	71.58	129.00	0.04	1960.5	1962.5	3	3	3	−45	(33)	−156	(36)	−120	(48)
Tiksi v	71.58	129.00	0.04	1963.5	1967.5	5	5	5	−63	(25)	−135	(26)	−76	(33)
Tiksi vi	71.58	129.00	0.04	1969.5	1981.5	13	13	13	−76	(22)	−155	(23)	−50	(31)
Toledo iii	39.88	355.95	0.50	1961.5	1981.5	21	21	21	−9	(22)	−3	(25)	−12	(32)
Tomsk	56.47	84.93	0.20	1960.5	1969.5	10	10	10	35	(28)	87	(26)	−355	(37)
Toolangi iii	−37.53	145.47	0.46	1960.5	1979.2	20	20	20	−52	(31)	6	(32)	66	(44)
Trelew	−43.25	294.68	0.03	1960.5	1970.5	11	11	11	147	(33)	86	(39)	−47	(49)
Trelew ii	−43.25	294.68	0.03	1972.5	1984.5	13	13	13	38	(33)	246	(40)	−54	(50)
Trivandrum	8.48	76.95	0.30	1960.5	1984.5	24	24	24	190	(27)	223	(36)	141	(40)
Tromso	69.66	18.95	0.11	1960.5	1984.5	25	25	25	156	(21)	−429	(21)	165	(28)

Table 15: Observatory annual means listing (continued).

Station	Lat. (deg)	Lon. (deg)	Height (km)	Time Span Begin	Time Span End	Number X	Number Y	Number Z	CMP3 Bias (Error) X (nT)		CMP3 Bias (Error) Y (nT)		CMP3 Bias (Error) Z (nT)	
Tsumeb	−19.22	17.70	0.08	1964.8	1984.5	21	21	21	12	(31)	−56	(33)	96	(42)
Tucson	32.25	249.17	0.77	1960.5	1984.5	25	25	25	−119	(23)	−106	(30)	84	(33)
Tulsa	35.91	264.21	0.33	1968.9	1984.2	3	3	3	−97	(36)	20	(37)	32	(48)
Tuntungan	3.51	98.56	0.00	1982.5	1984.5	3	3	3	−44	(43)	−30	(43)	−457	(59)
Ujjain	23.18	75.78	0.00	1979.5	1984.5	6	6	6	−289	(29)	180	(31)	345	(43)
Ulan bator	47.85	107.05	0.00	1966.5	1977.5	12	12	12	−22	(27)	25	(25)	25	(37)
Urumqi	43.82	87.70	0.97	1980.5	1984.5	5	5	5	−2	(31)	−55	(32)	−111	(41)
Valentia iii	51.93	349.75	0.01	1960.5	1984.5	25	25	25	117	(22)	−60	(23)	27	(30)
Vannovskaya	37.95	58.11	0.57	1960.5	1962.5	3	3	3	170	(32)	125	(31)	39	(41)
Vannovskaya ii	37.95	58.11	0.57	1963.5	1984.5	21	21	21	165	(24)	105	(23)	58	(33)
Vassouras	−22.40	316.35	0.46	1960.5	1984.5	25	25	25	78	(33)	−23	(34)	158	(50)
Victoria	48.52	236.58	0.20	1960.5	1984.5	25	25	25	−15	(27)	−33	(26)	−378	(39)
Vostok	−78.45	106.87	3.50	1960.5	1984.5	22	22	22	−21	(38)	23	(33)	162	(51)
Voyeykovo	59.95	30.70	0.07	1960.5	1984.5	25	25	25	6	(21)	−55	(22)	−151	(32)
Vysokay dub iii	56.73	61.07	0.29	1960.5	1966.5	7	7	7	−301	(26)	−113	(26)	−495	(35)
Vysokay dub iv	56.73	61.07	0.29	1967.5	1976.5	10	10	10	−289	(24)	−111	(25)	−472	(33)
Vysokay dub v	56.73	61.07	0.29	1979.5	1980.5	2	2	2	305	(32)	−288	(32)	−146	(38)
Whiteshell	49.75	264.75	0.00	1977.5	1980.4	4	4	4	172	(30)	−251	(34)	−220	(41)
Wien kobenzl	48.26	16.32	0.40	1960.5	1984.5	25	25	25	28	(20)	9	(20)	48	(27)
Wilkes	−66.25	110.58	0.01	1960.5	1966.5	7	7	7	664	(46)	−405	(45)	124	(62)
Wingst	53.74	9.07	0.05	1960.5	1984.5	25	25	25	−15	(23)	50	(22)	−18	(30)
Witteveen	52.81	6.67	0.02	1960.5	1984.5	25	25	25	−18	(22)	35	(22)	−32	(32)
Wuhan	30.53	114.56	0.04	1960.5	1984.5	25	25	25	154	(26)	223	(28)	−198	(38)
Yakutsk ii	62.02	129.72	0.10	1960.5	1964.5	5	5	5	21	(27)	−1136	(29)	81	(37)
Yakutsk iii	62.02	129.72	0.10	1965.5	1984.5	20	20	20	46	(20)	−1153	(22)	110	(29)
Yangi-bazar ii	41.33	69.62	0.81	1964.5	1984.5	19	19	19	−311	(24)	38	(25)	−105	(35)
Yellow-knife	62.40	245.50	0.18	1975.5	1984.5	10	10	10	374	(25)	−231	(25)	158	(36)
Yuzhno sakh ii	46.95	142.72	0.07	1960.5	1969.5	10	10	10	−10	(25)	−77	(27)	−163	(33)
Yuzhno sakh iii	46.95	142.72	0.07	1970.5	1977.5	8	8	8	−143	(26)	12	(27)	116	(34)
Yuzhno sakh iv	46.95	142.72	0.07	1978.5	1984.5	7	7	7	−130	(26)	2	(28)	110	(34)
Zaymishche ii	55.83	48.85	0.08	1960.5	1972.5	13	13	13	−244	(22)	−267	(25)	−321	(30)
Zaymishche iii	55.83	48.85	0.08	1978.5	1984.5	7	7	7	−87	(24)	−77	(26)	46	(31)

REPORT DOCUMENTATION PAGE

Form Approved
OMB No. 0704-0188

1. AGENCY USE ONLY *(Leave blank)*	2. REPORT DATE	3. REPORT TYPE AND DATES COVERED
	April 2000	Technical Memorandum

4. TITLE AND SUBTITLE

A Comprehensive Model of the Near-Earth Magnetic Field: Phase 3

5. FUNDING NUMBERS

Code 921

6. AUTHOR(S)

Terence J. Sabaka, Nils Olsen, and Robert A. Langel

7. PERFORMING ORGANIZATION NAME(S) AND ADDRESS (ES)

Geodynamics Branch
Goddard Space Flight Center
Greenbelt, Maryland 20771

8. PEFORMING ORGANIZATION REPORT NUMBER

2000–02234-0

9. SPONSORING / MONITORING AGENCY NAME(S) AND ADDRESS (ES)

National Aeronautics and Space Administration
Washington, DC 20546-0001

10. SPONSORING / MONITORING AGENCY REPORT NUMBER

TM-2000–209894

11. SUPPLEMENTARY NOTES

Sabaka: Raytheon ITSS, Lanham, Maryland, 20706, email: sabaka@geomag.gsfc.nasa.gov; Olsen: Danish Space Research Institute, Juliane Maries Vej 30, DK-2100 Copenhagen Ø, Denmark; Langel: Formerly, NASA-GSFC, Geodynamics Branch, Greenbelt, Maryland 20771

12a. DISTRIBUTION / AVAILABILITY STATEMENT

Unclassified–Unlimited
Subject Category:
Report available from the NASA Center for AeroSpace Information,
7121 Standard Drive, Hanover, MD 21076-1320. (301) 621-0390.

12b. DISTRIBUTION CODE

13. ABSTRACT *(Maximum 200 words)*

The near-Earth magnetic field is due to sources in Earth's core, ionosphere, magnetosphere, lithosphere, and from coupling currents between ionosphere and magnetosphere and between hemispheres. Traditionally, the main field (low degree internal field) and magnetospheric field have been modeled simultaneously, and fields from other sources modeled separately. Such a scheme, however, can introduce spurious features. A new model, designated CMP3 (Comprehensive Model: Phase 3), has been derived from quiet-time Magsat and POGO satellite measurements and observatory hourly and annual means measurements as part of an effort to coestimate fields from all of these sources. This model represents a significant advancement in the treatment of the aforementioned field sources over previous attempts, and includes an accounting for main field influences on the magnetosphere, main field and solar activity influences on the ionosphere, seasonal influences on the coupling currents, *a priori* characterization of ionospheric and magnetospheric influence on Earth-induced fields, and an explicit parameterization and estimation of the lithospheric field. The result of this effort is a model whose fits to the data are generally superior to previous models and whose parameter states for the various constituent sources are very reasonable.

14. SUBJECT TERMS	15. NUMBER OF PAGES
Comprehensive model phase 3; near-Earth magnetic field; core; lithosphere; ionosphere; magnetosphere; coupling currents; induction.	75
	16. PRICE CODE

17. SECURITY CLASSIFICATION OF REPORT	18. SECURITY CLASSIFICATION OF THIS PAGE	19. SECURITY CLASSIFICATION OF ABSTRACT	20. LIMITATION OF ABSTRACT
Unclassified	Unclassified	Unclassified	UL